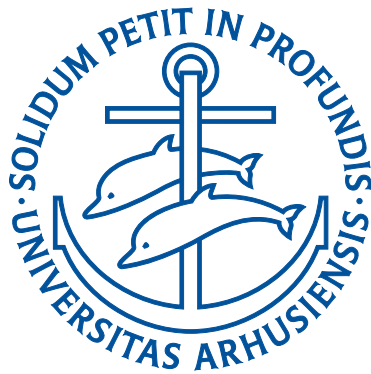


**ULTRASHORT LASER-PULSE  
MODIFICATION OF MATERIALS:  
QUANTIFYING METAL-NANOPARTICLE  
NEAR FIELDS AND TRANSIENT OPTICAL  
PROPERTIES OF DIELECTRICS**



**Søren Hanghøj Møller**

Department of Physics and Astronomy  
Aarhus University, Denmark

PhD thesis  
July 2019

This thesis has been submitted to the Graduate School of Science and Technology (GSST) at Aarhus University, in order to fulfil the requirements for obtaining a Ph.D. degree in physics. The work has been carried out under the supervision of Professor Peter Balling at the Department of Physics and Astronomy.

This document was compiled and typeset in L<sup>A</sup>T<sub>E</sub>X

July, 2019

## ABSTRACT

A major part of this thesis is related to the SunTune project, which deals with ways of improving solar cells by combining photon upconversion and metal nanoparticles (plasmonics). The attractive feature of metal nanoparticles is their ability to strongly concentrate light in their immediate vicinity (near-field zone). We have developed an experimental approach that utilizes ultrashort laser pulses to permanently mark near fields of metal nanoparticles, either into an underlying substrate by laser ablation, or by polymerization of a photoresist enclosing the particles. The existence of well-defined threshold fluences for ablation and polymerization enables experimental quantification of near-field enhancement factors. Detailed maps of experimental near fields of various metal nanoparticles have been obtained and compared quantitatively to electric-field simulations.

A second part of the thesis is concerned with fundamental studies related to laser-matter interactions. In one project, we investigated ablation and amorphization thresholds of  $\text{Ge}_2\text{Sb}_2\text{Te}_5$  (GST) thin films. The observed dependence of the threshold values on film thickness gave important clues toward the physical mechanisms underlying ablation and amorphization. For instance, we found that amorphization of GST is thermally driven, whereas ablation in a low-fluence regime is caused by the build-up, and subsequent relaxation, of large pressure waves, which ultimately tears the material apart.

Transient optical properties of dielectrics, excited by ultrashort laser pulses above the ablation threshold, were investigated by time-resolved *s*- and *p*-reflectivity measurements. About 100 fs after excitation, we discovered that the “standard” approaches to modeling the reflectivities, based e.g. on the Fresnel equations, completely failed to describe our data. We managed to model the data by proposing that a thin electron cloud is produced in front of the laser-excited target by electron emission.

Time-resolved cathodoluminescence (CL) measurements of  $\text{Er}^{3+}$  ions were

carried out during a research stay in Albert Polman's group at AMOLF in The Netherlands, in order to study how metal nanoparticles influence the decay rates of excited  $\text{Er}^{3+}$  ions. In CL, a focused electron beam is used to selectively excite certain ions with high spatial resolution. We observed that the decay rate of ions very close to a nanoparticle increased by 4–6 times.

## DANSK RESUMÉ

En betydelig del af denne afhandling er relateret til SunTune-projektet, hvor målet er at forbedre solceller ved at kombinere foton-opkonvertering og metalnanopartikler (plasmonics). Den eftertragtede egenskab ved metalnanopartikler er deres evne til at koncentrere lys kraftigt i deres nære omgivelser (nærfelts-zone). Vi har, ved brug af ultrakorte laser-pulser, udviklet en eksperimentel tilgang til markering af nærfelter fra metalnanopartikler enten i et underliggende substrat ved laser ablation eller ved polymerisation af en fotoresist, der omslutter partiklerne. Eksperimentel kvantificering af graden af nærfeltsforstærkninger muliggøres grundet forekomsten af bestemte tærskelfluenser for ablation og polymerisation. Detaljerede kort over eksperimentelle nærfelter fra forskellige nanopartikler blev opmålt og sammenlignet kvantitativt med simuleringer af elektriske felter.

En anden del af afhandlingen omhandler grundlæggende studier af laser-materiale vekselvirkninger. Vi har, i et af disse projekter, undersøgt ablations- og amorfiserings-tærskler af  $\text{Ge}_2\text{Sb}_2\text{Te}_5$  (GST) tyndfilm. De observerede afhængigheder af tærskelværdierne med filmtykkelse gjorde det muligt at udpege de fysiske processer, der forårsager ablation og amorfisering. Vi opdagede eksempelvis, at amorfiseringen i GST drives af termisk effekter, og at ablation i regimer ved lav fluens skyldes opbyggelsen af et enormt tryk, som efterfølgende afgives i form af kraftige trykbølger, der til sidst flår materialet fra hinanden.

Transiente optiske egenskaber af dielektrika, exciteret over ablations-tærsklen med ultrakorte laser pulser, blev undersøgt med tids- og polarisationsopløste målinger af *s*- og *p*-refleksioner. Vi opdagede, omtrent 100 fs efter excitation, at de "gængse" tilgange til modellering af refleksionerne, eksempelvis med Fresnels ligninger, brød sammen. Det lykkedes os at modellere målingerne ved at foreslå at en tynd elektronsky opbygges foran det laser-exciterede dielektrikum ved elektronemission.

Tidsopløste målinger af katodeluminescens (CL) fra  $\text{Er}^{3+}$  blev udført ved et forskningsophold i Albert Polmans gruppe ved AMOLF i Holland; formålet var at studere hvordan metalnanopartikler påvirker henfaldsraterne af exciterede  $\text{Er}^{3+}$  ioner. I CL bruges en fokuseret elektronstråle til selektivt at excitere bestemte  $\text{Er}^{3+}$  ioner med høj rumlig præcision. Vi observerede at henfaldsraten af ioner meget tæt på en metalnanopartikel øgedes med en faktor 4-6.

## ACKNOWLEDGEMENTS

It is now exactly four years ago since I started working on this PhD project in materials science and ultrafast laser physics. Every step along the way has been awesome, which is largely due to all the amazing people that I have been lucky to work with.

My deepest thanks go to my supervisor and mentor Peter Balling: Working with you these past four years have been the best! Peter's guidance and excellent insight on physics and on seemingly all technical issues have greatly propelled this work. Every (rough) version of a draft for a manuscript has been scrutinized vigorously and rigorously by Peter, vastly improving the content, and, not least phrasings and grammar. Peter has been supportive all the way and a big inspiration.

I would like to express my thanks to all past and present members of the semiconductor group and the SunTune project for contributing to a productive and fun working environment. Special thanks to Emil Haldrup Eriksen and Joakim Vester-Petersen for all the numerical calculations (and explaining how they work); to Harish Lakhotiya, Adnan Nazir, and Søren Roesgaard for providing top-quality samples; and finally, to Jeppe Christiansen for sharing a passion about optics. I am grateful for discussions with Søren P. Madsen and Brian Julsgaard.

Thanks also to Innovation Fund Denmark for funding the SunTune project, and, accordingly, my PhD.

I appreciate all the help provided by Bjarke Rolighed Jeppesen, Jacques Chevallier, John Lundsgaard Hansen, and Pia Bomholt Jensen on virtually all practical materials-science related issues addressed in this thesis, not least for training me on various equipment, and for all kinds of handy tips and tricks.

I can hardly thank Jan Thøgersen enough for help on various issues related to our new (now 4 years old) femtosecond laser system, and for *invaluable* guidance on how to align an OPA from scratch.

It has been a joy working closely together with a lot of master's and bachelor' students in the group: Peter Tønning, Gunhild Thorsen, Sebastian T. Andersen, Rune Bloom, and Christian Vandborg. A big shout-out to Henrik Dueholm and Gunhild for completely rewriting the old Labview (spaghetti) code for motion control to something that is much more manageable.

The months spent in Albert Polman's group at AMOLF, Amsterdam, were wonderful. The atmosphere was extremely stimulating, and I enjoyed the many group meetings and coffee breaks. Thanks to Magda, Sophie, and Nick for training and assistance on cathodoluminescence. I am particularly grateful to Nick for taking such good care of me in Amsterdam. To everyone in the group – Albert, Andrea, Joris, Magda, Nick, Sophie, Tom, Verena: Thank you...! My visit was so much fun because of you.

I have very much enjoyed sharing office with Emil, Jeppe, and Nicolai Søgaard – you guys rock! I also appreciate the awesome “lunch club” for... well, the lunch breaks, coffee drinking, cake eating, etc...

I am grateful to Jeppe, Jesper, Niels Jakob, and Thomas for proofreading parts of this thesis.

Finally, I would like to express my sincerest thanks to my friends and family – especially my parents and my brother – for all their amazing support.

Aarhus, July 2019  
Søren Hanghøj Møller

# LIST OF PUBLICATIONS

## Publications included in this thesis

- **S. H. Møller**, J. Vester-Petersen, A. Nazir, E. H. Eriksen, B. Julsgaard, S. P. Madsen, and P. Balling: *Near-field marking of gold nanostars by ultrashort pulsed laser irradiation: experiment and simulations*, Appl. Phys. A **124**, 210 (2018). [1]
- **S. H. Møller**, E. H. Eriksen, P. L. Tønning, P. B. Jensen, J. Chevallier, and P. Balling: *Femtosecond-laser-induced modifications of Ge<sub>2</sub>Sb<sub>2</sub>Te<sub>5</sub> thin films: Permanent optical change without amorphization*, Appl. Surf. Sci. **476**, 221 (2019). [2]
- **S. H. Møller**, S. T. Andersen, and P. Balling: *Transient optical properties of highly excited dielectric materials at variance with reflection from an air–solid interface: Signatures of ultrafast electron emission*. Submitted to Phys. Rev. Lett. (2019).

## Other publications

- P. Balling, J. Christiansen, R. E. Christiansen, E. H. Eriksen, H. Lakhotiya, M. Mirsafaei, **S. H. Møller**, A. Nazir, J. Vester-Petersen, B. R. Jeppesen, P. B. Jensen, J. L. Hansen, S. K. Ram, O. Sigmund, M. Madsen, S. P. Madsen, and B. Julsgaard: *Improving the efficiency of solar cells by upconverting sunlight using field enhancement from optimized nano structures*, Opt. Mater. **83** 279–289 (2018).
- S. P. Madsen, J. Christiansen, R. E. Christiansen, J. Vester-Petersen, **S. H. Møller**, H. Lakhotiya, A. Nazir, E. H. Eriksen, S. Roesgaard, O. Sigmund, J. S. Lissau, M. Madsen, B. Julsgaard, and P. Balling: *Improving*

*the efficiency of upconversion by light concentration using nano-particle design*, submitted to J. Phys. D (2019).

- J. Christiansen, J. Vester-Petersen, S. Roesgaard, **S. H. Møller**, R. E. Christiansen, O. Sigmund, S. P. Madsen, P. Balling, and B. Julsgaard: *Strongly enhanced upconversion by topology-optimized gold nanostructures*, submitted to Light Sci. Appl.

### **Planned publications**

- **S. H. Møller**, S. R. Nielsen, J. G. R. Thorsen, S. P. Madsen, B. Julsgaard, and P. Balling: *Visualizing and quantifying resonant electric near fields in topology-optimize plasmonic nanostructures by femtosecond-laser-induced multiphoton polymerization*.

# CONTENTS

<b>Abstract</b>	<b>iii</b>
<b>Dansk resumé</b>	<b>v</b>
<b>Acknowledgements</b>	<b>vii</b>
<b>List of publications</b>	<b>ix</b>
<b>1 Introduction</b>	<b>1</b>
1.1 SunTune . . . . .	2
1.2 Plasmonically enhanced upconversion . . . . .	5
1.3 Plasmonic near-field measurements . . . . .	6
1.4 Other projects . . . . .	7
1.5 Outline . . . . .	8
<b>2 Optics</b>	<b>9</b>
2.1 Maxwell's equations . . . . .	9
2.2 The dielectric function . . . . .	10
2.3 Fresnel's equations . . . . .	12
<b>3 Plasmonics</b>	<b>17</b>
3.1 Optical properties of metals . . . . .	17
3.2 Localized surface plasmons . . . . .	19
3.3 Absorption, scattering and extinction . . . . .	22
3.4 Far-field and near-field resonances . . . . .	24
<b>4 Ultrashort laser pulses</b>	<b>25</b>
4.1 Basic concepts . . . . .	26
4.2 Excitation of materials . . . . .	27

4.3	Material relaxation: damage and ablation . . . . .	30
<b>5</b>	<b>Near-field marking on TiO<sub>2</sub></b>	<b>33</b>
5.1	Background . . . . .	33
5.2	Contribution . . . . .	34
5.A	Introduction . . . . .	35
5.B	Methods . . . . .	37
5.C	Results and discussion . . . . .	42
5.D	Conclusion . . . . .	47
5.3	Comments . . . . .	48
<b>6</b>	<b>Near-field marking in SU-8</b>	<b>49</b>
6.1	Introduction . . . . .	50
6.2	Multiphoton polymerization . . . . .	51
6.3	Experimental approach . . . . .	53
6.4	Results and discussion . . . . .	55
6.5	Conclusion and outlook . . . . .	62
<b>7</b>	<b>Laser modifications of Ge<sub>2</sub>Sb<sub>2</sub>Te<sub>5</sub> thin films</b>	<b>65</b>
7.1	Background . . . . .	65
7.2	Contributions . . . . .	66
7.A	Introduction . . . . .	67
7.B	Experimental details . . . . .	68
7.C	Modelling . . . . .	70
7.D	Results . . . . .	72
7.E	Dicsussion . . . . .	78
7.F	Conclusion . . . . .	84
7.G	Appendix . . . . .	85
7.3	Near-field marking and Ge <sub>2</sub> Sb <sub>2</sub> Te <sub>5</sub> . . . . .	91
<b>8</b>	<b>Transient optical properties of excited dielectrics</b>	<b>93</b>
8.1	Contributions . . . . .	93
8.A	Supplemental material . . . . .	105
<b>9</b>	<b>Time-resolved cathodoluminescence of erbium</b>	<b>125</b>
9.1	Nanoparticle-emitter coupling . . . . .	126
9.2	Cathodoluminescence . . . . .	128
9.3	Pulsed CL . . . . .	130

9.4	Experimental investigations . . . . .	133
9.5	Discussion and conclusion . . . . .	139
10	<b>Conclusion and outlook</b>	<b>141</b>
	<b>Bibliography</b>	<b>145</b>



## INTRODUCTION

The temperature on Earth is rising at an alarming rate, and there is little doubt that the trend has been accelerated by humans. The Intergovernmental Panel on Climate Change (IPCC) put it very clearly in a report from 2013 [3]:

“Human influence has been detected in the major assessed components of the climate system. Taken together, the combined evidence increases the level of confidence in the attribution of observed climate change, and reduces the uncertainties associated with assessment based on a single climate variable. From this combined evidence it is *virtually certain* that human influence has warmed the global climate system.”

Greenhouse-gas emission<sup>1</sup> likely accounts for at least half of the human-induced global warming [3]. Unfortunately, inertia in the public and political belief system has slowed down actions to reduce greenhouse-gas emission, but the Paris Agreement in 2015 marks an important turning point; it obligates the United Nations to keep the increase in global mean surface temperature (GMST) below 2.0 °C, though preferably below 1.5 °C. Meanwhile, energy demand is

---

<sup>1</sup>The greenhouse effect was explained in 1856 by Eunice Newton Foot [4] – well before it had any noticeable impact on the climate!

constantly increasing, so implementation of sustainable, renewable and CO<sub>2</sub>-neutral energy sources into our society is key to uphold the Paris Agreement. Photovoltaics (PV) can easily accommodate the present and future energy demands,<sup>2</sup> and will no doubt be a big part of the solution to the climate-change problem.

Development of solar cells has evolved quickly, and production prices have gone down so much that installation costs now typically comprise 50% of the total price of solar-cell modules. This is limiting the cost benefit of PV, particularly for cheap but low-efficiency modules. It is therefore important for the PV industry that solar-cell efficiencies continue to increase. Much work still remains to be done before we reach the ultimate limits of solar-cell efficiencies [5].

## 1.1 SunTune

Single-junction solar cells are fundamentally limited by their band gap because they cannot absorb low-energy photons from the Sun. The vast majority of commercial solar cells are based on silicon, which, from a PV perspective, has a nearly ideal band gap of 1.1 eV (1100 nm) [6]. Yet silicon consequently fails to capture 20% of the solar energy contained in the sub-band-gap spectral range. This potential energy gain makes up the so-called band-gap loss. The SunTune project strives to reduce band-gap losses by constructing a device that allows utilization of low-energy photons in solar cells through photon upconversion (UC) and photon downshifting (DS). Harvesting these photons in silicon, while maintaining the band gap, can potentially the efficiency by several percentage points.

The SunTune concept is illustrated in Fig. 1.1, which also shows a graph of the solar spectral irradiance. Low-energy photons that are not absorbed by the active solar-cell material (silicon) are colored yellow and red. An upconverting material placed behind the solar cell can *upconvert* part of this lost light by the subsequent absorption of *two* low-energy red photons, later emitting a photon of higher energy (green) that can be absorbed by the active material. The upconverter chosen in SunTune has spectrally narrow absorption lines, so to exploit a greater part of the lost solar spectrum, a downshifter is placed behind the upconverter. The downshifter absorbs a broad range of photons (yellow)

---

<sup>2</sup>Assuming a rather high efficiency of 20%, less than 0.1% of the Earth's surface has to be covered by solar cells.

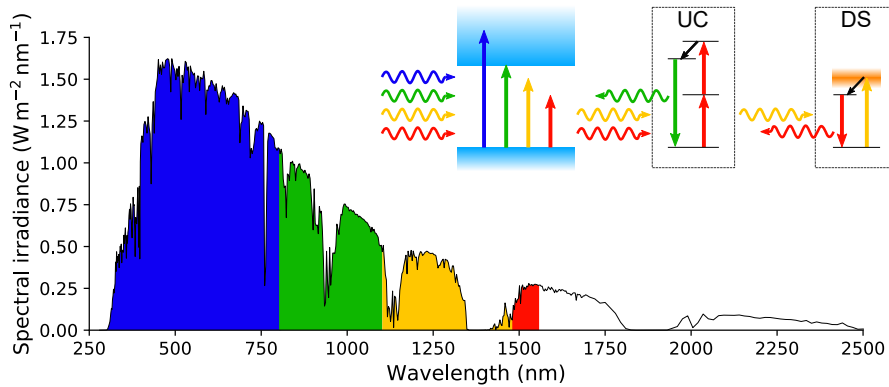


**Figure 1.1:** Graph of the spectral irradiance that Earth receives from the Sun, color-coded according to certain energy (wavelength) ranges. The sketch shows a solar-cell material (e.g. silicon) with a certain band gap that allows absorption of only the blue and green parts of the solar spectrum. The yellow and red parts, which constitute band-gap losses, can be converted to above-band-gap photons (green) via a combination of an upconverter (UC) and downshifter (DS) placed behind the active material: The UC absorbs two red photons and emits a green photon, while the DS converts the broad yellow spectral range into red photons that can be utilized by the UC for further upconversion to green photons.

and re-emits photons at lower energies (red) in a process called *downshifting*. The downshifted photons can be absorbed by the upconverter, thus making it possible, in principle, to convert the entire yellow and red spectral ranges in Fig. 1.1 to green, above-band-gap photons, utilizable by most semiconductor-based solar cells.

The main focus in SunTune has been on the UC process. UC is achieved by the use of the rare-earth element erbium (Er). When erbium is doped inside a dielectric host material, it typically appears as trivalent erbium ( $\text{Er}^{3+}$ ) with an electronic configuration  $[\text{Xe}]4f^{11}$ . The  $4f$  levels are split by strong spin-spin and spin-orbit coupling, which provides the energy states relevant for achieving UC of near-infrared light. The first few  $4f$  energy states of a free  $\text{Er}^{3+}$  ion are shown in Fig. 1.2. UC in SunTune is achieved through conversion of two  $\sim 1500$  nm photons to a single 980 nm photon as illustrated in the diagram.

But  $\text{Er}^{3+}$  has a serious flaw: transitions between the split  $4f$  levels are

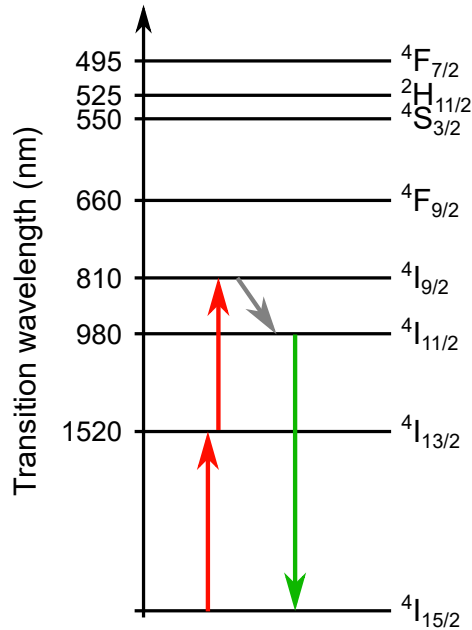


**Figure 1.2:** Energy levels of a free trivalent erbium ion ( $\text{Er}^{3+}$ ). UC of  $\sim 1500$  nm light is possible through the subsequent absorption of two such photons, giving rise to the process  ${}^4\text{I}_{15/2} \rightarrow {}^4\text{I}_{13/2} \rightarrow {}^4\text{I}_{9/2}$ . After a fast nonradiative relaxation to  ${}^4\text{I}_{11/2}$ , spontaneous emission produces 980 nm light that can be absorbed by many PV materials. Note that UC is not limited to absorption in the *same* ion; two nearby ions, both in the excited  ${}^4\text{I}_{13/2}$  state, can share energy via dipole-dipole interaction, thereby promoting one of the two ions to the  ${}^4\text{I}_{9/2}$  state from which spontaneous emission of 980 nm proceeds as usual.

electric-dipole forbidden because they share the same parity.<sup>3</sup> This is alleviated somewhat if  $\text{Er}^{3+}$  resides in a host material, where a reduction of the symmetry relaxes the selection rules of the  $4f$  transitions. In SunTune, the two typical host materials for  $\text{Er}^{3+}$  are  $\text{TiO}_2$  and  $\text{NaYF}_4$ ; both materials have low phonon energies, which significantly reduces the rate of unfavorable phonon-assisted relaxation of  $\text{Er}^{3+}$ . Electrostatic shielding by outer  $5s$  and  $5p$  electrons protects the  $4f$ -energy states against influence of the host, except for slight

<sup>3</sup>The parity of the  $4f$  shell is  $(-1)^l$  with  $l = 3$ . This remains true for the energy states split by spin-spin and spin-orbit interaction because both interactions commute with the parity operator, i.e. they preserve parity.

modifications of the energy levels by crystal-field splitting. Still, absorption in  $\text{Er}^{3+}$ , residing in either  $\text{TiO}_2$  or  $\text{NaYF}_4$ , remains low. This is a big issue for UC, which is fundamentally a nonlinear process where absorption of *at least* two photons is required for each upconverted photon.

## 1.2 Plasmonically enhanced upconversion

Because UC is a nonlinear process, the total UC yield (UCY) of  $\text{Er}^{3+}$  ions is enhanced by increasing the incident density of  $\sim 1500$  nm photons. This can readily be achieved by focusing the sunlight onto the UC device with a big lens. However, it is necessary that the lens tracks the position of the Sun in the sky, which makes this an impractical and expensive solution.

In SunTune, the approach is to utilize plasmonic (metallic) nanoparticles for focusing of the  $\sim 1500$  nm light near  $\text{Er}^{3+}$  ions. For these nanoparticles, concentration-factor enhancements in the near field (i.e. near the nanoparticle) may far exceed what is achievable by lenses, where the intensity of focused light is ultimately limited by diffraction. Because the optical response of plasmonic nanoparticles have great tunability in terms of their geometry (shape and size), they are good candidates for achieving not only excellent focusing of  $\sim 1500$  nm light, but also for obtaining a broad angular acceptance, such that an external tracking system of the Sun is not required.

To give an example of the utility of plasmonically enhanced upconversion, suppose that the average photon density at 1500 nm in a volume  $V_0$  containing  $\text{Er}^{3+}$  is  $\Phi_0$ . This situation is illustrated in Fig. 1.3(a). The average UCY is proportional to  $\Phi_0^2 V_0$ .<sup>4</sup> We now introduce a plasmonic nanoparticle, which concentrates the photon density in a small fraction  $f$  of the volume  $V = f V_0$ , such that the average photon density in this volume is  $\Phi = \Phi_0 (V_0/V) = f^{-1} \Phi_0$  and zero outside, as illustrated in Fig. 1.3(b). The resulting UCY is now proportional to  $\Phi^2 V = f^{-1} \Phi_0^2 V_0$ ; evidently, the UCY is enhanced by a factor of  $f^{-1}$ . Concentration enhancement by plasmonic nanoparticles easily reaches  $f^{-1} > 100$ , thus illustrating the usefulness plasmonically enhanced UC.

As the optical properties, including the concentration enhancement, of plasmonic nanoparticles is very dependent on the precise geometry, it is hard to predict what geometries are best suited for efficient UC. Consequently,

<sup>4</sup>The exponent is *two* because UC is a two-photon process, except under conditions of very high intensity where  $\text{Er}^{3+}$  ions are saturated, and the exponent approaches 1 [7]. Under normal sunlight conditions,  $\text{Er}^{3+}$  ions are far from saturated, and the exponent is 2.

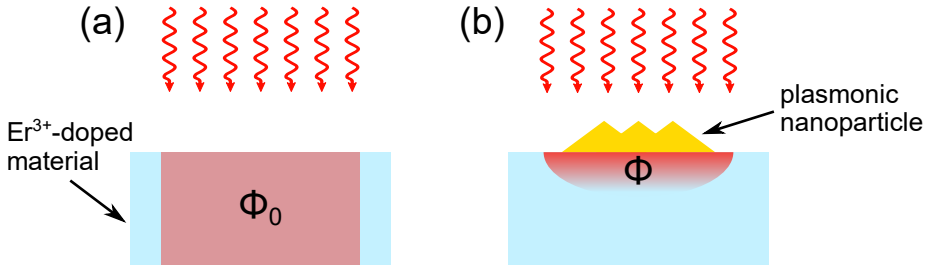


**Figure 1.3:** Illustration of plasmonic concentration of  $\sim 1500$  nm radiation (red arrows incident from above) inside an  $\text{Er}^{3+}$ -doped material. (a) Photon density  $\Phi_0$  (red-shaded region) inside the material under normal conditions. (b) The corresponding photon density  $\Phi$  when a plasmonic nanoparticle is placed on top of the material; the incident photons are concentrated in a small region near the nanoparticle.

in SunTune we utilize the geometrically unrestrained method of *topology optimization* (TopOpt) to search for optimal UC-enhancing nanoparticle geometries. In this procedure, Maxwell's equations for an incident plane-wave excitation of  $\sim 1500$  nm are solved in a gradient-based iterative procedure where gold (nanoparticle material) is gradually added and removed from a pre-determined design domain, eventually leading to a nanoparticle geometry with a high UCY.

### 1.3 Plasmonic near-field measurements

For TopOpt to be useful, it is obviously important that the calculations of the electric fields in the near-field zone of the nanoparticle, where UCY is primarily enhanced, agree with experimental values. Experimental confirmation of electric near-field calculations is challenging, because spatial variations of the near fields occur on length scales that are typically much smaller than optical wavelengths; the fields cannot, therefore, be probed directly by such light because of the diffraction limit.

Yet direct and quantitative measurements of electric near fields of nanostructures is possible by a clever application of short laser-pulse modification in materials surrounding the nanostructure [8]. My primary role in the SunTune project has been to carry out electric near-field measurements by femtosecond laser irradiation of metal nanoparticles used for improving the UCY of  $\text{Er}^{3+}$ . The experimental procedure builds upon earlier work (e.g. [8]),

and is described later in this thesis. We refer to the experimental technique as “near-field marking”. Confirmation of electric near-field calculations gives validation to the TopOpt procedure which is fundamental for achieving high plasmonically enhanced UC in SunTune.

Despite the technique is somewhat old (proposed in 2004), to my knowledge, it has not been used before to map out detailed quantitative near field patterns, as I present later in this thesis. Other techniques exist for imaging plasmonic near field, but they are typically unable to quantify the values of electric-field enhancements [9], which however our approach allows.

## 1.4 Other projects

We employed  $\text{Ge}_2\text{Sb}_2\text{Te}_5$  (GST) for the initial attempts toward near-field marking of metal nanoparticles. GST is a so-called phase-change material (PCM), which can be switched between a crystal and an amorphous structural state upon pulsed laser irradiation. The two phases have dramatically different properties. Because of this fact, amorphization of GST had been used previously for electric near-field imaging of dielectric microspheres [10, 11]. When we applied the same technique on gold nanoparticle, we saw no evidence of near-field effects on amorphization. This prompted further study, and lead to extensive work on laser-induced modifications in GST. A by-product is that we can now explain why GST was unsuited for near-field measurements of metal nanoparticles – and why it works for dielectric microspheres.

In a completely unrelated project to SunTune, we investigated the transient response of dielectrics – primarily fused silica – immediately after strong, ultra-short laser-pulse excitation through time- and polarization-resolved reflectivity measurements. The project was started as an opportune continuation of the work carried out by former PhD student Lasse Haahr-Lillevang. We observed a surprising ultrafast reflectivity response that could not be modeled by the “usual means” of applying Fresnel’s equation at an interface. A lot of effort was spent on explaining these result. We eventually found a simple model based on the formation of a thin electron cloud outside the dielectric, that could explain all the features in our measurements.

From Februar–May 2018, I visited Albert Polman’s group at AMOLF, The Netherlands, where I worked on time-resolved cathodoluminescence (CL) studies on  $\text{Er}^{3+}$ . My goal there was to measure, with nanometer spatial resolution, how the spontaneous emission rate of  $\text{Er}^{3+}$  ions is affected by

the presence of a nearby metal nanoparticle. The spontaneous emission rate usually increases dramatically when  $\text{Er}^{3+}$  is close to such metal particles. This poses a potential problem for SunTune, where the lifetime of the  $^4\text{I}_{15/2}$  state (see Fig. 1.2) should be as long as possible to promote UC, but at the same time, the ions must be close to the nanoparticle in order to benefit from light concentration in the near field. The experiments were challenging, mainly by a complicated time-dependent luminescence of  $\text{Er}^{3+}$ ; we did manage to see an enhancement of the spontaneous-emission rate of  $\text{Er}^{3+}$  near metal nanoparticles, but not with the spatial precision, originally envisioned.

## 1.5 Outline

Chapters 2–4 provide the background for the main topics of this thesis. The basics of optics with an emphasis on the dielectric function of the material response is described in Chapter 2. Chapter 3 gives an introduction to the field of plasmonics, which is at the heart of SunTune. Finally, Chapter 4 gives an overview of the concepts of ultrashort laser pulses and their interaction with materials.

Investigations of metal nanoparticles by near-field marking is presented Chapter 5 and 6. In Chapter 5, we used an approach based on ablation of the substrate beneath the nanoparticles. The investigations were published in [1], and is reproduced there. Chapter 6 details a different approach to near-field marking by multiphoton polymerization of a photoresist, which provides three dimensional maps of electric near-field distributions.

Work on projects, that are somewhat unrelated to SunTune, are presented in Chapters 7–9. Chapter 7 is related to studies of ablation and amorphization thresholds in GST thin films, which is published in [2], and reproduced in that chapter. Time- and polarization-resolved reflectivity studies on laser-excited dielectric is presented in Chapter 4, which is based on a recently submitted manuscript. My progress towards mapping out  $\text{Er}^{3+}$  lifetimes as a function of distance to metal nanoparticles with time-resolved CL is described briefly in Chapter 9.

A general conclusion and outlook concerning my PhD work is provided in Chapter 10.

## OPTICS

This chapter gives a brief account of the basic optical properties of materials that is relevant for this thesis.

### 2.1 Maxwell's equations

The relations between the electric field  $\mathbf{E}$ , the magnetic field  $\mathbf{B}$ , and electric charge densities  $\rho$  and current densities  $\mathbf{j}$  is contained in Maxwell's equations:

$$\nabla \cdot \mathbf{E} = \frac{1}{\varepsilon_0} \rho, \quad (2.1a)$$

$$\nabla \cdot \mathbf{B} = 0 \quad (2.1b)$$

$$\nabla \times \mathbf{E} = -\frac{\partial \mathbf{B}}{\partial t}, \quad (2.1c)$$

$$\nabla \times \mathbf{B} = \mu_0 \mathbf{j} + \mu_0 \varepsilon_0 \frac{\partial \mathbf{E}}{\partial t}, \quad (2.1d)$$

where,  $\varepsilon_0 = 8.85 \times 10^{-12} \text{ F m}^{-1}$  and  $\mu_0 = 4\pi \times 10^{-7} \text{ H m}^{-1}$  are the vacuum permittivity and vacuum permeability, respectively. The electromagnetic fields drive charges and current, which in turn affects the fields. An important

addition to Eq. (2.1) is the Lorentz force which, together with an equation of motion, tells precisely how a charge  $q$  with velocity  $\mathbf{v}$  responds to the electromagnetic field:

$$\mathbf{F} = q(\mathbf{E} + \mathbf{v} \times \mathbf{B}). \quad (2.2)$$

Light is electromagnetic waves (radiation) that was generated by some far-away source, the details of which we typically need not be concerned with. In vacuum ( $\rho = 0$ ,  $\mathbf{j} = \mathbf{0}$ ), monochromatic light with frequency  $\omega$  can be expressed in terms of plane propagating waves with a continuous spectrum of wave vectors  $\mathbf{k}$ . These wave vectors are related to the frequency  $\omega$  through the dispersion relation  $k = \omega/c$ , where  $c = 2.998 \times 10^8 \text{ m s}^{-1}$  is the speed of light (in vacuum). Specifically, the plane-wave component of the electric field propagating in the direction parallel  $\mathbf{k}$  is

$$\mathbf{E}(\mathbf{r}, t) = \mathbf{E}_{\mathbf{k},\omega} e^{i\mathbf{k}\cdot\mathbf{r} - i\omega t}. \quad (2.3)$$

The associated magnetic-field component may be obtained as  $\mathbf{B}_{\mathbf{k},\omega} = -(\mathbf{k} \times \mathbf{E}_{\mathbf{k},\omega})/\omega$ . The momentum of the plane wave is  $\hbar\mathbf{k}$ , and its photon energy is  $\hbar\omega$ .

Light that is not monochromatic (such as a short laser pulse) may be represented as a superposition of plane waves over a continuous range of frequencies and wave vectors. It is therefore, for most purposes, sufficient to only consider plane waves, as the generalization to more realistic situations dealing with non-monochromatic and diverging light is straightforward.

The energy flux  $\mathbf{S}$  of electromagnetic radiation is defined by Poynting's vector:

$$\mathbf{S} \equiv \frac{1}{\mu_0} \mathbf{E} \times \mathbf{B}. \quad (2.4)$$

This definition of energy flux is actually not unique; only changes in  $\mathbf{S}$  are observable, i.e.  $\nabla \cdot \mathbf{S}$ . In fact, any term with vanishing divergence could be added to Eq. (2.4) without changing the physics. It is easy to confirm that there is no energy loss in vacuum ( $\nabla \cdot \mathbf{S} = 0$ ).

## 2.2 The dielectric function

When dealing with the electromagnetic field inside materials, it is a hopeless task to consider the detailed microscopic fields that vary rapidly over the dimensions of an atom. Instead, we consider only macroscopic quantities

of the fields, charges, and currents, which have been suitably averaged over many atoms. We then find that the plane-wave description Eq. (2.3) of the fields hold in homogeneous materials, although Eq. (2.3) is modified slightly by the response of the material to external radiation. We are not concerned with magnetic or relativistic materials in the following, which means that the material response is entirely determined by the electric field.

The incident electromagnetic radiation induces charge currents in the material, and it is helpful to divide the material response into the two contributions: one due to *bound* charges (valence-band electrons) and the other due to *free* charges (conduction-band electrons). The free charges respond to  $\mathbf{E}$  according to Ohm's law:  $\mathbf{j}_f = \hat{\sigma}\mathbf{E}$ , where  $\hat{\sigma}$  is the conductivity of these electrons.<sup>1</sup> The bound charges respond according to the rate of change of the bound polarization density:  $\mathbf{j}_b = \partial\mathbf{P}_b/\partial t$  [12]. The induced polarization is defined by the electric susceptibility  $\hat{\chi}_b$ :

$$\mathbf{P}_b = \varepsilon_0 \hat{\chi}_b \mathbf{E}. \quad (2.5)$$

Let us make the simplification that the material is isotropic, which means that  $\mathbf{P}_b$  and  $\mathbf{j}_f$  are parallel to  $\mathbf{E}$ . In addition, we will assume that the response is local, i.e. the (macroscopic) fields at one location  $\mathbf{r}$  do not depend on the fields at nearby locations. This is usually a good approximation [13]. However, at optical frequencies we cannot in general ignore temporal dispersion, i.e. the fact that the material response is not instantaneous:  $\mathbf{P}_b$  and  $\mathbf{j}_f$  depends on  $\mathbf{E}$  both at present *and* earlier times. Eq. (2.5) may then be written

$$\mathbf{P}_b(\mathbf{r}, t) = \varepsilon_0 \int_{-\infty}^t dt' \chi_b(t - t') \mathbf{E}(\mathbf{r}, t'). \quad (2.6)$$

Similarly for Ohm's law. It is an advantage to express the fields in their frequency components  $\omega$  by applying the Fourier transform; Eq. (2.6) simplifies to

$$\mathbf{P}_{b,\omega}(\mathbf{r}) = \varepsilon_0 \chi_b(\omega) \mathbf{E}_\omega(\mathbf{r}). \quad (2.7)$$

Carrying this out for Ohm's law as well, the total current density inside the material for an excitation at frequency  $\omega$  becomes

$$\mathbf{j}_\omega = [\sigma(\omega) - i\omega\varepsilon_0\chi_b(\omega)]\mathbf{E}_\omega. \quad (2.8)$$

---

<sup>1</sup>Note the "hat" on  $\sigma$ ; in general,  $\hat{\sigma}$  is a linear operator, not just a number or a tensor.

Taking the curl of Ampere's law (2.1d) and inserting it into Faraday's law (2.1c), gives

$$\nabla \times (\nabla \times \mathbf{E}_\omega) = -i\mu_0\omega\mathbf{j}_\omega - \mu_0\varepsilon_0\omega^2\mathbf{E}_\omega, \quad (2.9)$$

or, using Eq. (2.8)

$$\nabla \times (\nabla \times \mathbf{E}_\omega) + \frac{\omega^2}{c^2}\varepsilon(\omega)\mathbf{E}_\omega = \mathbf{0}, \quad (2.10)$$

where we introduced the *dielectric function*

$$\varepsilon(\omega) = 1 + \chi_b(\omega) + \frac{i\sigma(\omega)}{\varepsilon_0\omega}. \quad (2.11)$$

The solution to Eq. (2.10) admits the plane-wave solutions of the kind in Eq. (2.3), but now the dispersion relation reads

$$\mathbf{k}^2 = \varepsilon(\omega)\frac{\omega^2}{c^2}. \quad (2.12)$$

The refractive index of the material  $n$  is defined as  $n = \sqrt{\varepsilon}$ , so the dispersion relation may also be expressed as  $k = n(\omega)\omega/c$ . We see that a finite imaginary part of  $n$  damps the plane-wave propagation inside the material. This occurs for instance in metals, where electric fields are efficiently screened out by free charges near the metal surface. The imaginary part of  $\varepsilon$  is associated with absorption of light by the material. This is readily seen from the spatial derivative of the time-averaged energy flux  $\langle \mathbf{S} \rangle$  in the direction of the energy flow (which we choose to be  $z$ ) [14, p. 23]:

$$\frac{\partial \langle S \rangle}{\partial z} = -\frac{1}{2} \operatorname{Re}\{\mathbf{j}^* \cdot \mathbf{E}\} = -\frac{1}{2}\sigma(\omega)\mathbf{E}_\omega^2. \quad (2.13)$$

In the second equality, we inserted Eq. (2.8) and assumed  $\chi_b(\omega)$  to be real.

### 2.3 Fresnel's equations

When light is incident onto a material boundary, it is partly reflected and partly transmitted. The Fresnel equations determine the reflected and transmitted amplitudes of an incident plane wave. The situation is sketched in Fig. 2.1(a) where light is incident in the  $xz$  plane ( $\mathbf{k}_1 = k_x\hat{\mathbf{x}} + k_z\hat{\mathbf{z}}$ ). We assume perfect symmetry in  $xy$ , which implies that  $k_x$  is conserved [13]. There is a difference

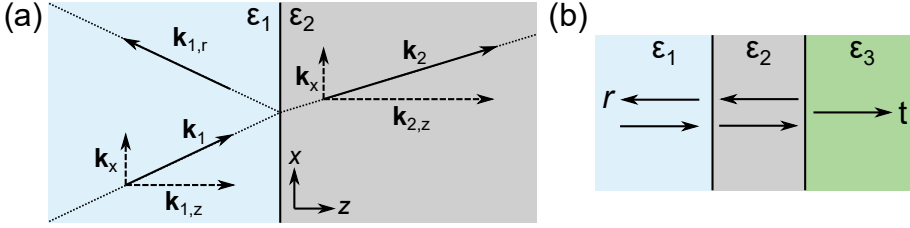


**Figure 2.1:** (a) Reflection and transmission at a single interface of an incident plane wave with wave vector  $\mathbf{k}_1$ . (b) Reflection ( $r$ ) and transmission ( $t$ ) of a plane wave in a multilayer material. The arrows indicate the  $z$  component of the wave vector of forward (right) and backwards (left) moving waves.

in reflection and transmission depending on whether the incident radiation is  $s$ -polarized ( $\mathbf{E}$  parallel to the interface) or  $p$ -polarized ( $\mathbf{B}$  parallel to the interface). The formulas are derived in most textbooks (e.g. [12–14]) by applying Maxwell's interface conditions at the boundary. The result is [14, p. 22]:

$$r_p = \frac{\epsilon_2 k_{z,1} - \epsilon_1 k_{z,2}}{\epsilon_2 k_{z,1} + \epsilon_1 k_{z,2}}, \quad (2.14a)$$

$$r_s = \frac{k_{z,1} - k_{z,2}}{k_{z,1} + k_{z,2}}, \quad (2.14b)$$

$$t_p = \frac{2\epsilon_2 k_{z,1}}{\epsilon_2 k_{z,1} + \epsilon_1 k_{z,2}} \sqrt{\frac{\epsilon_1}{\epsilon_2}}, \quad (2.14c)$$

$$t_s = \frac{2\epsilon_2 k_{z,1}}{\epsilon_2 k_{z,1} + \epsilon_1 k_{z,2}}. \quad (2.14d)$$

Here,  $r$  and  $t$  are the reflection and transmission amplitudes of the electric fields, respectively, and

$$k_{z,i} = \frac{\omega}{c} \sqrt{\epsilon_i - (ck_x/\omega)^2}, \quad (i = 1, 2) \quad (2.15)$$

according to the dispersion relation Eq. (2.12). Note that when light is incident into the material from vacuum (as it usually is somewhere),  $k_x = (\omega/c) \sin \theta$ , where  $\theta$  is the angle of incidence.

### 2.3.1 Multilayer systems

When dealing with a multilayered system as sketched in Fig. 2.1(b), it is necessary to consider multiple reflections from and transmissions at each interface. This quickly becomes cumbersome to keep track of, but there is an easier way. Consider for instance the interface between materials 1 and 2. In each of these regions there is a wave moving forward (to the right in Fig. 2.1)  $E_i^+$  and a wave moving backwards  $E_i^-$  ( $i = 1, 2$ ). Intuitively, we expect that

$$E_1^- = r_{12}E_1^+ + t_{21}E_2^-, \quad (2.16a)$$

$$E_2^+ = r_{21}E_2^- + t_{12}E_1^+, \quad (2.16b)$$

which can also be proved by applying Maxwell's boundary conditions [15]. Here, for example,  $r_{\alpha\beta}$  denotes the reflection coefficient of a plane wave incident from medium  $\alpha$  to medium  $\beta$ . (Following this convention, the Fresnel coefficients on the left-hand side of Eq. (2.14) should have the subscript "12".) We can put Eq. (2.16) in the following form:

$$\begin{pmatrix} E_1^- \\ E_1^+ \end{pmatrix} = M_1 \begin{pmatrix} E_2^- \\ E_2^+ \end{pmatrix} \quad (2.17)$$

At the next interface, the fields  $E_2$  are advanced by the phase  $k_{z,2}d_2$ , where  $d_2$  is the thickness of material 2:  $E_2^\pm \rightarrow E_2^\pm e^{\pm ik_{z,2}d_2}$ . The propagation can be represented by the action of a diagonal matrix:

$$P_2 = \begin{pmatrix} e^{-ik_{z,2}d_2} & 0 \\ 0 & e^{ik_{z,2}d_2} \end{pmatrix}. \quad (2.18)$$

Thus, at this interface between materials 2 and 3, we have

$$P_2 \begin{pmatrix} E_2^- \\ E_2^+ \end{pmatrix} = M_2 \begin{pmatrix} 0 \\ E_3^+ \end{pmatrix}, \quad (2.19)$$

which can be related to the fields in material 1 as

$$\begin{pmatrix} E_1^- \\ E_1^+ \end{pmatrix} = M_1 P_2^{-1} M_2 \begin{pmatrix} 0 \\ E_3^+ \end{pmatrix}. \quad (2.20)$$

To get the reflection and transmission coefficients of the full structure, simply put  $E_1^+ = 1$ ,  $E_1^- = r$ , and  $E_3^+ = t$ ; this leaves two linear equations with two

unknowns, which is easily solved. This procedure is known as the transfer-matrix method (TMM) [15]. Once  $t$  is known, it is straightforward to calculate the fields everywhere inside the multilayer structure. It is simple to generalize the procedure to an arbitrary multilayer system consisting of many layers.

The TMM was applied extensively in chapter 7 for estimating absorption in a variety of  $\text{Ge}_2\text{Sb}_2\text{Te}_5$  (GST) thin films.



## PLASMONICS

Plasmonics deals with optics of metal nanoparticles and metal interfaces. The field is quite old, as the fundamental physics was established in the early 1900s, but our understanding has matured a lot since then, thanks to computer modeling and improvements in fabrication and characterization of nanoscale structures [16]. This chapter gives an introduction to the basics of plasmonics.

### 3.1 Optical properties of metals

Metals have partially filled electronic bands which allows them to conduct electricity at any temperature. The response of the electrons in these bands to an applied electric field  $\mathbf{E}$  can be evaluated within the Drude model, where the electrons are treated as “free”, but damped by collisions at a rate  $\Gamma$  (scattering rate) [17]. The electrons obey the following equation of motion:

$$m\ddot{\mathbf{x}} = -m\Gamma\dot{\mathbf{x}} - e\mathbf{E}. \quad (3.1)$$

Here,  $\mathbf{x}$  is the displacement of the electrons from their initial position,<sup>1</sup>  $e = 1.602 \times 10^{-19}$  C is the elementary charge, and  $m = 9.11 \times 10^{-31}$  kg is

<sup>1</sup>The electrons of course have a thermal velocity, which however is zero when averaged over an ensemble of electrons. Thus, we have in mind not one particular electron, but rather an “average” electron from the ensemble.

the electron mass. For a periodic driving field of frequency  $\omega$ , the solution is

$$\mathbf{x} = \frac{e\mathbf{E}}{m(\omega^2 - i\omega\Gamma)}. \quad (3.2)$$

The induced current density of the electrons is  $\mathbf{j} = -n_e e \dot{\mathbf{x}}$ , where  $n_e$  is the density of free electrons. Equating this to Ohm's law, we obtain Drude's expression for the electrical conductivity of a metal:

$$\sigma(\omega) = \frac{in_e e^2 \omega}{m(\omega - i\Gamma)} \quad (3.3)$$

Comparing to Eq. (2.11), we see that the dielectric function of the metal can be expressed as

$$\varepsilon(\omega) = \varepsilon_b(\omega) - \frac{\omega_p^2}{\omega^2 + i\Gamma\omega}, \quad (3.4)$$

where  $\varepsilon_b(\omega)$  is the bound optical response due to electrons in the filled bands of the metal. In Eq. (3.4) we have introduced the *plasma frequency*  $\omega_p$  as

$$\omega_p \equiv \sqrt{\frac{e^2 n_e}{\varepsilon_0 m}}. \quad (3.5)$$

A good conductor has a low scattering rate and a large plasma frequency as compared to  $\omega$  at optical frequencies. Under the assumption that  $\Gamma \ll \omega$ ,

$$\varepsilon(\omega) \approx \varepsilon_b(\omega) - \frac{\omega_p^2}{\omega^2} \left(1 - i\frac{\Gamma}{\omega}\right) \quad (3.6)$$

The bound dielectric response is typically on the order of unity, so the real part of  $\varepsilon(\omega)$  is negative; this is the characteristic feature of  $\varepsilon$  for metals. Inspecting Eq. (2.15), we see that  $k_{z,i}$  attains a large imaginary part which leads to significant damping of light waves. This is not due to absorption (which we here assumed to be small), but rather due to reflection at the metal surface: The free electrons respond essentially instantly to the incident radiation, screening it inside the metal over the skin depth  $1/\text{Im}\{k_z\} \approx c/\omega_p$ , which is typically much smaller than optical wavelengths. As the frequency of the radiation increases above the plasma frequency, the metallic response is lost, and the metal becomes transparent (except for possible interband transitions that are "encoded" in  $\varepsilon_b$ ).

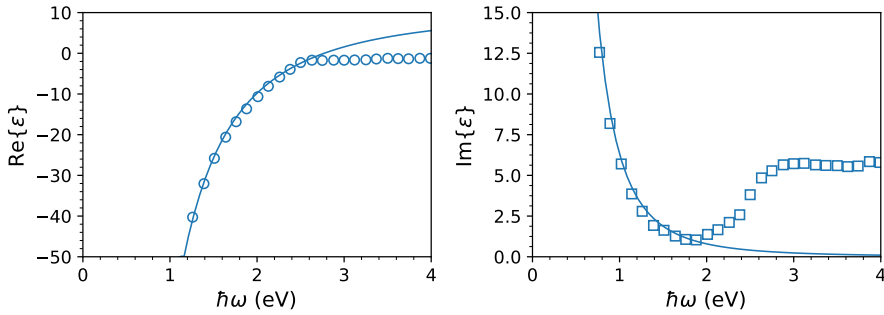


**Figure 3.1:** Dielectric function  $\varepsilon$  of gold. The experimental data are from Ref. [18]. The solid lines represent the Drude-dielectric function of Eq. (3.4) with  $\varepsilon_b = 1.070$ ,  $\omega_p = 1.377 \times 10^{16} \text{ s}^{-1}$ , and  $\Gamma = 1.175 \times 10^{14} \text{ s}^{-1}$ .

The dielectric function of gold is shown in Fig. 3.1. The data are from Ref. [18], and the solid line is obtained by fitting the Drude-dielectric function of Eq. (3.4) to the data below 2 eV (above 620 nm), where the Drude model accurately describes the optical response of gold. Deviations from the Drude model at higher energies is due to interband transitions [19], which is evident in the increase of the imaginary part of  $\varepsilon$ .

### 3.2 Localized surface plasmons

When a small metal particle is subjected to an external electrostatic field  $\mathbf{E}_{\text{ext}}$ , opposite charges accumulate at the particle surfaces (i.e. an excess of electrons at one side and a deficiency of electrons at the opposite side) as illustrated in Fig. 3.2(a). An internal field  $\mathbf{E}_{\text{int}}$  is produced inside the particle due to the surface charges. If the external field is suddenly removed, the internal field produces a current inside the particle, moving the excess electrons from one side of the particle to the opposite side. Electrons now accumulate at the other side of the particle, which produces an internal field and a current in the direction opposite the initial current flow. This oscillation continues until the motion is eventually damped by e.g. heat loss. The motion of the electrons evidently resembles a damped harmonic oscillator, which is apparent in the periodic modulation of the surface charge on the particle. This surface-charge oscillation is called a *localized surface plasmon* (LSP). The analogy of an LSP

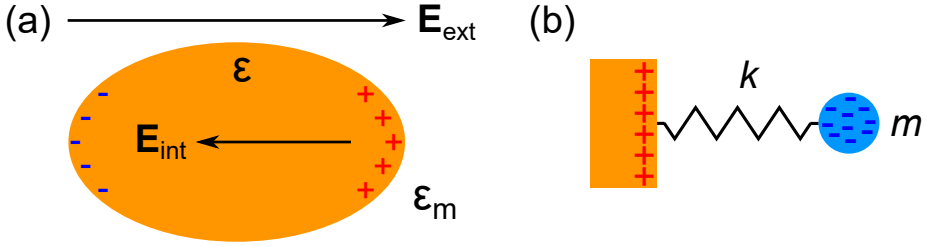


**Figure 3.2:** (a) An external electric field  $\mathbf{E}_{\text{ext}}$  applied across a metal particle (orange blob) is screened by induced surface charges on the particle, giving rise to a small internal electric field  $\mathbf{E}_{\text{int}}$  inside the particle. (b) The relaxation of the induced surface charges in the particle can be modeled as a damped harmonic motion (i.e. a spring system) with a characteristic frequency  $\sqrt{k/m}$ .

can be made with the spring system in Fig. 3.2(b), which has a characteristic (resonance) frequency  $\omega_0 = \sqrt{k/m}$ , where  $k$  is the spring constant, and  $m$  is the mass attached to the spring. The resonance frequency of an LSP is called a *localized surface plasmon resonance* (LSPR) frequency.

LSPs are typically associated with metallic (plasmonic) *nano*-particles, since coherent oscillations of the surface charge can only be excited by light of optical or near-infrared frequencies if the particle size is a few times smaller than the excitation wavelength.

Let us consider the action of a harmonic excitation at frequency  $\omega$  on the response of a metal nanoparticle. We assume that the size of the nanoparticle is much smaller than the wavelength, so that the phase of the applied field is the same everywhere inside the nanoparticle. Departure from this idealization gives rise to so-called retardation effects. Applying the conceptual model of a damped harmonic oscillator, the equation of motion for the electrons inside the nanoparticle reads [20]

$$m\ddot{\mathbf{r}} = -m\omega_0^2\mathbf{r} - m\Gamma\dot{\mathbf{r}} + \frac{2e^2}{3c^3}\ddot{\mathbf{r}} - e\mathbf{E}_{\text{ext}}. \quad (3.7)$$

The third term on the right is the Abraham-Lorentz force (or the radiation-reaction force) that accounts for radiation losses [14, p. 240]. The solution is readily obtained for the oscillating field  $\omega$ ; expressed in terms of the polarizability  $\alpha$  of the nanoparticle, defined by  $-e\mathbf{r} = \alpha\mathbf{E}_{\text{ext}}$ , we find:

$$\alpha(\omega) = \frac{e^2/m}{\omega_0^2 - \omega^2 - i\Gamma\omega - i2e^2\omega^3/3mc^3}. \quad (3.8)$$

The imaginary terms in denominator are responsible for damping of the LSP. Radiation damping can be included in an effective but slightly frequency-dependent scattering rate  $\Gamma' = \Gamma + 2e^2\omega^2/3mc^3$ . At optical frequencies,  $\Gamma' \approx \Gamma$ .

The polarizability displays a clear resonance (LSPR) around  $\omega_0$ . We can evaluate the electric near field of the LSP by associating it with an electric dipole with dipole moment  $\mathbf{p} = \alpha\mathbf{E}_{\text{ext}}$ . The induced near field in the direction of the external field, a distance  $z$  from the dipole center, is then

$$\mathbf{E}_{\text{ind}}(z, \omega) = \frac{1}{4\pi\epsilon_0} \frac{2\alpha(\omega)}{z^3} \mathbf{E}_{\text{ext}}. \quad (3.9)$$

The total field is  $\mathbf{E} = \mathbf{E}_{\text{ind}} + \mathbf{E}_{\text{ext}}$ . Large electric near fields may be produced by the LSPR due to enhanced polarizability and the small size (i.e. small  $z$ ). Specifically, we define *near-field enhancement* (NFE) as  $|\mathbf{E}|/|\mathbf{E}_{\text{ext}}|$ . The NFE is essentially due to the surface charge of the particle, and is particularly large when the excitation frequency matches the LSPR frequency. Note that the near field falls off rapidly away from the nanoparticle as  $1/z^3$ .

The harmonic oscillator model for the polarizability Eq. (3.8) is useful for a conceptual understanding, but it has no predictive power, because the LSPR frequency  $\omega_0$  appears as an undetermined parameter. In general, detailed numerical modeling must be carried out to determine the LSPRs. Analytic solutions exist only in very specialized cases.

### 3.2.1 A spherical nanoparticle

Maxwell's equations of a driven spherical particle can be solved analytically; the solution is known as the Lorenz-Mie-Debye solution. The detailed calculations can be found in [21]. Here, we will immediately simplify to small metal nanoparticles, where the problem can be solved by electrostatics.

Suppose the spherical nanoparticle has radius  $l$ , dielectric function  $\epsilon$ , and is embedded inside a homogeneous medium of dielectric constant  $\epsilon_m$ . The polarizability of the nanoparticle is [21, p. 139]:

$$\alpha(\omega) = 4\pi l^3 \frac{\epsilon(\omega) - \epsilon_m}{\epsilon(\omega) + 2\epsilon_m}. \quad (3.10)$$

The resonance condition is  $\text{Re}\{\epsilon(\omega)\} + 2\epsilon_m = 0$ , which is known as the Fröhlich condition. For the condition to be fulfilled in a dielectric environment, the nanoparticle has to be metallic (i.e.  $\text{Re}\{\epsilon\} < 0$ ). Plugging in the Drude-dielectric function Eq. (3.4) (setting  $\epsilon_b = 1$ ) we find that the LSPR frequency

$\omega_0$  of this spherical nanoparticle is

$$\omega_0 = \sqrt{\frac{\omega_p^2 - \Gamma^2(1 + 2\varepsilon_m)}{1 + 2\varepsilon_m}}. \quad (3.11)$$

We see that an increasing dielectric constant of the environment redshifts (decreases) the LSPR frequency. An increased loss rate (larger  $\Gamma$ ) has the same effect, which explains why the LSPR frequency of a silver nanoparticle is higher than that of a gold nanoparticle (which has a higher  $\Gamma$ ) of the same size.

### 3.2.2 Size-dependence of LSPRs

There is no explicit size dependence on the resonance condition for a small spherical nanoparticle, see the line below Eq. (3.10). This is due to the neglect of retardation effects. If such effects are included, to leading order in the particle size  $l$ , a redshift of the LSPR is found, which scales roughly as  $(l/\lambda)^2$  [20].

That is a general trend: larger nanoparticles have lower LSPR frequencies. This is easily understood based on the harmonic oscillator model displayed in Fig. 3.2; in large-sized particles, the distance between the two oppositely charged surfaces is greater, which leads to a smaller internal electric field. This corresponds to a smaller restoring force, i.e. a smaller spring constant  $k$ , and this reduces the resonance frequency of the system.

## 3.3 Absorption, scattering and extinction

A nanoparticle stimulated by light modifies not only the near-field zone [e.g. according to Eq.(3.9)], but also the far-field zone by producing radiation. It is customary to talk about the scattered electromagnetic field, which is defined as  $\mathbf{E}_s = \mathbf{E} - \mathbf{E}_{\text{inc}}$  (similarly for the magnetic field).  $\mathbf{E}_{\text{inc}}$  is the incident electric field that would appear without the nanoparticle, and  $\mathbf{E}$  is the total field obtained by solving Maxwell's equations *with* the nanoparticle excited by  $\mathbf{E}_{\text{inc}}$  [21].

The associated time-averaged Poynting vector of the full problem can be expressed as:

$$\langle \mathbf{S} \rangle = \mathbf{S}_{\text{inc}} + \mathbf{S}_s + \mathbf{S}_{\text{ext}}, \quad (3.12)$$

where

$$\mathbf{S}_{\text{inc}} = \frac{1}{2\mu_0} \text{Re}\{\mathbf{E}_{\text{inc}} \times \mathbf{B}_{\text{inc}}^*\}, \quad (3.13a)$$

$$\mathbf{S}_s = \frac{1}{2\mu_0} \operatorname{Re}\{\mathbf{E}_s \times \mathbf{B}_s^*\}, \quad (3.13b)$$

$$\mathbf{S}_{\text{ext}} = \frac{1}{2\mu_0} \operatorname{Re}\{\mathbf{E}_{\text{inc}} \times \mathbf{B}_s^* + \mathbf{E}_s \times \mathbf{B}_{\text{inc}}^*\}. \quad (3.13c)$$

The so-called extinction Poynting vector Eq. (3.13c) is a peculiar mixture of the the incident and scattered fields. Its meaning is revealed when we integrate  $\langle \mathbf{S} \rangle$  over a surface enclosing the nanoparticle, noting that this represents the absorption  $Q_a$  by the particle:<sup>2</sup>

$$Q_a = - \oint \mathbf{d}\mathbf{a} \cdot \langle \mathbf{S} \rangle = -Q_s - \oint \mathbf{d}\mathbf{a} \cdot \mathbf{S}_{\text{ext}}, \quad (3.14)$$

where  $Q_s = \oint \mathbf{d}\mathbf{a} \cdot \mathbf{S}_s$ . We assumed that the surrounding medium is nonabsorbing such that  $\oint \mathbf{d}\mathbf{a} \cdot \mathbf{S}_{\text{inc}} = 0$ . Setting  $Q_{\text{ext}} = - \oint \mathbf{d}\mathbf{a} \cdot \mathbf{S}_{\text{ext}}$ , we see that *extinction* is the energy absorbed and scattered by the particle:

$$Q_{\text{ext}} = Q_a + Q_s. \quad (3.15)$$

It is often helpful to work with cross sections  $\sigma = Q/A$ , where  $A$  is the cross section area of the nanoparticle.

Enhanced scattering and absorption (and hence extinction) by the nanoparticle happens near the LSPR. Since these quantities are relatively straightforward to measure experimentally, they are a valuable for performing spectroscopy on plasmonic nanoparticles. In Chapter 5.B.3 we describe how we measure extinction cross sections accurately. As usual, analytic expressions for the various cross sections cannot be found in general, but they exist for the small, spherical nanoparticle considered above. The cross sections are [21, p. 140]:

$$\sigma_a(\omega) = k \operatorname{Im}\{\alpha(\omega)\} = 4\pi k l^3 \operatorname{Im} \left\{ \frac{\varepsilon(\omega) - \varepsilon_m}{\varepsilon(\omega) + 2\varepsilon_m} \right\}, \quad (3.16a)$$

$$\sigma_s(\omega) = \frac{k^4}{6\pi} |\alpha|^2 = \frac{8}{3} \pi k^4 l^6 \left| \frac{\varepsilon(\omega) - \varepsilon_m}{\varepsilon(\omega) + 2\varepsilon_m} \right|^2. \quad (3.16b)$$

<sup>2</sup>Our convention is that  $\mathbf{d}\mathbf{a}$  points *outward* of the surface enclosing the nanoparticle, hence the explicit negative sign to ensure that  $Q_a \geq 0$ .

### 3.4 Far-field and near-field resonances

One could imagine that the resonance frequency at which the NFE of a plasmonic nanoparticle is largest coincides with the maximum extinction in the far field. This is not exactly true because of radiation damping and heat loss in the nanoparticle [22].

According to Eq. (3.9), the largest NFE is expected when  $|\alpha(\omega)|$  reaches its maximum value. From Eq. (3.8),

$$|\alpha(\omega)| = \frac{e^2/m}{\sqrt{(\omega_0^2 - \omega^2)^2 + \Gamma'^2 \omega^2}}. \quad (3.17)$$

It is straightforward to confirm that the maximum value is reached at

$$\omega_{\text{NFE}} = \sqrt{\omega_0^2 - \Gamma'^2/2}, \quad (3.18)$$

which is somewhat lower than the LSPR at  $\omega_0$ . A different way to arrive at the same result is to maximize the potential energy of the harmonic oscillator, which is associated with the surface charge, and therefore also NFE [22].

The resonance observed in the far field as maximal extinction is expected to coincide with peak absorption, which also enhances radiation. According to Eq. (2.13), absorption by the particle is proportional to  $\text{Re}\{\mathbf{j}^* \cdot \mathbf{E}_{\text{ind}}\} \propto \text{Im}\{\omega\alpha(\omega)\}$ .<sup>3</sup> Maximizing the absorption shows that the resonance frequency coincides with the LSPR at  $\omega_0$ .

Thus we see that the the resonances in the near field are slightly redshifted with respect to the LSPRs, which coincides with peaks in the extinction spectrum.

---

<sup>3</sup>This follows from Eq. (2.8) since  $\alpha$  and  $\chi$  are proportional. The absorption rate can also be obtained directly from Eq. (3.7) by calculating the work done by the damping force, see [22].

## ULTRASHORT LASER PULSES

Half of the nobel prize in physics 2018 was awarded jointly to Gérard Mourou and Donna Strickland “for their method of generating high-intensity, ultrashort optical pulses”.<sup>1</sup> Here, *ultrashort* refers to a timescale below a few hundreds of femtoseconds (fs). The technique they invented is called chirped-pulse amplification (CPA): An ultrashort laser pulse is stretched to ns durations such that it can be amplified to high pulse energies, after which it is recompressed to the original pulse duration. CPA avoids damaging of the amplifying laser crystals, in turn making it possible to achieve astonishing peak powers. The Extreme Light Infrastructure (ELI) recently achieved 10 PW with a CPA-based laser system producing  $\sim 100$  fs pulses, thus potentially achieving intensities in the order of  $10^{23}$  W cm<sup>-2</sup>.<sup>2</sup>

In this thesis we are concerned with much lower intensities, generally up to  $10^{14}$  W cm<sup>-2</sup>. Materials respond strongly to these intensities, often leading to irreversible damage. In this chapter, we will review the fundamentals of ultrashort laser-pulse interaction with matter in this intensity regime.

---

<sup>1</sup>The Nobel Prize in Physics 2018. NobelPrize.org. Nobel Media AB 2019. Tue. 9 Jul 2019. <https://www.nobelprize.org/prizes/physics/2018/summary/>.

<sup>2</sup>ELI-NP laser hits 10 petawatts peak power. Optics.org. 27. Mar 2019. <http://optics.org/news/10/3/41>.

## 4.1 Basic concepts

To produce ultrashort laser pulses, a broad laser gain medium is necessary. The archetypical fs laser (in research) is the titanium:sapphire (Ti:AlO<sub>2</sub>) laser, which is usually operated around 800 nm. Ultrashort laser pulses are produced via mode-locking, where the phases of the individual laser-cavity modes are locked together to provide the shortest achievable pulses. The temporal shape of the pulses depends on the gain profile of the laser crystal, which is typically approximately Gaussian around a central wavelength. This implies that the pulse shape is Gaussian in time as well, with a full-width half-maximum (FWHM)  $\tau$  defined as:

$$I(t) = I_0 e^{-(4 \ln 2) t^2 / \tau^2}. \quad (4.1)$$

Here,  $t$  is time, and  $I$  is the intensity (energy flux in the propagation direction) at a fixed point in space. For such a mode-locked Gaussian pulse,  $\tau \times \Delta\omega = 0.441$ , where  $\Delta\omega$  is the bandwidth (at FWHM) of the gain profile, and the pulse is said to be time-bandwidth limited (TBL). In general, when there is a slight phase mismatch between the modes,  $\tau > 0.441/\Delta\omega$ .

When ultrashort pulses propagate through a dispersive material, the individual frequency components are delayed with respect to each other, because they exhibit slightly different phase velocities [ $v = c/n(\omega)$ ] in the material. This gradually stretches the pulse in time (the phase relation between the frequency components is ruined). The duration of a TBL Gaussian pulse passing through a distance  $L$  in a material with refractive index  $n(\omega)$  is stretched to [23, p. 343]

$$\tau = \tau_0 \sqrt{1 + (16 \ln^2 2) L^2 \beta^2 / \tau_0^4}, \quad (4.2)$$

where  $\tau_0$  is the TBL pulse duration and  $\beta = \partial^2(n(\omega)\omega/c)/\partial\omega^2$  is the group-velocity dispersion (GVD) of the material, evaluated at the central (carrier) frequency of the pulse. The GVD at 800 nm of a typical glass (BK7) is  $\sim 45 \text{ fs}^2 \text{ mm}^{-1}$ . For  $L = 20 \text{ mm}$ , a 35 fs pulse is stretched to  $\sim 80 \text{ fs}$ . This highlights the deteriorating effect that dispersive optical elements might have on short laser pulses, which is important to keep in mind when designing an experiment.

The spatial profile of a laser can typically be described as a ‘‘Gaussian beam’’, formally called a TEM<sub>00</sub> mode. Suppose the beam propagates in the  $z$  direction and has a focal point at  $z = 0$  with *spot size*  $w_0$ . The intensity profile is then

$$I(\rho, z) = \tilde{I}_0(z) e^{-2\rho^2/w^2(z)}, \quad (4.3)$$

where  $\rho$  is a radial coordinate orthogonal to the  $z$ -axis, and

$$\tilde{I}_0(z) = I_0 \frac{w_0^2}{w^2(z)}, \quad w(z) = w_0 \sqrt{1 + z^2/z_R^2}. \quad (4.4)$$

The Rayleigh range  $z_R = \pi w_0^2/\lambda^2$  characterizes both the collimation depth, but also the divergence angle  $\vartheta = w(z)/z \approx w_0/z_R$  at large  $z$ .

In materials processing with short laser pulses, the relevant quantity is often the *fluence*  $F$ , which represents the total pulse energy per unit area delivered to a target. The fluence is defined as

$$F(\rho, z) = \int_{\text{pulse}} dt I(\rho, z, t). \quad (4.5)$$

For a temporal Gaussian-shaped pulse, we obtain

$$F(\rho, z) = \sqrt{\frac{\pi}{4 \ln 2}} I(\rho, z) \tau \approx 1.064 I(z, \rho) \tau. \quad (4.6)$$

Radial integration of the fluence gives the pulse energy  $E_p$ , which for a Gaussian beam establishes the following convenient relationship:

$$F_0(z) = \frac{2E_p}{\pi w^2(z)}. \quad (4.7)$$

## 4.2 Excitation of materials

An ultrashort light pulse interacts mainly with the electrons in atoms, as the nucleus is hardly affected due to its much higher inertia. Excitation of solids depends on the detailed electronic band structure, in particular whether the solid has a band gap (semiconductors and dielectrics) or not (metals).

### 4.2.1 Metals

In metals, light of essentially any wavelength can be absorbed because the partially filled electronic bands provide a continuum of states for the electrons to occupy. The electrons residing in the partially-filled bands are called “free carriers”. Absorption of light by these carriers is called *free-carrier absorption* (FCA). Actually, truly free charges cannot absorb photons because it is impossible to simultaneously conserve energy and momentum. In metals,

FCA proceeds mainly via inverse bremsstrahlung where a free carrier absorbs a photon while exchanging momentum with heavy ions through collisions. Thus, electrons near the Fermi level (energy  $E_F$ ) are elevated to higher energies in the band in steps of  $\hbar\omega$  by FCA. The process is illustrated in a simplified energy-band diagram in Fig. 4.1.

### 4.2.2 Semiconductors and dielectrics

In semiconductors and dielectrics for which the photon energies of the light pulse is lower than the band gap, absorption is initiated through *strong-field ionization* (SFI). SFI promotes valence-band (VB) electrons to the conduction band (CB), thereby producing *two* free carriers: an electron in the CB, and a hole in the VB. The two processes responsible for SFI are multiphoton absorption and tunnel ionization. Multiphoton absorption happens at “moderate” intensity, and typically scales with intensity to the power of the number of photons needed to bridge the band gap. At much higher intensities, the electric field of the pulse strongly perturbs the atomic potentials, allowing VB electrons to travel directly to the CB within a half-cycle of the laser field. The transition from the multiphoton regime at moderate intensities to the tunnel-ionization regime at high intensities is captured in an important analytical expression derived by L. V. Keldysh in 1965 [24]. In this model, the two regimes are distinguished in terms of the Keldysh parameter  $\gamma$ ; multiphoton absorption dominates when  $\gamma > 1$ , whereas tunnel ionization dominates when  $\gamma \ll 1$ . The Keldysh parameter is defined as

$$\gamma = \sqrt{\frac{E_g}{2U_p}}, \quad (4.8)$$

where  $E_g$  is the band gap, and  $U_p$  is the *ponderomotive energy*:

$$U_p \equiv \frac{e^2 E^2}{4m_e \omega^2} = (9.34 \text{ eV}) \times I [10^{14} \text{ W cm}^{-2}] \times \lambda^2 [\mu\text{m}^2]. \quad (4.9)$$

$U_p$  is the average potential energy of a free electron in an electric field  $E$  oscillating at frequency  $\omega$ . The right-hand side of Eq. (4.9) is convenient for quick evaluation of  $U_p$ . Evidently,  $U_p$  surpasses the photon energy for 800 nm at an intensity of  $2.6 \times 10^{13} \text{ W cm}^{-2}$ . Note that  $U_p$  increases the potential energy of free carriers, which means that this extra amount of energy must be

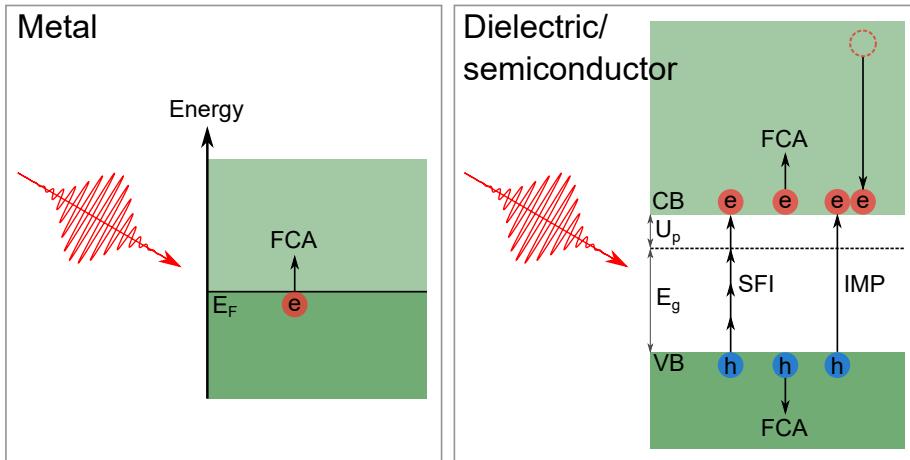


**Figure 4.1:** Ultrashort laser-pulse excitation of materials. *Left.* Excitation of metals. Electrons near the fermi level (energy  $E_F$ ) are promoted to states of higher energy via FCA as represented by the small upward arrow. *Right.* Excitation of a wide band gap material with pristine band gap  $E_g$ , which is shifted upwards by  $U_p$  due the strong electric field of the laser pulse. Excitation is initiated by SFI, creating e-h pairs. The free CB electrons and VB holes are heated by FCA to high energies. When the energy of a carrier exceeds the band gap, it may produce by additional e-h pairs through IMP.

supplied by the light pulse in order to excite electrons from the VB and CB. In other words,  $U_p$  effectively increases the band gap of the material.

SFI in band-gap materials is sketched Fig. 4.1. Immediately after SFI, the produced electron-hole (e-h) pairs are heated by FCA, which proceeds in the same way as in metals. For intense excitation pulses, FCA heats the carriers to very high energies, far exceeding the bandgap. These very hot electrons and holes can produce additional e-h pairs by *impact ionization* (IMP) where, e.g. an energetic electron collides with an atom, transferring a VB electron to the CB. IMP can lead to an avalanche effect (avalanche ionization), resulting in an excitation rate that may far exceed the SFI rate. The processes of FCA and IMP are illustrated in Fig. 4.1.

It is still debated how influential IMP actually is on ultrashort laser-pulse excitation of dielectrics; some authors report clear signatures of significant IMP [25–27], while other authors find no evidence thereof [28, 29]. The conflicting reports may in part be due to different laser conditions, as the detailed excitation dynamics depends strongly on e.g. peak intensity and pulse

duration. See for example [30] for an in-depth discussion on these issues.

### 4.3 Material relaxation: damage and ablation

SFI and FCA creates a highly nonequilibrium ensemble of carriers in metals and dielectrics, but fast electron-electron and electron-hole scattering nevertheless quickly establishes a local thermodynamic equilibrium of the free carriers within 1–10 fs. After thermalization, the carriers can be assigned a Fermi-Dirac distribution with a well-defined temperature  $T$  and chemical potential  $\mu$ .<sup>3</sup> On a longer time scale, typically 1–10 ps, the carrier system transfers energy to the lattice through inelastic electron-phonon scattering, which heats the ions in the solid to high temperatures. Strong temperature gradients emerge because of inhomogeneous laser-pulse excitation in the depth of the material. As a result, the lattice becomes thermodynamically unstable, and ablation – removal of atoms – may happen. It is an experimental fact that ablation (and similar types of permanent short-pulse laser-induced modifications) exhibit a certain threshold below which the material recovers without leading to ablation. Below the ablation threshold, transient phase transformations (such as a solid-liquid transition) may take place in the material, which eventually reverts to the solid phase after cooling, sometimes leading to unique frozen-in metastable solid states [31, 32].

The material relaxation following strong laser excitation is an extremely complex topic, where small and large time- and spatial scales all are important for the final outcome. As a result, laser-induced material modifications depend strongly on the material properties and the excitation conditions. It is not the purpose here to give a complete overview of this subject – we refer instead to a recent review [31].

However, there are a few general differences between ablation of metals and dielectrics that are worth highlighting. In metals, ablation is typically hydrodynamic in nature, i.e. dependent on temperature or pressure of the excited state of the solid. Photomechanical spallation is one such ablation process that we discuss in Chapter 7. In contrast, ablation of dielectrics typically entails a significant depletion of the occupation of the VB, which strongly affects the bonding between atoms in the solid. This can lead to ultrafast, so-called non-thermal processes, such as a breakdown of the lattice

---

<sup>3</sup>In band-gap materials, one should assign separate Fermi-Dirac distributions to the CB and VB, which, however, eventually equilibrates to a common temperature and chemical potential.

while it remains cold. One example of a non-thermal ablation process is Coulomb explosion [33–35], which we consider in more detail in Chapter 8.



## NEAR-FIELD MARKING ON $\text{TiO}_2$

A major goal of my thesis is to experimentally verify numerical electric-field calculations of plasmonic nanoparticles. The results presented below is based on our first published validation of such calculations [1]. We named the technique “near-field marking”, because it involves characterizing modifications (in this case ablation) around nanoparticles, produced by strong electric near-field enhancements (NFEs).

### 5.1 Background

As mentioned in Section 1.4, we initially tried to carry out the near-field measurement by placing gold nanoparticles on top of  $\text{Ge}_2\text{Sb}_2\text{Te}_5$  (GST) thin films, looking for amorphization of GST caused by the strong electric near fields around laser-irradiated nanoparticles. This, however, was unsuccessful for the reasons described later in Section 7.3. We therefore adopted the original approach proposed in Ref. [8] by instead relying on ablation, in our case of GST. Following this approach, we rarely saw NFEs greater than  $\sim 2$ .

The reason for the low NFEs on GST took some time to realize, but it is related to the curious optical properties of GST: at 1500 nm, the complex refractive index is  $n_{\text{GST}} = 7.0 + 1.3i$ ; this is huge! Compare this to  $n_{\text{TiO}_2} = 2.4$

for TiO<sub>2</sub>. We know that a higher refractive index generally redshifts the LSPRs of nanoparticles by an amount proportional to  $n$  [see e.g. Eq. (3.11)]. If a nanoparticle is designed to have a LSPR at 1500 nm on TiO<sub>2</sub> – i.e. for improved upconversion of Er<sup>3+</sup> doped into this material – then replacing TiO<sub>2</sub> with GST redshifts the LSPR well above 3000 nm. This implies that our early measurements on GST (1300–2000 nm) must have been off-resonant by a fantastic amount.

Thus we completely abandoned the use of GST for near-field marking. Instead, we carried out the procedure on TiO<sub>2</sub> with ablation. A few nanoparticle designs had previously been optimized to give enhanced upconversion yield (UCY) in TiO<sub>2</sub>:Er<sup>3+</sup> films. At the time, the 3D topology optimization (TopOpt) code was not ready, so particle geometries were optimized by the following – presumably common – approach: Guess a shape of a nanoparticle (preferably something with pointy antenna-like features to get large near-field concentrations), parameterize the shape according to a few parameters (e.g. radius and height for a disk), identify an objective function (e.g. maximization of total UCY in a certain volume), and feed it to an optimization routine. In the case described here, we guessed that star-shaped nanoparticles would produce large NFEs. Eventually we settled on five-legged “nanostars”, which we then investigated the near-field properties of below. It turned out later that this geometry was worse than simple disks in terms of UCY. This basically underlines how bad our intuition might be about optics on the nanoscale, and thus why the envisioned TopOpt approach towards generating nanoparticle designs is a promising way forward.

## 5.2 Contribution

My contributions to the article consisted of writing most of the text, producing all the figures, and carrying out all of the measurements. Adnan Nazir fabricated the nanoparticles, which also involved a fair bit of optimization on his part. Emil H. Eriksen and Joakim Vester-Petersen carried out the numerical calculations.

The publication [1] is included in the following with minor changes to the layout and labeling of sections, equations, and references.

## Near-field marking of gold nanostars by ultrashort pulsed laser irradiation: experiment and simulations

Søren H. Møller<sup>1</sup>, Joakim Vester-Petersen<sup>2</sup>, Adnan Nazir<sup>1</sup>, Emil H. Eriksen<sup>1</sup>, Brian Julsgaard<sup>1,3</sup>, Søren P. Madsen<sup>2</sup>, and Peter Balling<sup>1,3</sup>

<sup>1</sup> Department of Physics and Astronomy, Aarhus University, Ny Munkegade 120, DK-8000 Aarhus C, Denmark

<sup>2</sup> Department of Engineering, Aarhus University, Inge Lehmanns Gade 10, DK-8000 Aarhus C, Denmark

<sup>3</sup> Interdisciplinary Nanoscience Center, Aarhus University, Gustav Wiedes Vej 14, DK-8000 Aarhus C, Denmark

**Abstract:** Quantitative measurements of the electric near-field distribution of star-shaped gold nanoparticles have been performed by femtosecond laser ablation. Measurements were carried out on and off the plasmon resonance. A detailed comparison with numerical simulations of the electric fields is presented. Semi-quantitative agreement is found, with slight systematic differences between experimentally observed and simulated near-field patterns close to strong electric-field gradients. The deviations are attributed to carrier transport preceding ablation.

### 5.A Introduction

Freely propagating electromagnetic waves are subject to the diffraction limit which fundamentally constrains our ability to focus light down to a spot smaller than roughly half of the wavelength. Metal nanostructures can bypass this limitation due to their ability to convert the freely propagating waves into evanescent waves [16], i.e. strongly damped waves that exist only along interfaces or inhomogeneities [14]. For metal nanoparticles (NPs), so-called localized surface plasmon resonances (LSPRs) are coupled light-matter modes consisting of strong evanescent waves that dominate the near-field zone of the NPs, resulting in nanoscale light confinement with very high field-magnitudes [36]. The ability to change the values of the LSPR frequencies of NPs, by changing their size, shape, and dielectric environment [37, 38], makes it possible to tailor the NPs for specific applications, e.g. sensing [39], photovoltaics [40], and nonlinear optics [41].

When the NPs are larger than roughly 10 nm, quantum mechanical effects are negligible [42], in which case the macroscopic Maxwell equations can be used to predict the electromagnetic field distribution. Such classical simulations are usually validated by the far-field optical properties [43] or some response

that depends strongly on the local electric field, e.g. a surface-enhanced Raman signal [44] or upconversion luminescence [45]. Even if simulations agree on measured cross sections in the far field, this does not imply that the simulations are correct in the near-field zone [21]. For instance, a Raman-enhancement signal gives at best an average view of the field enhancement. Scanning near-field optical microscopy (SNOM) is one of the earlier techniques for imaging electric fields with nanoscale resolution [46]. The challenge with SNOM is, however, that the measured signal depends strongly on the tip-sample interaction; this interaction must somehow be subtracted from the signal to obtain an image of the actual fields in the absence of the tip, but this is very hard to do in practice [9, 14]. Techniques based on electron-energy-loss spectroscopy (EELS) and cathodoluminescence (CL) [47, 48] are very useful as they image the plasmon modes with a resolution set by an electron microscope (down to a few nm or better). The drawback in EELS and CL is that high-energetic electrons excite the plasmon modes, and therefore a comparison to low-energetic optical excitation of plasmons, as utilized in most applications and also calculated in most simulations, is not always straightforward [9]. A different approach is to image electric near-field enhancements (NFEs) by permanently modifying the environment around the NPs by pulsed laser-irradiation; the modifications can be ablation [8, 49, 50], phase-change [10, 11], or polymerization [51, 52] of the underlying or embedding material. The advantage of such techniques is that they potentially provide quantitative NFEs directly comparable to electromagnetic simulations with nm resolution. We will refer to such techniques as “near-field marking” in the following.

In this work we compare, quantitatively, measured and simulated electric field distributions around gold nanostars (from now on referred to as NPs), placed on top of a thin film of Er-doped TiO<sub>2</sub> (TiO<sub>2</sub>:Er<sup>3+</sup>), by pulsed femtosecond-laser ablation. The advantage of laser ablation, as compared to phase-change and polymerization, is that it can be performed on any material without any precautions. Near-field measurements on TiO<sub>2</sub>:Er<sup>3+</sup> are carried out in order to validate numerical electric-field simulations that are used for optimizing plasmonic nanostructures for enhanced Er-upconversion (see e.g. [45]). By tuning the laser wavelength, we measure the NFE in space on and off the plasmon resonance. We find that the results in each case agree semi-quantitatively with electric-field simulations, however we observe a slight systematic difference between observed and simulated near-field patterns near the NP edges. The discrepancy is attributed to diffusion, and carrier-related scattering in TiO<sub>2</sub> taking place before ablation is initiated. Consequently, the

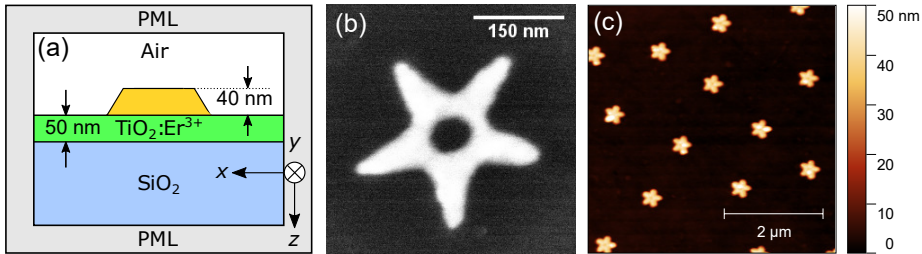


**Figure 5.1:** Illustration of the sample and NP details. (a) Schematic side-view of the sample with a single NP on top. This domain is used in the simulations; see Section 5.B.2 for details. (b) Top-down SEM image of one of the identically fabricated NPs. (c) AFM image showing an overview of part of the distribution of NPs.

near-field marking technique has the potential to study these phenomena on a nanometer length scale.

## 5.B Methods

### 5.B.1 Sample fabrication

A 50 nm thick  $\text{Er}^{3+}$ -doped  $\text{TiO}_2$  film was deposited on top of a 0.5 mm thick fused quartz substrate by radio-frequency magnetron sputtering. A random distribution of identical gold NPs was fabricated with electron beam lithography (EBL) on top of the  $\text{TiO}_2$  film on a  $500 \mu\text{m} \times 500 \mu\text{m}$  area in the center of the film. The sample is sketched in Fig. 5.1(a) together with a scanning electron microscope (SEM) image of the NP geometry on Fig. 5.1(b); the NP is a star with five legs, a height of approximately 40 nm with an outer diameter of about 320 nm and a hole of diameter 65 nm. The fabrication details are identical to those reported by us elsewhere [45]. The NP dimensions were chosen so as to have a LSPR around 1500 nm. An atomic force microscope (AFM) image of the NPs are shown in Fig. 5.1(c). The area that each NP occupy on average is  $a_{\text{NP}} = 1.67 \mu\text{m}^2$ .

### 5.B.2 Simulations

Fig. 5.1(a) depicts a 2D cross section of the computational domain consisting of a single gold NP on top of the  $\text{TiO}_2$ -quartz sample. The NP is modeled using a contour trace  $(x, y)$  from the SEM image shown in Fig. 5.1 (b) which

is extruded to a height of 40 nm. The size of the computational domain is  $2\ \mu\text{m} \times 2\ \mu\text{m} \times 2\ \mu\text{m}$  and is truncated by perfectly matched layers (PMLs) [53] in order to efficiently model the electric field distribution for a single NP while reducing artificial reflections from the boundary. Particle-particle interactions are neglected, which is a reasonable assumption when the  $\text{TiO}_2:\text{Er}^{3+}$  film is sufficiently thin [54].

For non-magnetic, isotropic, and linear media, the model is governed by the time-harmonic electric-field wave equation

$$\nabla \times (\nabla \times \mathbf{E}) + \tilde{\epsilon}_r k_0^2 \mathbf{E} = \mathbf{0}, \quad (5.1)$$

where  $\mathbf{E}$  is the total electric field,  $\tilde{\epsilon}_r$  is the complex relative electric permittivity, and  $k_0$  is the free-space wavenumber. The model is excited using the scattering-field formulation [55] where  $\mathbf{E}$  is given as the superposition of the background field  $\mathbf{E}_b$  and the scattered field,  $\mathbf{E}_s$ , as

$$\mathbf{E} = \mathbf{E}_b + \mathbf{E}_s. \quad (5.2)$$

The background field is obtained analytically via the transfer matrix method [56] for the situation without any scatterer present in the model. Here, a normally-incident plane wave propagates in the positive  $z$ -direction, linearly polarized in either the  $x$ - or  $y$ -direction, cf. Fig. 5.1(a). The scattered field is obtained by substitution of Eq. (5.2) into Eq. (5.1)

$$\nabla \times (\nabla \times \mathbf{E}_s) + \tilde{\epsilon}_r k_0^2 \mathbf{E}_s = -\nabla \times (\nabla \times \mathbf{E}_b) - \tilde{\epsilon}_r k_0^2 \mathbf{E}_b, \quad (5.3)$$

and solving for  $\mathbf{E}_s$  numerically using the finite element method. The refractive indices for Au and  $\text{SiO}_2$  are taken from [18] and [57], respectively, while values for  $\text{TiO}_2:\text{Er}^{3+}$  were experimentally obtained using ellipsometry.

Note, that for an incident laser pulse, the correct solution is a convolution between the monochromatic time-harmonic solutions and the pulse spectrum. If the NP response spectrum is broad compared to the pulse spectrum, which is the case here (see Section 5.C), a single monochromatic solution is sufficient for modelling the pulse.

The extinction cross section of the NP is given by

$$\sigma_{\text{ext}} = \sigma_{\text{abs}} + \sigma_{\text{sct}}, \quad (5.4)$$

where  $\sigma_{\text{abs}}$  and  $\sigma_{\text{sct}}$  are the absorption and scattering cross sections, respectively, obtained via

$$\begin{aligned}\sigma_{\text{abs}} &= \frac{1}{I_0} \iiint_{V_{\text{NP}}} \mathbf{J} \cdot \mathbf{E} \, dV_{\text{NP}}, \\ \sigma_{\text{sct}} &= \frac{1}{I_0} \iint_{\Omega_{\text{NP}}} \mathbf{n} \cdot \langle \mathbf{S}_{\text{sct}} \rangle \, d\Omega_{\text{NP}}.\end{aligned}\tag{5.5}$$

Here  $I_0$  is the intensity of the incoming plane wave,  $\mathbf{J}$ , is the current density induced by the electric field, and  $\mathbf{n}$  is a unit vector normal to the surface of the NP. The time averaged poynting vector of the scattered field,  $\langle \mathbf{S}_{\text{sct}} \rangle$ , is defined by the poynting vector of the total- and background fields as  $\langle \mathbf{S}_{\text{sct}} \rangle = \langle \mathbf{S} \rangle - \langle \mathbf{S}_{\text{b}} \rangle$ .  $V_{\text{NP}}$  and  $\Omega_{\text{NP}}$  are the volume and surface of the nanostar, respectively.

The software package COMSOL Multiphysics [58] version 5.3 was used to implement the model, solve for the scattered field distribution as well as calculating  $\sigma_{\text{ext}}$ . The model is discretized by nonuniform quadratic tetrahedral Nedélic elements [53]. The maximum element size is scaled according to the wavelength in each material domain as  $\lambda/6$  ( $\lambda$  is the material-dependent wavelength) in order to resolve the electric field oscillation. To resolve high gradients close to the NP surface, the mesh resolution is increased by a factor of 10.

### 5.B.3 Optical measurements

An extinction spectrum of the NPs was recorded in a spectrophotometer by measuring the transmission through the sample on and off the NPs. The difference in the two transmission measurements yields the extinction due to the NPs. The reason for this is the following: it can be shown that the power,  $P$ , in the forward direction measured in the far field on a small detector, yet large enough to contain many interference fringes of the scattered beam, is [21]

$$P = I_i a - \sigma_{\text{ext}} I_i + I_s a / (k_0 r)^2.\tag{5.6}$$

Here  $I_i$  is the incident beam intensity,  $I_s$  the scattered beam intensity in the forward direction, and  $r$  the sample–detection distance. The quantity  $a$  represents the detection area. The derivation given in [21] is valid for NPs in homogeneous space. When the NPs are situated on top of a layered structure, the incident intensity must be replaced by the transmitted intensity  $I_{\text{b}}$  of the

structure without NPs. Ignoring the scattering term in Eq. (5.6), which is negligible in the far field, the extinction cross section is thus given by

$$\sigma_{\text{ext}} = a(T_{\text{b}} - T_{\text{NP}}), \quad (5.7)$$

where  $T_{\text{b}}$  and  $T_{\text{NP}}$  are the transmittance in absence and presence of the NPs, respectively. Here, Eq. (5.7) is the total extinction cross section. For  $N$  identical NPs (ignoring particle-particle couplings), the cross section of a single NP is  $\sigma_{\text{ext},1} = \sigma_{\text{ext}}/N$ . In our setup,  $a$  corresponds to the illuminated area on the sample because all the forward-scattered light is captured by the detector. The final expression for the single-NP extinction cross section is thus

$$\sigma_{\text{ext},1} = a_{\text{NP}}(T_{\text{b}} - T_{\text{NP}}), \quad (5.8)$$

where  $a_{\text{NP}} = a/N = 1.67 \mu\text{m}^2$  is the area that each NP covers on average.

#### 5.B.4 Near-field marking

The experimental setup for near-field marking is as follows. Part of the output of a regeneratively amplified Ti:Sapphire (35 fs, average pulse energy 0.5 mJ) is used to pump an optical parametric amplifier (TOPAS), thus providing femtosecond pulses with a tunable wavelength in the range 1160 nm to 2600 nm. Pulse energies are measured by a fast, calibrated photodiode and adjusted by absorptive optical density filters. Single laser pulses are focused onto the sample by an achromatic lens (focal length 45 mm) at normal incidence. The focused beam radius (at  $1/e^2$ ) is between 8  $\mu\text{m}$  to 9  $\mu\text{m}$ , while typical fluences range from 0.5 J cm<sup>-2</sup> to 2 J cm<sup>-2</sup>.

The idea of the near-field marking method is to permanently mark the near-field zone of the NPs onto the underlying TiO<sub>2</sub> film by field-enhanced laser ablation. It is therefore crucial to determine the ablation threshold and the spatial laser-beam parameters. The beam from the TOPAS is in our situation to a very good approximation Gaussian, however it can be slightly elliptic. In the general case, the spatial fluence profile in the focal plane at the sample surface is described as

$$F(x, y) = F_0 \exp\left(-2x^2/w_x^2 - 2y^2/w_y^2\right), \quad (5.9)$$

where  $F_0$  is the peak fluence, and  $w_x$  and  $w_y$  are the beam radii in the  $x$  and  $y$  directions chosen to lie along the major and minor axes of the elliptic spot.

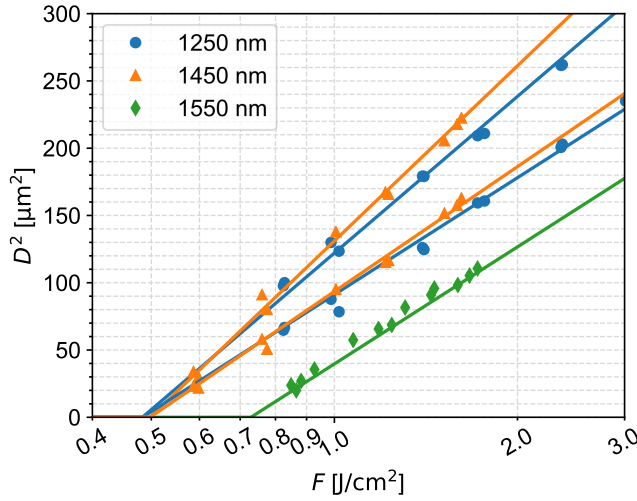


**Figure 5.2:** Plot of diameter,  $D$ , squared versus fluence,  $F$ . The threshold fluence for ablation and the laser beam radii are obtained from fits (solid lines) to the data (cf. Eq. (5.10)).

The relation between peak fluence and pulse energy,  $E_p$ , as measured by the photodiode, is  $F_0 = 2E_p/\pi w_x w_y$ . A simple technique due to Liu [59] for determining both the ablation threshold,  $F_{th}$ , and the beam radius is used here, wherein a series of holes is ablated in  $\text{TiO}_2$  at different energies. By measuring the major and minor diameters of the holes, the ablation threshold and the beam radii can be extracted by simultaneously fitting the data to the following two curves:

$$\begin{aligned} D_x^2 &= 2w_x^2 \ln(F_0/F_{th}), \\ D_y^2 &= 2w_y^2 \ln(F_0/F_{th}). \end{aligned} \quad (5.10)$$

The values  $w_x$ ,  $w_y$ , and  $F_{th}$  are extracted from the fits to the model shown in Fig. 5.2 for wavelengths 1250 nm, 1450 nm, and 1550 nm, respectively; the associated threshold fluences are, respectively,  $480 \pm 30 \text{ mJ cm}^{-2}$ ,  $500 \pm 30 \text{ mJ cm}^{-2}$ , and  $730 \pm 50 \text{ mJ cm}^{-2}$ . In the case of 1550 nm, the laser spot was circular, so only a single straight line was used in the fit. We attribute the larger threshold at 1550 nm to a change in photonic order for bridging the band gap ( $\sim 3.4 \text{ eV}$  as obtained from ellipsometry measurements).

Once the laser beam and ablation threshold of the  $\text{TiO}_2$  film have been

characterized, the NPs are irradiated by a single pulse above the ablation threshold. The presence of the ablation crater is useful for finding the center of the irradiated spot, and for checking that the measured pulse energy is consistent with the energy calculated from the crater size. Outside the ablation crater, where  $F(x, y) < F_{\text{th}}$ , nanoscale ablation craters appear around the NPs due to field-enhancement effects, see Fig. 5.3(a). The NFE (near-field enhancement), defined here as  $\text{NFE}(x, y) = \sqrt{F_{\text{th}}/F(x, y)}$ , can thus be calculated and related to a contour line corresponding to the ablation crater. By selecting NPs at different distances from the center of the spot, multiple field-enhancement contours can be traced out from a single laser-irradiated spot. To improve the statistics of the final contour lines, we stack several (4 or more) images of field-enhanced ablation craters, which are roughly at the same distance from the center of the spot. Stacking and alignment of the images is performed with AutoStakkert [60]. The final contour lines are traced on the resulting image. The process is illustrated in the bottom of Fig. 5.3(b); the darker areas, outlined by red, indicate ablation. The bright areas outside the lineouts represent a combination of the edges of the ablation craters, and leftover residues from the gold NPs. There is some potential ambiguity as to where contours are drawn. We have chosen to draw consistently the lines slightly outside the edge of the ablation crater (see e.g. Fig. 5.3(b)). The contours are made 4 nm thick to reflect this ambiguity. Note that in the present case, the NPs showing near-field-induced ablation are all removed by the laser pulse due to the relatively high ablation threshold of TiO<sub>2</sub>. The fluence for removal of NPs is estimated to be about  $10 \text{ mJ cm}^{-2}$  to  $30 \text{ mJ cm}^{-2}$ . This fits well with the expected melting threshold of the nanostars ( $\sim 10 \text{ mJ cm}^{-2}$ ), so most likely the NPs are ejected from the film when they contract to nanodroplets [61]. Note that melting and NP-ejection happens only on a much longer time scale (ps to ns) compared to the pulse duration (fs), hence the measured near-field distribution will remain unaffected.

## 5.C Results and discussion

A comparison between the measured and simulated single-NP extinction cross section is shown in Fig. 5.4(a). Both measurements and simulations are for unpolarized light normally incident on the sample. The measured peak, and hence the LSPR, is located at 1560 nm. Two simulated curves are shown: one labelled 90°, which means that the geometry of the NP (based on thresholding

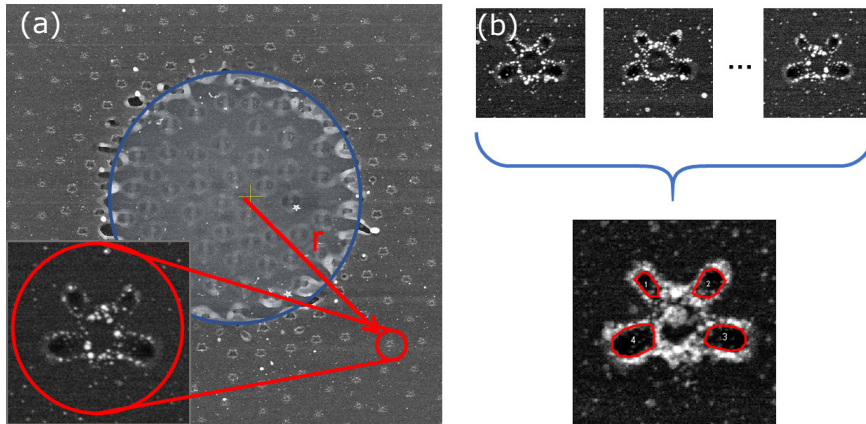


**Figure 5.3:** SEM images of irradiated NPs. (a) Ablation crater produced by single-shot irradiation at 1550 nm and a peak fluence of  $1.4 \text{ J cm}^{-2}$ . NPs close to the center of the spot are removed, leaving behind nanoscale ablation craters due to NFE as shown in the blow-up. (b) The near-fields of different NPs, all irradiated with approximately the same fluences, are stacked together to obtain an average whose contours for NFE are traced by red.

actual SEM images) is simply extruded perpendicularly to the plane of the substrate. The resulting NP is shown in Fig. 5.4(b). The other curve, labelled  $70^\circ$ , was calculated by tapering the NP  $70^\circ$  with respect to the substrate plane; the tapered geometry is shown in Fig. 5.4(c). The reason for considering this NP geometry is to also account for the fact that NPs fabricated by a lithography process become tapered during the evaporation step [62]. We have seen previously, under identical fabrication parameters, that the tapering angle ranges somewhere between  $60^\circ$  to  $80^\circ$  [45], hence  $70^\circ$  is a reasonable value. Indeed, the simulations at this angle fit almost perfectly the measured extinction. Tapering the NP further redshifts the LSPR; this is a general feature because, effectively, the NP's (average) height is reduced [63].

The results from the near-field measurements are studied by lines of constant NFE (near-field enhancement) shown in Fig. 5.5(a)-(c) for incident wavelengths of 1250 nm (a), 1450 nm (b), and 1550 nm (c). We remark that the spectrum of the femtosecond pulses is roughly 60 nm broad (full-width at half-maximum), however, this is narrow compared to the spectrum of the NP response (c.f. Fig. 5.4(a)). Therefore, we will consider only the central wavelength of the laser pulse in the following. The polarization is horizontal,

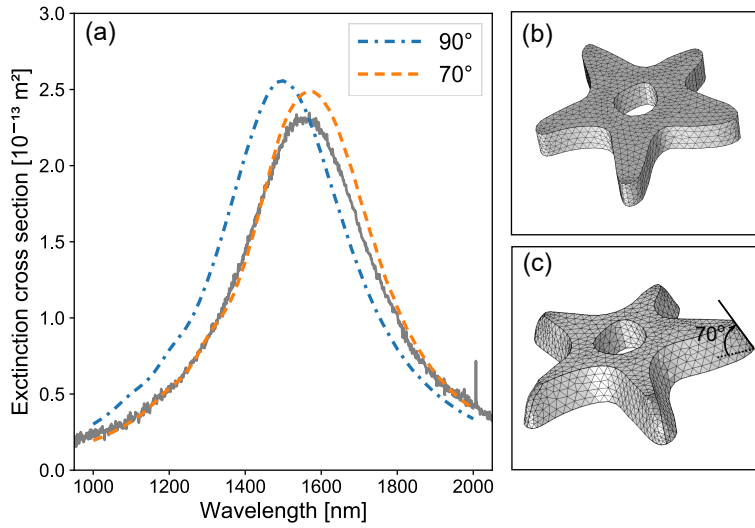


**Figure 5.4:** Measured (gray full) and simulated (blue dash-dotted and orange dashed) extinction cross section curves. The simulated curves are labelled according to their tapering angles,  $90^\circ$  and  $70^\circ$ ; the corresponding NP geometries, as implemented in the simulations, are shown in (b) and (c), respectively.

as indicated by the black arrow. We estimate that the uncertainty of the measured values of NFE is up to 25%. (The uncertainty is due to tight focusing of the laser beam, producing a slight gradient in the incident fluence across NPs.) The corresponding simulations, shown in Fig. 5.5(d)-(f), were performed for the  $70^\circ$  tapered NPs (Fig. 5.4(c)); the field is shown in the upmost part of the  $\text{TiO}_2$  film where ablation is initiated. The color scales indicate NFE, which in the simulations is defined as  $|\mathbf{E}_s|/|\mathbf{E}_b|$ . The color scale is the same in all panels; it is truncated to the maximal measured NFE in order to facilitate comparison between experiment and simulations. (Simulations have a tendency to show large NFEs very close to the NP that grows in magnitude with finer mesh resolution.) We see immediately, both in experiment and simulations, that the NFE is much smaller at 1250 nm than at 1450 nm and 1550 nm. This is expected because 1250 nm is relatively far off resonance, cf. Fig. 5.4. The simulations predict that the NFE is higher at 1550 nm, (which is very close the measured LSRP at 1560 nm), however the measurements do not clearly show the difference between 1450 nm and 1550 nm. In all cases, the two upper

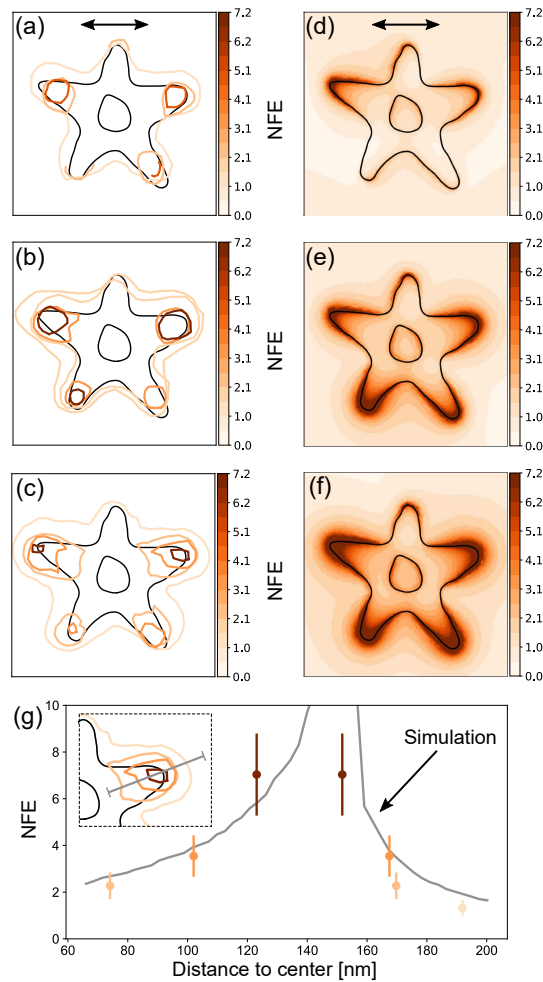


**Figure 5.5:** Comparison between measured and simulated near-field distributions. The left column, (a)-(c), shows lines of constant NFE obtained from the near-field-marking procedure. The wavelength of the exciting light was 1250 nm (a), 1450 nm (b), and for 1550 nm (c). Panels (a)-(f) each have dimensions 400 nm  $\times$  400 nm. The polarization is the same and is indicated by the arrow in (a) and (d). The right column, (d)-(f), displays the simulated near-field distribution at the surface of the TiO<sub>2</sub> film. The color scale indicates the NFE. Note that the scale is the same in panels (a)-(f) and is truncated at 7.2. (g) Measured and simulated NFE for 1550 nm excitation along a line bisecting the upper-right leg of the nanostar as indicated in the inset.

legs that are best aligned with the polarization, concentrate the incident light more strongly, resulting in larger magnitudes of NFE in close agreement with the simulated values.

Fig. 5.5(g) shows the NFE as observed at 1550 nm along a line bisecting the upper-right leg of the nanostar (see the inset in Fig. 5.5(g)). There is fairly good agreement between the measured and simulated values away from the edge of the NP. The difference is up to 50%, yet the asymmetric trends on each side of the NP's edge are well reproduced. Around the edge, the calculated NFE reaches values of up to 25 in a very small region which could not be resolved experimentally. We see in all cases from Fig. 5.5 a systematic shift of the measured NFEs toward the center of the NP. In addition, the measured NFEs are somewhat lower than the simulated values. In order to explain these discrepancies, we emphasize that absorption of the laser pulse in the TiO<sub>2</sub> (which in the simplest case is proportional to  $|\mathbf{E}_0|^{2n}$  where  $|\mathbf{E}_0|$  is the peak electric field inside the material due to the pulse, and  $n$  is the number of photons needed to bridge the band gap) is only the first step in the process leading to ablation. Absorption in TiO<sub>2</sub> proceeds by exciting electrons across the band gap. The excited electrons are then subsequently heated via inverse bremsstrahlung for the remainder of the pulse duration. If the excited electrons are sufficiently hot, impact ionization may proceed, further exciting electrons across the band gap. For macroscopic ablation to occur, the electrons (and holes) must transfer their energy to the lattice. This happens generally after the first few or few tens of ps. In the meantime, the initially absorbed energy density, as to be compared with the electric field simulations, is smeared out due to diffusion (or possibly ballistic transport) of electrons and holes. Consequently, the energy transferred to the lattice is smeared out, and this can explain why very localized NFEs cannot be resolved sufficiently due to unusually large gradients. Indeed, carrier transport can qualitatively explain the experimentally observed shifts of NFEs toward the center of the NP; large initial gradients in electron density along the edge of a leg will lead to piling up of electrons beneath it. However, carrier transport alone cannot explain the observed, systematically small values of NFE close to the NP edges. One important effect, which has been shown to be crucial in explaining ablation patterns around gold nanorods [64], is electron-phonon screening due to high electron densities which greatly reduces the rate of energy transfer between the electrons and the lattice. Hence, at positions of sufficiently large NFE, where most excited electrons reside initially, energy transfer to the lattice is slower. This allows more time for the transport mechanisms to redistribute the energy.

In addition, recombination of carriers at the gold interface may play a role for energy losses in  $\text{TiO}_2$ , especially when the electron-phonon coupling is weakened by the high carrier concentration. The details of the carrier-lattice dynamics will be the topic of future investigations, e.g. by comparing to detailed modelling in an extended two-temperature model [65]. Comparison with detailed simulations will help illuminate which processes dominate the dynamics leading to ablation (e.g. diffusion or ballistic transport). Such a combined study will provide a means for precisely calculating dynamical properties of carrier transport due to the nm resolution available by the current experimental technique.

For validation of electric-field simulations, the experimental technique shows that the trends from the simulations are well-produced. The principal resolution of the technique is a few nanometers. However, as seen clearly from Fig. 5.5(g), the experimentally observed NFEs can be shifted by about 10 nm close to strong electric-field gradients for the reasons discussed above. The ultimate resolution of the technique will probably depend on the substrate material. To further increase the spatial resolution of the technique, detailed modelling of the carrier transport must be applied. Away from strong electric-field gradients, semi-quantitative agreement is obtained where the measured NFEs may be up to 50 % lower than the simulated values. The major advantage of this technique is that it can be applied to any material.

## 5.D Conclusion

We have studied experimentally the electric near-field distribution around star-shaped gold nanoparticles by ablation of an underlying  $\text{TiO}_2$  film using a tunable femtosecond laser. The technique provides quantitative measurements of the spatial distribution of electric-field enhancement on and off the plasmon resonance with nanometer resolution. We found good semi-quantitative agreement with electric-field simulations, with some systematic differences in the spatial patterns and values of field enhancement close to strong electric-field gradients. The disagreement can be attributed to the photoexcited carrier transport preceding the ablation process. In future work we will investigate the effect of the carrier transport in details to clarify the discrepancies between experiment and simulations. The near-field marking technique used in this work can potentially be applied to study further the carrier dynamics by carefully designed nanostructures.

**Acknowledgements** Harish Lakhotiya is gratefully acknowledged for producing the  $\text{TiO}_2\text{:Er}^{3+}$  films. This work was funded by Innovation Fund Denmark through the SunTune project.

---

### 5.3 Comments

It was only after publication of the paper that I became aware of Ref. [22], where the authors argued that the resonance frequency of maximum NFE is redshifted with respect to the LSPR frequency. The latter coincides with the observed peak extinction in Fig. 5.4. The argument is simple, and was discussed in Section 3.4. Thus, in hindsight, it would have been more interesting to measure NFEs at e.g. 1700 nm instead of 1250 nm, since the former wavelength would be closer to the actual resonance in NFE, which we presumably missed by not going above 1550 nm.

In the article, we promised to investigate further the influence of carrier transport on the nanoscale ablation craters by detailed modeling, similar to what was done in [64]. I never got around to do this, because I got busy with the GST project (Chapter 7), and afterwards with the project on transient optical properties of laser-excited dielectrics (Chapter 8). Nevertheless, the intended study does suggest an interesting approach towards examining, and potentially tailoring, hot electron transport phenomena on the nanoscale.

## NEAR-FIELD MARKING IN SU-8

In the previous chapter, we described how quantitative near-field enhancements (NFEs) of plasmonic nanoparticle were obtained by ultrashort laser-pulse ablation in the substrate ( $\text{TiO}_2$ ) below the nanoparticles. The ablation craters were imaged by scanning electron microscopy (SEM), which provided us with two dimensional (2D) contour maps of the NFEs. The experimental results compared favorable well with simulations, although we did see evidence of systematic differences, which we attributed to carrier transport preceding ablation.

In this chapter we use a slightly different approach to near-field marking by making use of *multiphoton polymerization* (MPP) of a photoresist that covers the nanoparticles. Compared to ablation, MPP has a lower threshold fluence, which might mitigate some of the potential side effects of strong excitation, such as hot-carrier transport. However, the biggest advantage of MPP is that three dimensional (3D) surfaces of constant NFEs are can be obtained with atomic force microscopy (AFM). In contrast, debris related to ablation makes this much harder to achieve in the previous approach.

We have recently designed and fabricated a topology optimized (TopOpt) periodic nanostructure, optimized to exhibit maximum NFE at 1500 nm when covered with the photoresist SU-8. I have not yet had the time to carry out the detailed NFE measurements on the new nanostructure, but I expect that a

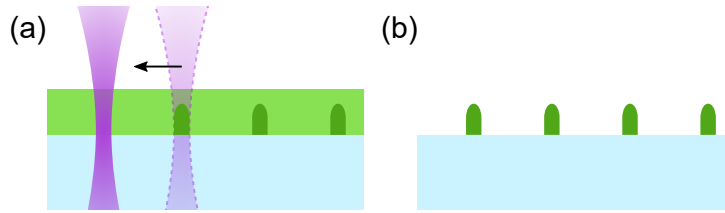


**Figure 6.1:** Photolithography process using a negative resist (green). (a) Exposure step: A focused UV light beam is scanned across the sample (from right to left). The exposure in the focal volume is sufficient to cause polymerization (dark green regions). (b) After development of the resist, only the polymerized parts remain.

manuscript related to this work will be ready by October (discussed in more detail in Section 6.5.1). In this chapter, I present detailed NFE measurements on an older sample with nanoparticles, that, however, were not obtained by TopOpt. This nanoparticle design was thought up by Emil Eriksen, who also did the numerical near-field calculations shown later; Adnan Nazir fabricated the sample.

## 6.1 Introduction

Photolithography is a versatile tool for fabricating 3D structures. In this approach, a photosensitive resist (“photoresist” or simply resist) is coated on top of a substrate and subsequently exposed to light, typically in the UV range, which changes the local chemical composition of the resist. In a *negative* resist, the exposed regions exceeding a certain threshold is *polymerized* (i.e. “hardens”). The remaining underexposed parts of the resist is removed chemically by dipping the resist into a developer solution. In this way, 3D structures can be printed on top of the substrate by selectively exposing parts of the resist with a focused beam of light, see Fig. 6.1.

Positive resists work the other way around: The exposed regions becomes soluble, which are therefore removed in the development step. Thus the desired structures emerge by removing the exposed volumes.

For 3D printing of microstructures, negative resists are typically used. The spatial resolution in this case is limited by diffraction to about the wavelength (typically around 400 nm) of the focused light beam. A simple way to improve the resolution is to use long-wavelength, ultrashort laser pulses, where multi-

photon absorption is needed to locally expose the resist [66–68]. The process is then called multiphoton polymerization (MPP).<sup>1</sup> Impressive large-scale 3D structures with sub- $\mu\text{m}$  features have been written by MPP [69].

Since the condition for MPP, like ablation, exhibits a threshold, it can be used for near-field marking by the same procedure described in Section 5.B.4. Such an approach has been undertaken before [51, 52, 70–72], but the measured NFEs has not been reported in enough detail to allow a thorough comparison to numerical near-field calculations,<sup>2</sup> which is our purpose here.

Before embarking on a description of the experimental procedure and the results, let us briefly describe the polymerization process in more detail. Based on this understanding, we introduce a simple model for the threshold of MPP, which is a function of laser fluence and number of pulses used for the exposure.

## 6.2 Multiphoton polymerization

Negative photoresists used for MPP are typically very viscous liquids (resins), that contains the following three basic ingredients: monomers, oligomers, and (photo)initiators. A monomer is, by definition, a small molecule that can bind to other monomers. An oligomer is a larger molecule that consists of many monomers in a repeating structure [73]. Upon absorption of UV light by the initiator molecules, free radicals are produced that starts a reaction whereby monomers and oligomers bind together, forming a long chain of molecules – a so-called macromolecule. The macromolecule keeps growing until it meets and fuses with another macromolecule, thus forming an even bigger molecule, called a polymer molecule if it is large enough [66]. When a region of the resin consists primarily of such large-scale polymer molecules, the region is said to be polymerized. The initiation process may have to be restarted multiple times in order to create necessary amount of polymers, that can survive the development step. There is, statistically, a minimal optical dose required to complete the polymerization process.

The detailed process leading to polymerization is very complex, as it involves diffusion of and reactions between many molecules. In the simplest

---

<sup>1</sup>Very often the process is simply called two-photon polymerization (TPP) when a Ti:sapphire laser of 800 nm is used for the exposure.

<sup>2</sup>Ref. [51] comes close, but the analysis of the experimental data is somewhat ad hoc: In order to extract NFEs, it is necessary to assume that the NFE drops exponentially away from the nanoparticles.

possible description, we could assume that the polymerization process is completely local (i.e. we neglect spatial effects such as diffusion). Polymerization may then be directly linked to the multiphoton absorption by the initiator molecules. To derive the polymerization threshold, we assert that a certain fraction of initiators have to be activated via multiphoton absorption. Let this fraction be  $A_{\text{th}}$ . Suppose that  $m$  photons is need to be excite, and thus activate, an initiator. The rate of change of the fraction  $A$  of activated initiator can then be modelled as

$$\frac{\partial A}{\partial t} = \sigma_m I^m(t)(1 - A), \quad (6.1)$$

where  $I$  is the intensity of the laser pulse, and  $\sigma_m$  is the  $m$ -photon absorption cross section of the initiators.

Depending on the laser intensity, many subsequent pulses are necessary to activate a large fraction of initiators. When many subsequent pulses are needed, the change in  $A$  per pulse is small, so

$$\Delta A = \int_{\text{pulse}} dt \sigma_m I^m(t)(1 - A) \quad (6.2)$$

$$\approx \sigma_m(1 - A) \int_{\text{pulse}} dt I^m(t) = \eta_m(1 - A)F^m, \quad (6.3)$$

where  $F$  is the fluence and  $\eta_m = 1.064\tau\sigma_m/\sqrt{m}$  for a Gaussian pulse [compare to Eq. (4.6)]. Eq. (6.3) gives the change in  $A$  per pulse. Expecting  $\Delta A$  to be small, and therefore the number of pulses  $N$  to be large in order to cause polymerization, we write

$$\frac{dA}{dN} \approx \Delta A \approx \eta_m(1 - A)F^m. \quad (6.4)$$

We can easily solve this “differential equation” for  $N$ ; the result is

$$A(N) = 1 - e^{-N\eta_m F^m}. \quad (6.5)$$

At the MPP threshold,  $A = A_{\text{th}}$ . The associated threshold fluence depends on the applied number; solving for this threshold,  $F_{\text{th},N}$ , we find

$$F_{\text{th},N} = N^{-1/m} F_{\text{th},1}, \quad (6.6)$$

with  $F_{\text{th},1} = [\ln(1 - A_{\text{th}})\eta_m]^{-1/m}$ , which is the single-pulse MPP threshold. Eq. (6.6) implies that the threshold fluence of MPP decreases with the number

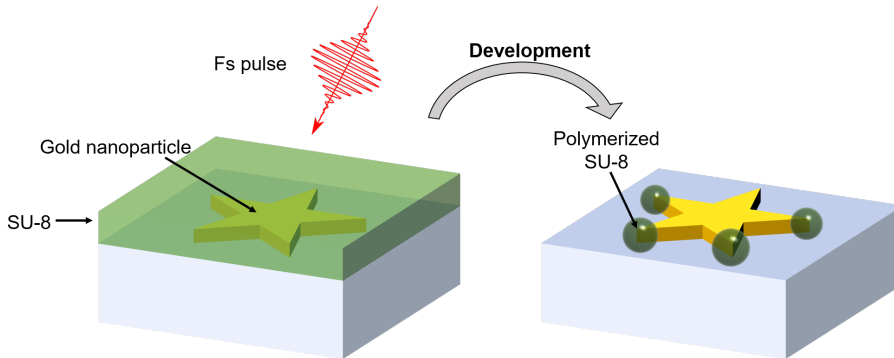


**Figure 6.2:** Principle behind near-field marking by MPP. Displayed here is a small section of a larger sample containing gold nanoparticles (stars in this case). The sample is covered by a negative photoresist (SU-8) and irradiated by ultrashort laser pulses below the MPP threshold. After development, the resist is removed, except for the polymerized parts near nanoparticle where the NFE was sufficient to increase the fluence above the MPP threshold.

of pulses as  $N^{-1/m}$ . A similar scaling of the threshold fluence is also found in the case of ablation, where it is expressed in terms of the *incubation coefficient*  $S$ :  $F_{th,N} = N^{S-1} F_{th,1}$  [74, 75]. Our simple model of MPP predicts that  $S = 1 - 1/m$ .

### 6.3 Experimental approach

The general principle behind near-field marking by MPP is sketched in Fig. 6.2. As a first step, gold nanoparticles are prepared on a flat substrate. The surface is then covered by a negative photoresist (e.g. SU-8, see below), fully embedding the nanoparticles on the substrate. Next, the sample is exposed to ultrashort, near-infrared laser pulses. Considering here a particular nanoparticle, the local laser fluence and number of pulses is adjusted such that the exposure is below, the threshold for MPP. If the NFE by the nanoparticle is sufficient, MPP is caused near the nanoparticle. The final step is development of the resist, where the underexposed (i.e. non-polymerized) parts are removed. The near-field induced MPP around the nanoparticles can then be imaged in AFM and SEM to obtain a surface (in the case of AFM) of a particular value of NFE. If  $N$  laser pulses were used for the exposure, and the (average) laser fluence per

pulse near the nanoparticle was  $F$ , then

$$\text{NFE} = \sqrt{F_{\text{th},N}/F}, \quad (6.7)$$

where  $F_{\text{th},N}$  is the MPP threshold of the resist. Note that this is analogous to how NFEs were obtained by ablation with  $N = 1$  (Section 5.B.4).

### 6.3.1 Experimental details

Metal nanoparticles are produced by EBL on a flat 0.5 mm flat quartz substrate (sometimes covered with a thin  $\sim 300$  nm  $\text{TiO}_2$  film). Before coating the samples with a photoresist, we first clean them with acetone and isopropanol (IPA). Afterwards, the samples are dried on a hotplate. As the final preparatory step, the samples are baked in an oven under low pressure to remove water molecules from the surface, followed by application of an HMDS treatment, which basically makes the sample surface hydrophobic; this greatly promotes adhesion with photoresists used for lithography.

As a negative photoresist, we employ commercial SU-8.<sup>3</sup> SU-8 is very viscous, which is not so great for making thin films. We therefore use a diluted solution of SU-8 (using cyclopentanone as a solvent) that has a much lower viscosity. The samples are covered with the photoresist by spin coating at 6000 rpm, yielding 400–450 nm thick SU-8 films. The coated samples are finally dried on a hotplate at 95 °C for a few minutes.

Exposure is carried out using wavelength-tunable femtosecond laser pulses, derived from an optical parametric amplifier (TOPAS). The steps are the same as described in Section 5.B.4. Briefly, regions on the sample containing no nanoparticles are exposed at different pulse energies and different number of pulses to determine the MPP threshold of SU-8. Next, areas containing nanoparticles are exposed. The irradiation parameters are typically chosen such that the central, most intense, part of the laser-irradiated spot on the sample exceeds the MPP threshold. The tail areas of the Gaussian fluence profile are still below the MPP threshold, which is where polymerization due to NFE is observed. Note, however, that the MPP threshold is actually only known after development of the sample, so prior knowledge about typical MPP threshold values is useful.

The samples are developed immediately after exposure, where they are first baked on a hotplate at 95 °C for a few minutes. The unpolymerized parts

<sup>3</sup>MicroChem, SU-8 3000: <http://microchem.com/Prod-SU83000.htm>.

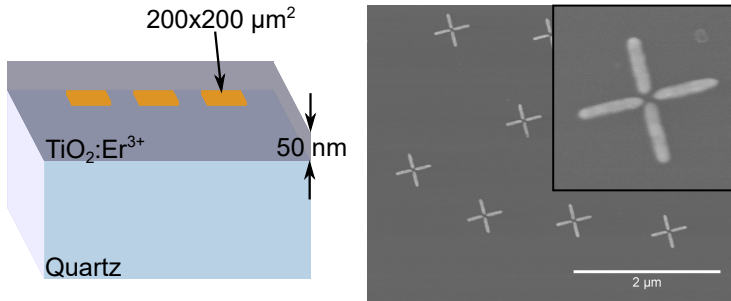


**Figure 6.3:** *Left.* Sample geometry (not to scale), before coating with SU-8. Nanoparticles are printed in small  $200\ \mu\text{m} \times 200\ \mu\text{m}$  areas (colored yellow). The drawing is not to scale. *Right.* SEM image of the randomly distributed nanoparticle crosses. The inset shows a magnified view of one nanoparticle. The length and width of each leg is  $200\ \text{nm}$  and  $50\ \text{nm}$ , respectively. The gap in the center is about  $40\ \text{nm}$  wide, and the height is  $50\ \text{nm}$ .

of the resist are then removed by dipping and actively stirring the samples in a commercial developer solution for a few minutes. Finally, the samples are rinsed in IPA, and are thus ready for characterization by e.g. SEM and AFM.

## 6.4 Results and discussion

The sample and nanoparticle geometry considered in this section is sketched in Fig. 6.3. The nanoparticles (“nanocrosses”) are arranged in a random pattern with an average particle density of  $0.3\ \mu\text{m}^{-2}$ . The nanocrosses were designed to have large NFEs in the  $\text{TiO}_2:\text{Er}^{3+}$  film at  $\sim 1500\ \text{nm}$  for enhanced upconversion yield (UCY) of  $\text{Er}^{3+}$ .

The localized surface plasmon resonances (LSPRs) of the nanoparticles are redshifted slightly after coating the sample with  $450\ \text{nm}$  SU-8.<sup>4</sup> This is confirmed in Fig. 6.4, which shows the extinction cross section  $\sigma_{\text{ext}}$  of the nanoparticles, measured before and after SU-8 was applied. The measurements were carried out by the same procedure described in Section 5.B.3. The new

<sup>4</sup>This can be understood, somewhat crudely, from Eq. (3.11) by replacing  $\epsilon_m = 1$  for air with the larger value of SU-8 at the appropriate excitation wavelength. Another intuitive explanation is as follows: the increased refractive index of SU-8 makes the excitation wavelength near the nanoparticles look smaller; the particle thus *appears* bigger, which, as we know, generally redshifts LSPRs.

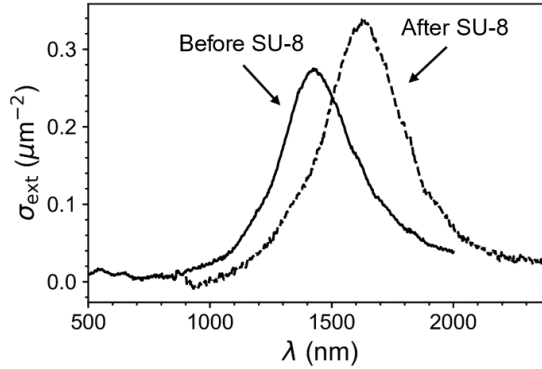


**Figure 6.4:** Measured extinction cross sections of the nanoparticles before (solid line) and after (dashed line) coating the particles with 450 nm SU-8. The LSPR is redshifted from 1400 nm to 1600 nm by SU-8.

LSPR is located around 1600 nm. Realizing that the near-field resonance frequency is slightly redshifted compared to this value (see Section 3.4), we choose 1700 nm as the excitation wavelength.

### 6.4.1 MPP thresholds

We must determine the MPP threshold of the photoresist in order to infer quantitative values of NFEs [see Eq. (6.7)]. This is accomplished by the standard procedure [59], where the size of the polymerized spots are related to pulse energies, assuming a Gaussian beam profile, see Eq. (5.10). Here, we repeat this procedure for a varying number of pulses in order to check Eq. (6.6).

Fig. 6.5 shows the data from which we extract the MPP threshold fluence at 1700 nm. The boundaries of each polymerized spot [e.g. inset in panel (b)] is fitted to an ellipse, which reveals that the spots are roughly circular; the errorbars on the squared diameter of the spots ( $D^2$ ) are estimated from the differences in the minor and major axes of the fitted ellipses. The solid straight lines show fits of Eq. (5.10), but with a single beam radius  $w$ , which in this case is  $w = 8.2 \pm 0.3 \mu\text{m}$ . Each line in panel (a) gives a distinct threshold fluence  $F_{\text{th},N}$  corresponding to the number of applied pulses  $N$  per spot. Assuming a particular value of  $m$ , we use Eq. (6.6) to fit all the data simultaneously to a single line, giving a better estimate of the single-pulse MPP threshold fluence

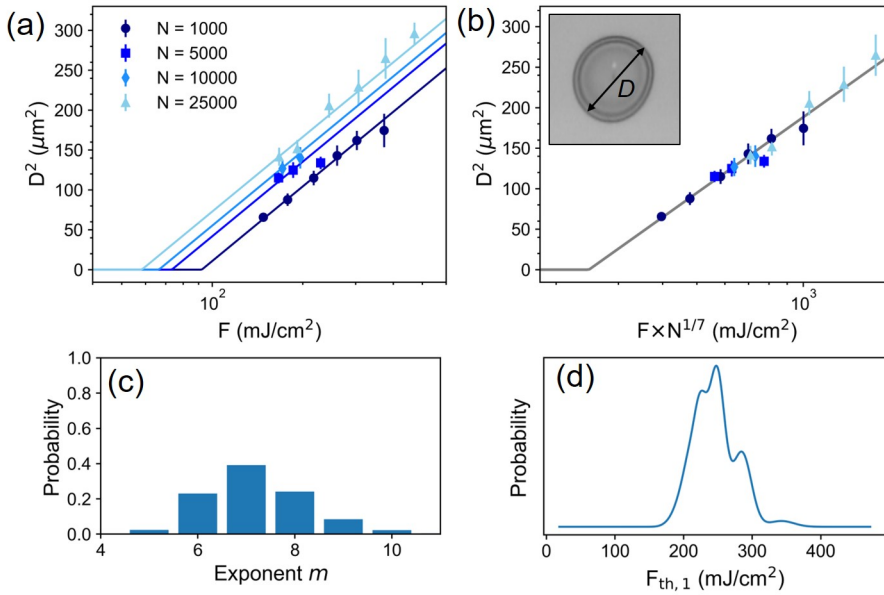


**Figure 6.5:** Determination of the MPP threshold of SU-8 at 1700 nm. (a) Squared diameter of polymerized spots (approximately circular) as a function of fluence  $F$  at different number of pulses  $N$ . The solid lines are fits to Eq. (5.10), which intersects the horizontal axis at  $F_{\text{th},N}$ . (b) Same as (a) except that the fluences are by  $N^{-1/7}$ . The solid line is a fit to a single straight line based on a single threshold, yielding  $F_{\text{th},1}$ . The inset shows an example of a polymerized spot. (c-d) Probability distributions obtained from the fit in (b) of the exponent  $m$  and the threshold fluence  $F_{\text{th},1}$ .

$F_{\text{th},1}$ . This is accomplished in panel (b) with  $m = 7$ , as this value seems to best fit the data. The value is actually surprising; SU-8 starts to absorb around 400 nm, so we would have expected  $m = 5$ .

Panel (c) shows the probability distribution of  $m$  extracted from the data. The probabilities are obtained simply by repeating the fit in panel (b), assuming different values of  $m$ , and comparing how well each model fits the data. The best value is, apparently,  $m = 7$ , although  $m = 6$  and  $m = 8$  fits the data as well. The reason for this uncertainty is the lack of data points. On the same sample, but at 1500 nm, I found  $m = 7$  to clearly be the best fit. In this case,  $m = 4$  would have been expected. It is interesting that the incubation coefficient associated with  $m = 7$ ,  $S \approx 0.86$ , is very close to the values reported for a variety of metals [75]. This could imply that multiphoton absorption is not an

adequate description of the photoinitiation process. Alternatively, our simple model might be too simplified, rendering  $m$  unphysical; for instance, diffusion of monomers and oligomers out of the irradiated spot could increase the MPP threshold fluence by effectively increasing  $m$ . However, there should still be a wavelength dependence of  $m$  if the initiators are excited by multiphoton absorption, but it is possible that 1500 nm and 1700 nm are too close in energy to reveal it in our case.

The inferred single-pulse threshold fluence  $F_{\text{th},1}$  is shown in Fig. 6.5. Since there is some ambiguity concerning the best value of  $m$ , we have averaged the probability distributions of  $F_{\text{th},1}$  obtained at each  $m$  (each distribution is approximately normal). The three spikes in the averaged distribution originate from  $m = 5, 6,$  and  $7$ . This gives a conservative estimate of  $F_{\text{th},1} = 250 \pm 33 \text{ mJ cm}^{-2}$ .<sup>5</sup>

#### 6.4.2 Near-field enhancements

A particular laser-irradiated spot containing nanoparticles is shown in Fig. 6.6. The peak fluence was  $F_0 = 170 \text{ mJ cm}^{-2} \approx 2.5F_{\text{th},N}$ , and  $N = 10\,000$  number pulses were used. Moving outside the polymerized boundary reveals that these nanoparticles have indeed caused MPP by NFE (see the lower-right inset). Furthermore, SU-8 appears to stick to the particle in the direction along the electric field polarization. This is particularly pleasing, because it is only when the electrons in the metals are driven along the long the legs that resonant NFE at this wavelength is expected.

A 2D map of experimental NFEs, derived from SEM images, and compared to numerical calculations, is shown in Fig. 6.7. To obtain the experimental contours, we used the same method of averaging several SEM images of nanoparticles, irradiated with approximately the same fluence, as explained in Section 5.B.4. The color scale displays NFE, and is the same in each panel. Experimental contours of small values of NFEs are lacking because nanoparticles close to the polymerized spot were severely modified by the exposure. Nevertheless, we find a decent agreement between the observed and simulated values, where the NFE is strongly localized near the tips, directed along the electric-field polarization. The experimental contours in the gap are somewhat different than the simulated values, which suggests that the associated surfaces

<sup>5</sup>When a probability distributions is not normal, as assumed in least-squares methods, I use instead a slight generalization of the standard error  $\sigma$ :  $\sigma = (C_{84} - C_{16})/2$ , where  $C_X$  is  $X$ th percentile.

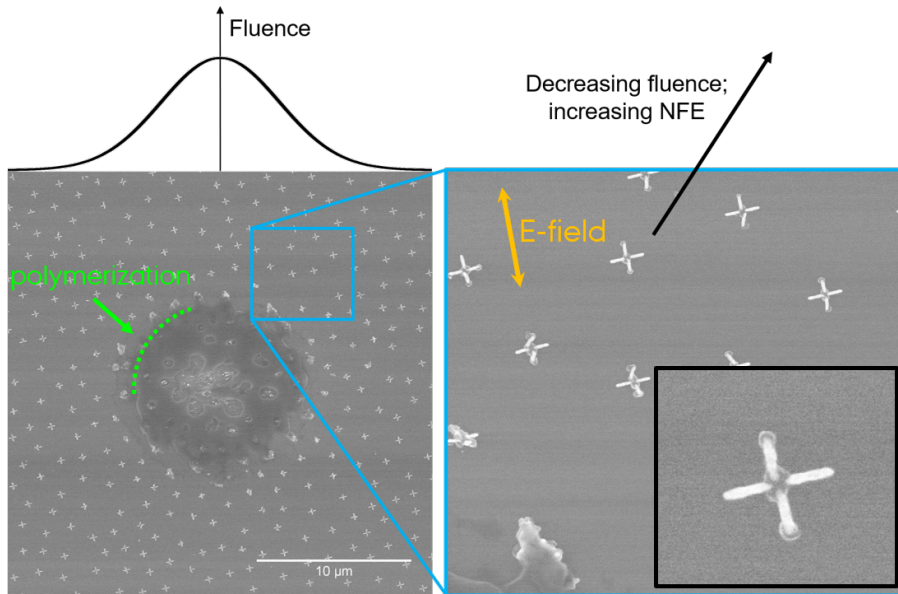
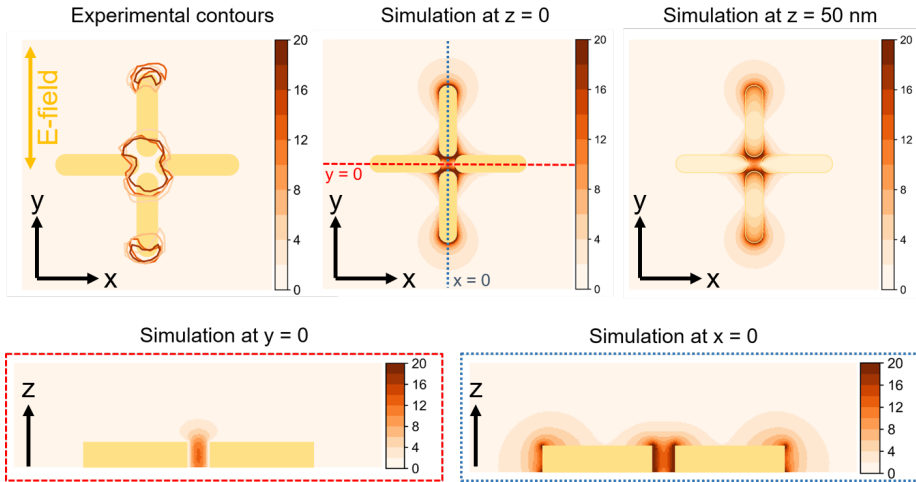


**Figure 6.6:** SEM image of a polymerized spot (peak fluence  $F_0 = 170 \text{ mJ cm}^{-2}$ ,  $N = 10\,000$  pulses), where the boundary is indicated by the green dashed line. The fluence profile of the laser beam is Gaussian and sketched on the top. The blue square shows an enlarged view of a region just outside the polymerized spot, where the local fluence is below the MPP threshold. Nanoparticles closest to the polymerized area were modified, probably partially melted, by the exposure. The yellow arrow shows the direction of the electric-field polarization of the laser pulses. A magnified image of a nanoparticle is shown in the inset in the lower-right corner. A bit of polymerized SU-8 remain attached to the particles where NFE is expected.

of constant NFEs extend above the full height of the nanoparticles. This is confirmed in the two lower panels, showing the simulated NFE in the  $y = 0$  and  $x = 0$  planes.

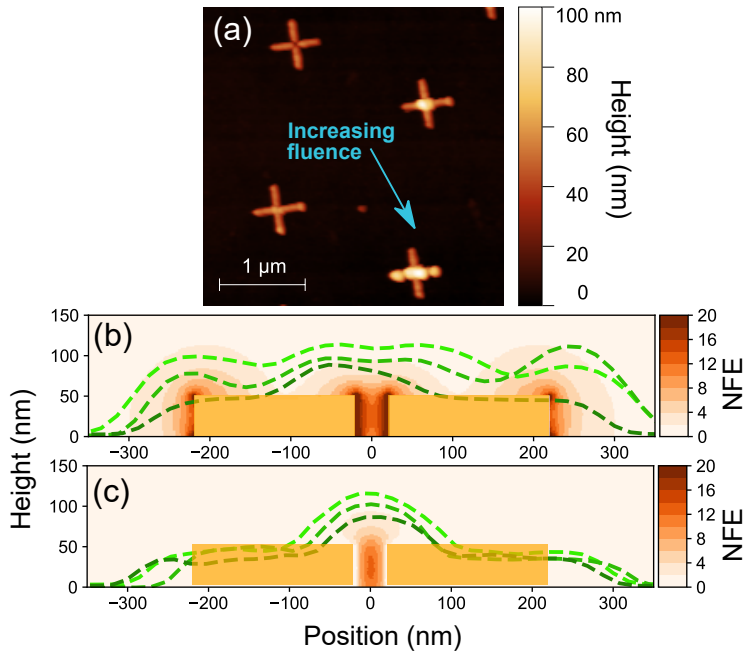
To check the heights of the polymerized structures, we employ AFM. Obtaining good images with AFM is more challenging than SEM, because of the possibility of various tip artefacts. One inherent artefact is tip broadened, which, assuming perfect AFM tips and imaging conditions, is expected to broaden the typical features of the nanoparticles by  $\sim 20 \text{ nm}$ . One could correct for this by carefully calibrating the tips, but this has not been done.

Fig. 6.8, panel (a), shows an AFM image recorded (in tapping mode)



**Figure 6.7:** Experimental (upper left) and simulated electric near-field maps at 1700 nm. The color scale represents NFE; it is truncated at 20, corresponding to the largest measured value. The nanoparticle geometry, as used in the simulations, is highlighted by yellow. Each leg is 200 nm long (tip to tip).

outside the same polymerized spot in Fig. 6.6. Polymerized SU-8 is clearly seen to accumulate on top of the nanoparticles, as evident by the increased height. The particle in the upper left corner, however, shows no sign of polymerization induced by NFE. In general, AFM appears to be a more sensitive probe of polymerized SU-8, but because of the extra dimension (height), AFM images show a lot more variation in the near-field patterns than apparent in SEM. However, there is also an element of randomness to the near-field patterns, as panel (a) of Fig. 6.8 clearly shows: The arrow in this figure indicates, roughly, the direction of increasing fluence, which is not totally consistent with the observed near fields. The discrepancies may be caused by three effects: (i) variations in the laser-beam profile, (ii) geometric variations in the nanoparticles, and (iii) randomness in the polymerization process. The variations observed here are presumably a combination of all three possibilities; is it, nonetheless, possible to distinguish them? Better control over the laser beam profile will obviously help. Item (ii) is difficult, because we are pushing the limits of our EBL process. As an alternative, one could print periodic nanostructures, because it has been observed, in the case of microspheres, that near-field patterns of periodic structures are incredibly robust in terms of



**Figure 6.8:** AFM images, providing contours of constant NFE around nanoparticles. (a) Image taken outside the same polymerized spot displayed in Fig. 6.6. The color scale shows the measured height above substrate. The direction to the center of the spot is indicated by the blue arrow. (b-c) Simulated NFEs in the  $y = 0$  (b) and  $x = 0$  (c) planes defined in Fig. 6.7. The green dashed lines show the AFM profiles obtained from three different nanoparticles. The associated experimental NFEs are ordered from low (bright) to high (dark).

defects in the particle patterns [11]. The cause of the robustness is that the near fields are now produced collectively by all the neighboring nanoparticles. By extension, this implies that the periodic structures are also robust with respect to local variations of the laser beam. If it turns the same kind of randomness in Fig. 6.8, panel (a), is observed also for periodic structures, I think it is safe to conclude that the randomness is caused by the polymerization process.

The randomness in the surfaces of constant NFE can of course be mitigated by averaging over several nanoparticles as we do in SEM. This is, however, a highly nontrivial task, because of the extra dimension (height) in AFM.

Putting aside these complications, we show in panels (b-c) experimental contours of NFE by green dashed lines obtained from three distinct nanopar-

ticles. The associated NFEs are ordered from low (bright green) to high (dark green) values. Panel (b) shows the AFM profiles along the electric-field polarization (compare to Fig. 6.7). The profiles in panel (c) are perpendicular to the ones in panel (b). We find a qualitative resemblance with the simulations; the experimental features are generally much broader, but that is to be expected. While the SEM measurements gave a fair quantitative agreement, this is not the case here, presumably due to large variations in the AFM patterns, as mentioned above.

## 6.5 Conclusion and outlook

We have investigated the electric near fields of a gold nanoparticles, shaped as crosses, experimentally and theoretically. By covering the particles with a negative photoresist (SU-8), and subsequently irradiating them with near-infrared ultrashort laser pulses below the polymerization threshold, we could selectively polymerize the resist around the nanoparticles through NFE. The boundary of such polymerized structures represents surfaces of constant NFE. Experimental NFEs were obtained by careful determination of the polymerization threshold and control of the exposure conditions. We found a good, quantitative agreement between simulations and 2D maps of experimental NFEs, obtained by imaging with SEM. We used AFM to image the heights of the polymerized structures as well, which revealed a lot more randomness in the near-field patterns than was apparent with SEM. We discussed a couple of reasons for the apparent randomness. With AFM we could get a qualitative comparison with the simulations, but the spatial resolution was limited by e.g. tip broadening.

### 6.5.1 Outlook

The simple model for the MPP threshold (see Section 6.2), assumes that  $m$  photons is needed to start the polymerization in SU-8;  $m$  is easily determined experimentally as described in Section 6.4.1, where we found  $m \approx 7$  at 1500 nm and 1700 nm. This was surprising, since  $m = 4$  or 5 would have been expected. If multiphoton absorption truly starts the polymerization process in SU-8, then clearly  $m$  must be wavelength dependent. We can check this by measuring  $m$  across a wide range of excitation wavelengths, e.g. 400 nm (second harmonic of Ti:Sapphire), 800 nm, and above 2000 nm. It could prove interesting if  $m \approx 7$  is consistently found; clearly, then, MPP would be misnomer?

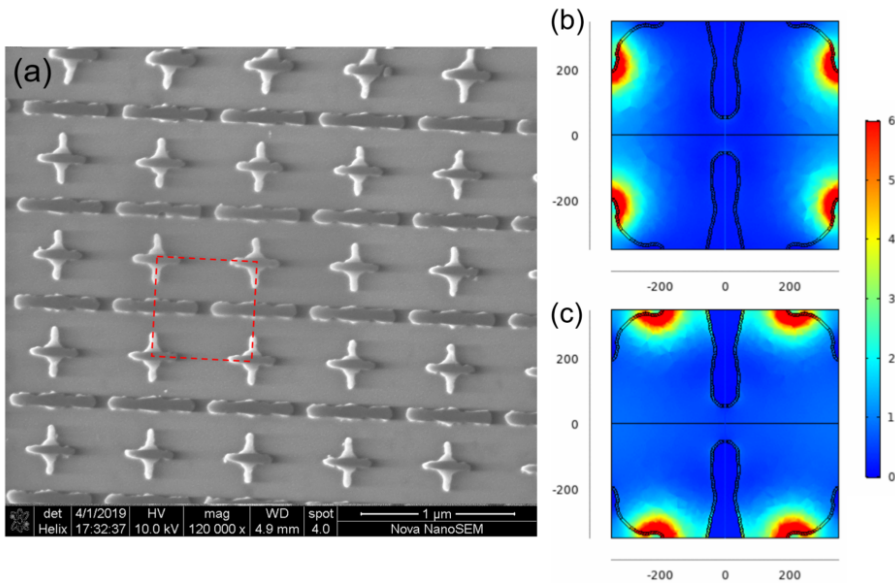


**Figure 6.9:** Periodic nanostructure found by TopOpt. (a) SEM image of the design produced by EBL. The red-dashed rectangle highlights a unit cell of the structure. (b-c) Calculated near fields in a unit cell at 1500 nm excitation near the substrate surface. The color scale represents NFE, which is truncated at 6. The calculations includes  $\sim 450$  nm SU-8 film that is needed for the near-field marking procedure.

We discussed some of the reasons for the apparent randomness of the polymerized structures. I believe the easiest way forward is to simply repeat the measurements on a periodic nanostructure, as this is robust with respect to spatial fluctuations in the laser-beam profile and geometric variations in the fabricated structures. If randomness persists, the cause is most likely the polymerization process. This option would, however, be difficult to circumvent.

As mentioned in the introduction, we have recently fabricated gold nanostructures based on designs derived from TopOpt. An SEM image of the design is shown in panel (a) in Fig. 6.9. Simulations of the NFE at 1500 nm excitation, is shown in panels (b-c) for two different polarizations. The nanostructure was optimized for achieving a large, average enhancement in the SU-8 film. The next step for me will be to carry out these measurements in detail for different excitation wavelengths, and for different polarizations. I expect

that we will have a manuscript ready for submission some time in October 2019. Major emphasis will be put on TopOpt as a technique for finding good designs; and of course, the detailed validation thereof by near-field marking by MPP.

## LASER MODIFICATIONS OF $\text{Ge}_2\text{Sb}_2\text{Te}_5$ THIN FILMS

In this chapter, we examine amorphization and ablation of  $\text{Ge}_2\text{Sb}_2\text{Te}_5$  (GST) thin films, induced by ultrashort laser pulses. The investigations are published in [2] and reproduced below. One of the key findings is that a particular thermal condition has to be fulfilled in order to promote amorphization of GST: Complete melting of the film. The condition turns out to be violated close to metal nanoparticles, where heating by the laser pulse is strongly localized around the particles. In the final section of this chapter we discuss how this understanding resolves the issues related to GST and near-field marking, touched upon previously in Section 1.4.

### 7.1 Background

GST is a so-called phase-change material (PCM), which means that the crystal structure can be switched between two phases – one crystalline, one amorphous – by heating the material with a short electrical or optical pulse. The two phases have very different electrical and optical properties, which makes GST (and other related PCMs) well-suited for the next generation of memory

devices [76]. However, GST is not just an item of the future; it is actually one of the common PCMs used in rewritable DVDs.

As we have described previously, we originally intended to utilize amorphization of GST as a tool for near-field marking [10, 11]. When this failed to work (see Section 7.3 below), we proceeded with systematic studies of ablation and amorphization in various GST films and under different irradiation conditions. In particular, we observed an interesting trend where the threshold for amorphization drastically increased with increasing film thickness. The typical understanding of the process is that the material must first melt, and then rapidly cool in order to be trapped in the metastable amorphous state [77–79]. We argued that, in addition, complete melting of the GST films is required to promote amorphization. This claim was supported by thermal simulations and detailed electron microscopy imaging.

An unrelated surprise of our investigations was the emergence of an additional ablation threshold in thick GST films. A low-fluence threshold was seen on all films, which we attributed to photomechanical spallation through detailed cross-section transmission electron microscopy (TEM) imaging, which revealed frozen-in voids, providing a clear indication of spallation. The high-fluence threshold still remains somewhat of a mystery, but one possibility is discussed.

## 7.2 Contributions

I wrote most parts of the paper, produced all the figures, and carried out the experiments and the simulations. Peter L. Tønning contributed to early work on GST. Emil H. Eriksen provided valuable feedback on details on the numerical calculations, where some of his code is used. Pia B. Jensen did all the focused-ion beam milling, and Jacques Chevallier helped me record all the TEM images.

The publication [2] is included in the following with minor changes to the layout and labeling of sections, equations, and references.

## Femtosecond-laser-induced modifications of $\text{Ge}_2\text{Sb}_2\text{Te}_5$ thin films: permanent optical change without amorphization

Søren H. Møller<sup>1</sup>, Emil H. Eriksen<sup>1</sup>, Peter L. Tønning<sup>1,2</sup>, Pia B. Jensen<sup>1</sup>, Jacques Chevallier<sup>1</sup>, and Peter Balling<sup>1,3</sup>

<sup>1</sup> Department of Physics and Astronomy, Aarhus University, Ny Munkegade 120, DK-8000 Aarhus C, Denmark

<sup>2</sup> Department of Engineering, Aarhus University, Finlandsgade 22, DK-8200 Aarhus N, Denmark

<sup>3</sup> Interdisciplinary Nanoscience Center, Aarhus University, Gustav Wieds Vej 14, DK-8000 Aarhus C, Denmark

**Abstract:** Modifications induced by ultrashort laser pulses have been investigated in crystalline  $\text{Ge}_2\text{Sb}_2\text{Te}_5$  thin films. The observations comprise optical and structural changes, amorphization, and ablation. By combining optical microscopy and cross-sectional scanning- and transmission electron microscopy, it is found that the threshold for permanent change of the optical properties of  $\text{Ge}_2\text{Sb}_2\text{Te}_5$  – responsible for the reduced optical reflectivity – is slightly lower than that for amorphization; no further change in reflectivity is seen upon amorphization. The laser-fluence thresholds for amorphization and change of the optical properties both show a strong dependence on film thickness that can be explained thermally by two-temperature simulations. In the case of sufficiently thick films, two distinct low- and high-fluence ablation thresholds are found. The mechanisms of the ablation thresholds are discussed, and it is concluded that ablation in the low-fluence regime proceeds by photomechanical spallation.

## 7.A Introduction

Phase-change materials (PCMs) are known for their rapid, reversible and non-volatile switching between crystalline and amorphous phases that have profoundly different electro-optical properties. One of the most well-studied PCMs is  $\text{Ge}_2\text{Sb}_2\text{Te}_5$  (GST) due to its very fast phase-switching speed.

Phase switching in GST and related PCMs was initially achieved by irradiation with ns and ps lasers, and the mechanism could be understood in terms of melting, quenching and resolidification [77–79]. More recently, time-resolved studies on the amorphization mechanism in GeTe alloys by ultrafast laser excitation have revealed that the large change in optical properties happens already on the fs time scale [80–83]. This is much faster than any thermally-induced transition. The most popular explanation of these observations is based on breaking of so-called “resonant bonds” [84] that could be responsible for the

large dielectric constant of crystalline PCMs as compared to their amorphous counterparts [85, 86]. It is generally believed that amorphization is either necessary for preventing subsequent healing of the resonant bonds [82], or that amorphization could be triggered by a rattling motion of Ge atoms on longer time scales [83]. It should be noted that not all reports support the idea of resonant bonds as the chief phase-change mechanism [87, 88]. Further research is needed to clarify this important question.

In this work, we study the thresholds for permanent change in the optical properties as well as for structural phase change (crystalline to amorphous) and ablation of crystalline GST films by single-pulse irradiation with a femtosecond laser. The dependence of the thresholds on the film thickness is examined and discussed in detail in relation to two-temperature model (TTM) simulations. Optical and scanning- and transmission electron microscopy (SEM/TEM) studies reveal that permanent change in the optical properties of GST (henceforth denoted as optical change) can be achieved while the film remains crystalline after excitation; amorphization occurs only at slightly higher fluences, but with no additional change in the optical contrast. This is at variance with the general belief that amorphization is either necessary for, or a consequence of, permanent reflectivity change. Our results may help in providing more insight into the phase-change mechanism, and may in addition be of practical importance for the design of photonic devices based on PCMs.

## 7.B Experimental details

$\text{Ge}_2\text{Sb}_2\text{Te}_5$  (GST) films were deposited on top of silicon(100) substrates in a radio-frequency magnetron sputtering system at room temperature using a commercial GST target. All samples were subsequently annealed for 15 minutes in a nitrogen atmosphere at 200 °C to produce a nanocrystalline fcc phase of GST [89]. The crystal phase was confirmed by X-ray diffraction (XRD), and the stoichiometry was checked by Rutherford backscattering spectrometry (RBS). The optical constants at near-infrared wavelengths (800 to 2500 nm) were determined by ellipsometry from several samples using a combined Tauc-Lorentz and Brendel oscillator model, and agree well with the values reported in the literature [90]. As GST is known to oxidize [91], a 2-3 nm oxide layer on top of GST, consisting of  $\text{TeO}_2$  (refractive index taken from [92]), was introduced in the optical model, offering a slightly improved agreement with the ellipsometry data.

In the laser-irradiation experiments, an optical parametric amplifier (TOPAS) was used to generate femtosecond pulses with tunable, central wavelength (1160 nm to 2600 nm) from part of the output of a 35 fs Ti:sapphire laser. Only the results for 1500 nm (60 nm FWHM) irradiation are reported in this work. The reason for choosing this particular wavelength is firstly due to its importance in telecommunication where PCMs may play a role in future applications. Secondly, the optical absorption depth at 1500 nm excitation is about 80 nm, which makes it easier to study the influence of thin-film interference effects as compared to e.g. 800 nm excitation, where the absorption depth is only 16 nm. Thicker GST films can therefore be studied in the former case, which makes the structural characterizations easier. The duration of the 1500 nm pulses has been measured by cross-correlation to be about 50 fs. The samples were positioned on a computerized 3-axis stage and irradiated at normal incidence by single pulses. Pulses from the TOPAS were focused down to a Gaussian spot (around 10  $\mu\text{m}$  at  $1/e^2$ ) on the sample surface, and remain of Gaussian shape until a distance approximately 15  $\mu\text{m}$  from the center of the spot. A calibrated photodiode was used to record the pulse energy, which was adjusted by passing the beam through different absorptive optical density filters.

Threshold fluences for ablation and optical change of the GST films were determined by plotting the diameter squared of the ablated and/or optical-changed spots against the logarithm of the associated peak laser fluences [59]. In the case where two or more thresholds are present simultaneously (i.e. two distinct ablation craters and an optical-changed ring as will be presented later), the data were fitted with a common laser beam spot size. This is explained in more detail in 7.G.1.

Atomic force microscopy (AFM), SEM, and TEM were used to characterize the laser-irradiated spots in GST. Lamellas (less than 100 nm thick with lengths up to 1  $\mu\text{m}$ ) for TEM were prepared by focused-ion-beam milling with  $\text{Ga}^+$  ions. Prior to milling, a protective gold layer of 100 nm was added onto the GST samples by thermal evaporation in addition to a protective carbon layer, which is usually added at the beginning of the milling process. The addition of a gold layer was found to be necessary to prevent the  $\text{Ga}^+$  ions from penetrating the carbon layer and amorphizing the upper part of the GST film. From cross-sectional TEM, it is possible to assess the crystallinity of the film in great detail, yet the same information was qualitatively also evident by cross-sectional SEM.

## 7.C Modelling

To inspect the effects of the laser irradiation, it is necessary to know how energy is distributed in the system. During laser-irradiation, electrons in the valence band of GST are excited to the conduction band where they thermalize on the fs time scale. Later, on the ps time scale, the heat of the conduction-band electrons (and valence-band holes) is gradually transferred to the lattice via electron-phonon scattering. Meanwhile, the heat is distributed by diffusion inside the system. The lattice heating typically induces the macroscopic response, resulting in e.g. ablation and amorphization.

A model that adequately captures these thermal effects is the so-called two-temperature model (TTM) [93, 94]. The model is usually applied to metals. For semiconductors, an extended TTM has been developed [65, 95], which should be more appropriate for GST. However, the characteristic time scale for carrier transport in GST turns out to be similar to that of carrier thermal diffusion (see 7.G.2). Both types of diffusion will therefore have roughly the same spatial dependence. In that case it is reasonable to treat only the thermal transport by using the standard TTM used for metals with similar temperature-dependent carrier properties.

Since the laser spot is large ( $\sim 10 \mu\text{m}$ ) compared to the characteristic absorption depth (10 to 100 nm), heat diffusion is dominant in the direction perpendicular the surface of the GST film. In this one-dimensional approximation, the TTM couples the energy density of the electrons,  $H_e$ , to that of the lattice (phonons),  $H_{\text{ph}}$ , via the equations:

$$\frac{\partial H_e}{\partial t} = \frac{\partial}{\partial x} \left( \kappa_e \frac{\partial T_e}{\partial x} \right) - g(T_e - T_{\text{ph}}) + S(x, t), \quad (7.1)$$

$$\frac{\partial H_{\text{ph}}}{\partial t} = \frac{\partial}{\partial x} \left( \kappa_{\text{ph}} \frac{\partial T_{\text{ph}}}{\partial x} \right) + g(T_e - T_{\text{ph}}). \quad (7.2)$$

Here,  $\kappa$  is the thermal conductivity,  $T$  is the temperature, and  $g$  is the coupling factor between the electronic and lattice systems. The first terms on the right-hand side of Eqs. (7.1) and (7.2) account for heat diffusion. The final term in Eq. (7.1),  $S(x, t)$ , is the source term, transferring energy from the laser pulse to the electrons and holes.

To treat the effects of melting in GST, the lattice volume-specific heat capacity,  $C_{\text{ph}}$ , is made sufficiently large during the phase transition to ensure a near-constant temperature of  $T_m$  until an amount of heat, corresponding

**Table 7.1:** Thermal properties of fcc-GST and silicon. Uncited values were estimated by the authors, see 7.G.2 for details.

Quantity	Ge <sub>2</sub> Sb <sub>2</sub> Te <sub>5</sub>	Si	Unit
$\kappa_{\text{ph}}$	0.45 <sup>a</sup>	130	W m <sup>-1</sup> K <sup>-1</sup>
$\kappa_{\text{e},0}$	$4.0 \times 10^{-2}$		W m <sup>-1</sup> K <sup>-1</sup>
$C_{\text{ph}}$	$1.38 \times 10^6$ <sup>b</sup>	$1.63 \times 10^6$	J m <sup>-3</sup> K <sup>-1</sup>
$\gamma$	20.0		J m <sup>-3</sup> K <sup>-2</sup>
$T_{\text{m}}$	618 <sup>c</sup>		°C
$L_{\text{m}}$	$7.0 \times 10^8$ <sup>c</sup>		J m <sup>-3</sup>
$R$	$1.0 \times 10^{-8}$		m <sup>2</sup> K W <sup>-1</sup>
$\tau_{\text{e-ph}}$	$2.2 \times 10^{-12}$ <sup>d</sup>		s

<sup>a</sup>[96], <sup>b</sup>[97], <sup>c</sup>[98], <sup>d</sup>[82].

to the heat of fusion,  $L_{\text{m}}$ , has been absorbed. Furthermore, heat diffusion into the silicon substrate is accounted for via the thermal boundary resistance, henceforth denoted as  $R$ , a parameter that is very important in the range of film thicknesses considered here where significant heating of the entire GST occurs. The choice of material parameters and the implementation details are discussed in detail in 7.G.2; the values are summarized in table 7.1.

### 7.C.1 The source term

In thin films, it is important to correctly treat absorption by solving the electromagnetic wave equations. The usual Lambert-Beer law for absorption, described by  $e^{-\alpha x}$ , breaks down, and the intensity (i.e. time-averaged poynting vector) is not proportional to the square of the electric field due to the presence of forward- and backward-going waves in the film [99]. Once the correct fields have been found, absorption in a linear medium is given by  $A(x) = \varepsilon_0 \int d\omega \text{Im}\{\omega \varepsilon_r(\omega)\} |\mathbf{E}(x, \omega)|^2$ , where  $\varepsilon_r$  is the (complex) relative permittivity,  $\omega$  is the angular frequency, and  $\mathbf{E}$  is the electric field expressed in frequency domain [13].

GST is highly absorptive at the considered wavelengths, and is therefore treated as a linear medium in our simulations. While the spectral profile of the laser pulses are Gaussian with a FWHM of 60 nm, centered at 1500 nm, the absorption is well-approximated by considering only the central wavelength

because  $\text{Im } \varepsilon_r$  changes little in the relevant spectral range.

Since the time scale of the laser pulse is short compared to the thermal timescales, the source term may be treated as a delta function in time. Thus, after the laser-pulse excitation at time  $t = 0$ , the energy distribution is:

$$H_{\text{ph}}(x, t = 0) = H_{\text{ph},0}, \quad H_e(x, t = 0) = H_{e,0} + A(x). \quad (7.3)$$

Here,  $H_{\text{ph},0}$  and  $H_{e,0}$  are the (unimportant) offsets in the energy densities at room temperature (i.e. before excitation);  $A(x)$  is the absorption profile, now calculated simply as  $A(x) = \varepsilon_0 \text{Im}\{\omega_0 \varepsilon_r(\omega_0)\} \int d\omega |\mathbf{E}(x, \omega)|^2$  with  $\omega_0 = 1.26 \times 10^{15} \text{ s}^{-1}$  (corresponding to 1500 nm). Note that the integral of  $|\mathbf{E}(x, \omega)|^2$  is directly proportional to the laser fluence  $F$ . The electromagnetic fields are calculated using the transfer-matrix method (TMM) (assuming an infinitely thick Si substrate to disregard backreflections) [15] using the *tmmpy* package [100].

## 7.D Results

In the following we present the thickness dependence of experimental modification thresholds in GST together with their structural characterizations. Film thicknesses in this study range from 20 nm to 250 nm. It will be useful to consider the dimensionless quantity  $\eta = \alpha d$ , which is the ratio of the film thickness ( $d$ ) to the optical absorption length ( $\alpha^{-1}$ ). The latter is close to 80 nm in the GST films at 1500 nm wavelength. Films less than 80 nm ( $\eta < 1$ ) are consequently considered “thin”, while the rest ( $\eta > 1$ ) are considered “thick”.

### 7.D.1 Modification thresholds

Fig. 7.1 shows a few selected laser-irradiated spots on a subset of the samples with different film thicknesses (each column corresponds to one particular and distinct sample). Each row shows a new spot produced at a different peak fluence, noted in the upper left corner. The images were recorded in a reflection white-light microscope (the illumination source is a halogen light bulb) on an 8-bit CCD using a 0.80 N.A. objective. The images displayed here are as-recorded, i.e. not normalized, and without any post-processing. Three threshold modifications are apparent: an optical change with reduced reflectivity (boundaries indicated by the green lines), ablation at low fluence

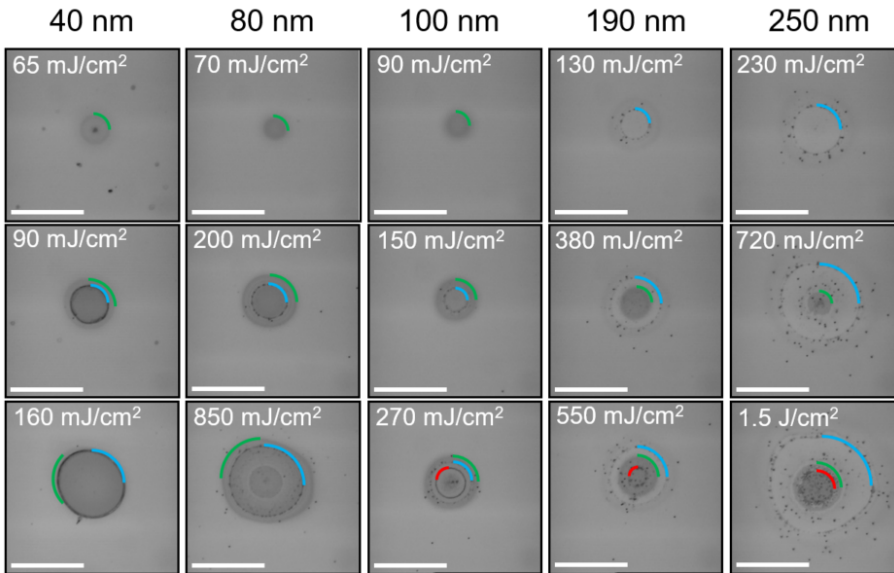


**Figure 7.1:** Gray-scale white-light images of laser-irradiated spots in GST. Each column corresponds to a specific GST sample thickness as noted above. The peak laser fluence is noted in each image. Boundaries of laser-induced modifications are indicated by the solid lines. Green: optical change; blue: first ablation; red: second ablation. The scale bars are 20  $\mu\text{m}$ .

(blue lines), and ablation at higher fluence (red lines). We will refer to the two distinct ablation craters as first and second ablation, where first ablation refers to the crater with the lowest threshold fluence. In the thin-film regime ( $\eta < 1$ ), GST is completely removed by first ablation, exposing the silicon substrate underneath. (Silicon is seen as the darkest areas in the first two columns (40 nm and 80 nm) of Fig. 7.1 due to its comparatively lower reflectivity than optical-changed GST.) The complete removal of films was also confirmed by AFM. Second ablation is consequently only present on the thick ( $\eta > 1$ ) samples. Note that the bright annular region present in the 80 nm film irradiated at 850 mJ cm<sup>-2</sup> is due to amorphization of silicon [101, 102].

As a general trend we note that the reflectivity has increased slightly within the first ablation crater (this is especially apparent in the two rightmost columns of Fig. 7.1). This could be due to the removal of a partially oxidized upper GST layer [91] as no capping layer was used in this work. Removal of

this oxide layer (2-3 nm  $\text{TeO}_2$ ) amounts to changes in the reflectivity of a few percentage points in the visible spectrum (according to TMM calculations), and is consistent with the slight changes observed here.

The modification thresholds were obtained as explained in section 7.B; they are plotted against the film thickness in Fig. 7.2(a). First ablation initially increases with film thickness, but reaches a constant value in the thick-film regime. Conversely, optical change and second ablation continue to increase with film thickness. The optical-change threshold in fact exceeds that of first ablation when the films are thicker than 150 nm. Panel (b) shows a closer look at the optical-change thresholds in the thin-film regime. The dash-dotted and solid lines are estimations of the optical-change threshold from TMM and combined TMM/TTM calculations; they will be discussed in section 7.E. The black dashed line in panel (b) is a representative prediction of the optical-change thresholds based on the Lambert-Beer law for absorption. Panel (c) shows the crater depths of first and second ablation in the thick-film regime, obtained by AFM. 40 nm to 50 nm is removed by the first ablation. For second ablation, a correlation appears to exist between ablation depth and film thickness where approximately half the film is removed.

## 7.D.2 Structural characterization

The ablated and optical-changed regions were investigated in more detail by cross-sectional SEM and TEM. For the TEM imaging, lamellas were prepared as explained in section 7.B. The TEM images were recorded at 200 keV. Cross-sectional SEM images of the laser-irradiated spots were obtained after breaking the samples along a line intersecting a series of the spots.

Fig. 7.3 shows optical and SEM images of the same laser-irradiated spot on a 190 nm GST film that has been cleaved in half. Panel (a) shows a white-light image on which three colored boxes have been drawn. The blue and green boxes contain the boundaries of first ablation and optical change, respectively. Panel (b) depicts a tilted SEM image of the same region containing both the first ablation and optical-change boundaries. Cross-sectional images of the blue and green regions at increased magnification are shown in panels (d) and (e), respectively. In panel (d), it is seen that part of the film has been removed due to ablation. The nanoscale grains of GST are clearly visible, especially near the silicon substrate (the top part of panel (d)). Note that columnar grains are starting to appear near the free GST surface (bottom part) in panel (d). The columnar grains grow in length with increasing incident fluence, and in

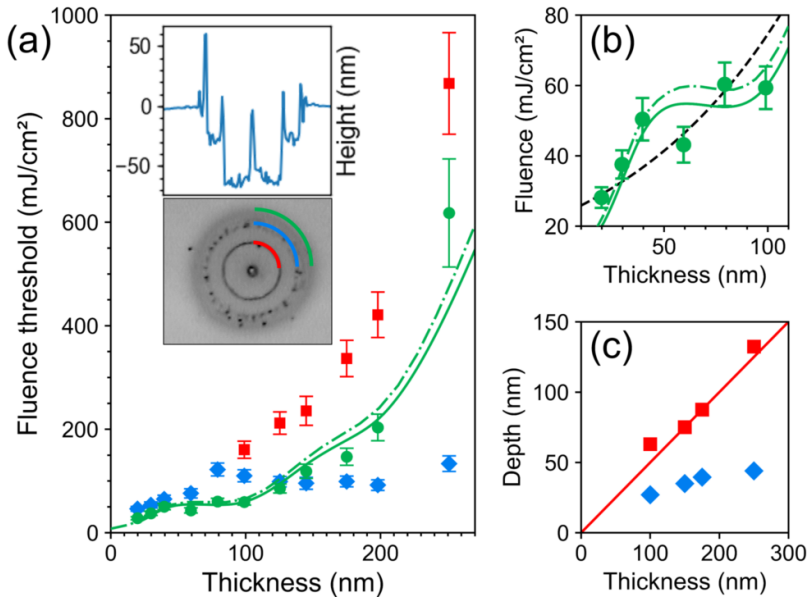


**Figure 7.2:** Laser-induced modifications in GST. (a) Measured threshold fluences as a function of film thickness (green circles: optical change; blue diamonds: first ablation; red squares: second ablation). The bottom part of the inset shows an optical microscope image of a spot on 100 nm thick GST exhibiting all three modifications. The upper part is an AFM depth profile across the same spot. Dash-dotted and solid lines are calculations based on TMM and combined TMM/T<sup>2</sup>TM, respectively. (b) Close-up on the thin-film regime of panel (a). (c) Measured crater depths of first- (blue) and second ablation (red) as a function of film thickness. The solid line has a slope of 0.5.

panel (e) they almost reach the silicon substrate. Second ablation appears at a higher fluence (towards the center of the spot), the boundary of which has been marked by the red dash-dotted line in panel (c). At a still higher fluence, within the orange box and blown up in panel (f), complete amorphization of the film suddenly takes place over less than 1  $\mu\text{m}$  in radius; this is evident by the disappearance of the grain boundaries from left to right. According to panel (a) there is no apparent change in optical contrast between regions (e) and (f). Thus permanent optical change is accomplished before (complete) amorphization of the film.

Although the results described above were based on one sample, we have

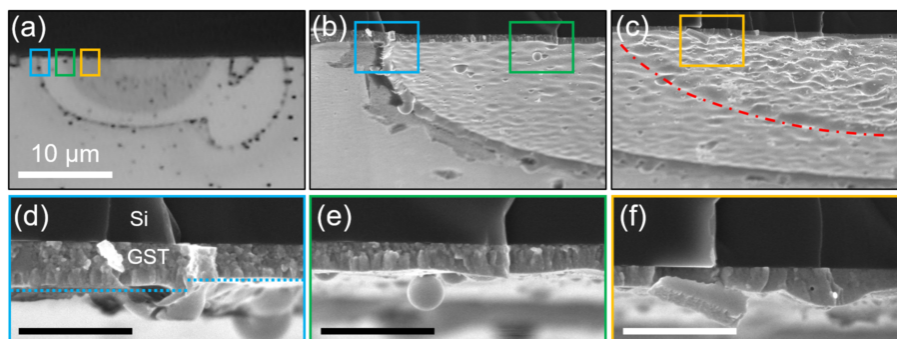


**Figure 7.3:** Optical (a) and SEM (b-f) images of the same laser-irradiated spot in GST. The sample was cleaved in half through the spot. (a) Three regions have been marked with colored boxes: blue contains the first ablation boundary, green contains the optical-change boundary, and orange contains the onset of amorphization as identified by the disappearance of grain boundaries from left to right (i.e. for increasing fluence). (b-c) Tilted SEM images where the corresponding boxes from (a) have been marked. The boundary of the second ablation crater is marked by the red dash-dotted line in (c). (d-f) Cross-sectional SEM images of the regions marked with blue, green, and orange, respectively. The scale bars in (d-f) are 500 nm. The dashed lines in (d) highlight the change in film thickness near the first ablation-crater edge.

carried out similar investigations on other samples with different thicknesses, presenting the same overall picture. A figure similar to Fig. 7.3 for a different sample is given in 7.G.3.

Lamellas of different regions of laser-irradiated spots on a 250 nm thick GST film were examined in cross-sectional TEM to study the structural modifications observed above in SEM in greater detail. Fig. 7.4(a) shows a cross-sectional TEM image around the first ablation-crater edge where part of the film has been removed to the right. The grains of pristine GST are clearly visible. The inset is a high-resolution TEM (HRTEM) of these grains showing several grain boundaries. The crystallites are randomly oriented as evidenced by the large differences in contrast between adjacent grains. Voids are present near the surface of GST, appearing as bright spots in the TEM image. That it is indeed voids was confirmed by observing the change in brightness upon over- and underfocusing [103].

Fig. 7.4(b) shows an image of an area somewhere between the first and second ablation boundaries. The formation of columnar grains almost cover

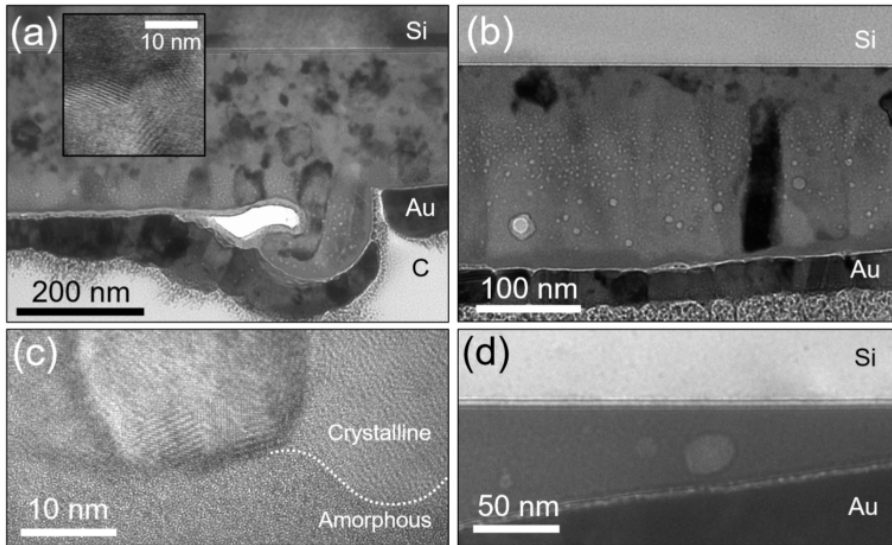


**Figure 7.4:** Cross-sectional TEM images of regions of laser-irradiated spots in a 250 nm GST film. (a) Near the edge of a first-ablation crater with part of the film removed to the right. Nano-sized voids are visible as bright dots in the surface region. Formation of short columnar grains are beginning to appear, starting from the free surface of GST. The inset shows a HRTEM image of the pristine grains. (b) Between first and second ablation, showing long columnar grains. Voids deep within the film are present. (c) HTREM image of the upper part of (b), highlighting a specific columnar grain. The first few nm are amorphous, while the rest of the film is crystalline. (d) At a fluence above the second ablation threshold, close to the threshold for complete removal of the film. The film is completely amorphous. The location of protective carbon (C) and gold (Au) layers have been indicated where appropriate.

the entire film except close to the Si substrate where the pristine grains remain. Voids are also present deep within the film. A thin, and very inhomogeneous, amorphous layer appears in the upper surface of the film. A HRTEM image highlighting the beginning of a columnar grain near the GST surface is shown in panel (c). The film is clearly polycrystalline except for the upper thin amorphous layer. Amorphization of the entire film is achieved only at higher fluences, as in panel (d), which is located after the second ablation crater.

It is worth noting that the thin amorphous layer, seen in the TEM images of Fig. 7.4, is most likely an artefact caused by the TEM sample preparation itself. The reason is that the amorphous layer is also present outside the first

ablation crater (panel (a) of Fig. 7.4) where there is no optical change (the threshold is located at much higher fluences, c.f. Fig. 7.2).

## 7.E Discussion

In this section we will discuss the implications of the results from section 7.D for optical change, amorphization, and ablation.

### 7.E.1 Optical change and amorphization

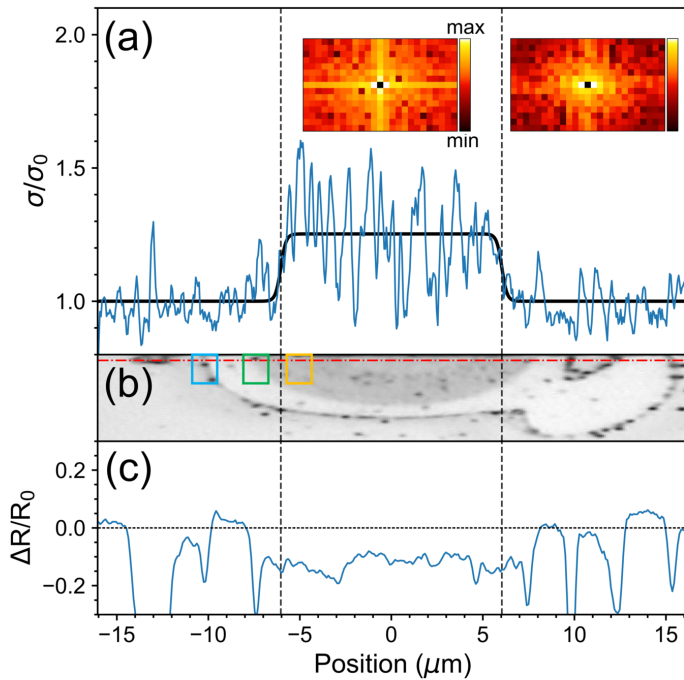
The qualitative observations made in connection with Fig. 7.3 show that the optical change precedes amorphization of the GST films, while both modifications display the same optical contrast under white-light illumination. To quantify these observations, we apply a 2-dimensional discrete fourier transform (DFT) locally to the cross sections of laser-irradiated GST. More precisely, the DFT is applied to a small rectangular selection – a “window” – of the cross-sectional SEM images of GST (such as those shown in Fig. 7.3); the window is then moved, parallel to the surface of the film, to map out the DFT at different local laser fluences. The nanoscale grains inside the crystalline regions can be described by a narrow range of spatial frequencies, determined mainly by the crystallite sizes, while the amorphous regions are characterized by a sharp zero-frequency peak (corresponding to a uniform background) on top of a broad frequency spectrum associated with image noise. Removing the zero-frequency peaks, and normalizing the DFT power spectra, yield narrow and broad spectral distributions of the crystalline and amorphous regions, respectively. The spread of a spectral distribution is summarized, somewhat crudely, by the square root of the variance of the distribution, which is then taken as a measure of the degree of crystallinity.

Fig. 7.5(a) displays the frequency spread  $\sigma$  of the laser spot, shown in Fig. 7.3, as a function of position from the center. Only the horizontal spread, that is, in the direction parallel to the GST surface, is shown (the DFTs were averaged in the vertical direction). The spread is normalized to a reference value  $\sigma_0$  of the crystalline region. The size of the DFT window was  $73 \text{ nm} \times 37 \text{ nm}$  (width times height). The estimated frequency spread fluctuates a lot because the DFT is quite sensitive to anomalies. Even so, there is a clear transition to an amorphous region of increased spread toward the center of the spot. The dark solid line is a fit to a smooth flat-top distribution

(transitions parameterized by Fermi-Dirac functions), and the two crystalline-amorphous transitions are marked by vertical dashed lines. Representative, normalized spectral distributions of the amorphous (center) and crystalline (right) regions are shown in the insets (the central zero-frequency peaks have been removed). Panel (b) depicts the optical microscope image of the laser spot, while panel (c) shows the change in reflectivity  $\Delta R$ , normalized to a reference value  $R_0$  of unirradiated GST, along a line just above the dash-dotted line indicated in panel (b). The colored boxes in Fig. 7.5(b) are the same as those depicted in Fig. 7.3(a). The crystalline-amorphous transitions are placed well inside the optically changed regions, thereby confirming the qualitative observation made in Section 7.D.2, namely that permanent optical change occurs at fluences lower than that required for amorphization.

Since the optical-change boundary is contained somewhere in the center of Fig. 7.3(e), it could be related to the formation of columnar grains of a length comparable to the film thickness. This is consistent with similar investigations on other samples, see 7.G.3 for an example. We note that a similar kind of columnar growth has been reported in [104], albeit in case of recrystallization by single-pulse fs irradiation of initially amorphous GST.

The columnar grain growth can be understood as follows: the laser-pulse absorption produces a sharp thermal gradient in the film towards the substrate. If the fluence is sufficient, the lattice will melt to a certain depth on the ps time scale. The melt front may grow a bit due to heat diffusion, but will cool soon after. (If the melt front is close to the Si substrate, the cooling rate will be particularly high.) During cooling, the molten state of GST is more likely to recrystallize bottom to top, seeded by the crystallites below the melt front. Since the cooling rate in pristine GST is slow due to its low thermal conductivity, the recrystallization could therefore result in the long columnar grains observed here, the length of the so-produced grains essentially matching the maximum melt depth. This explanation supposes that recrystallization of GST is growth-dominated. The same presumption was made based on short-laser-pulse recrystallization of melt-quenched GST [105, 106]. While giving a reasonable explanation for the formation of columnar grains, it also implies that amorphization will be difficult to achieve for increasingly thick films since any seed crystallites must be eliminated by entirely melting the film. This explains why amorphization appears rather suddenly at a specific fluence (radius) (Fig. 7.3(f) and 7.G.3) and not gradually throughout the whole laser-irradiated spot. That complete melting may be necessary for laser-induced amorphization has been reported in [78] in the case of GeSb



**Figure 7.5:** Crystalline to amorphous transitions of the same laser-irradiated spot depicted in Fig. 7.3. (a) Normalized spectral spread ( $\sigma/\sigma_0$ ) determined from local DFTs of SEM cross sections of the GST film. The spread increases in the amorphous region. The two insets show representative DFTs of the amorphous (center) and crystalline (right) regions. The solid line is a fit based on a smoothed flat-top function. Crystalline-amorphous transitions are marked by vertical dashed lines. (b) The associated optical image, the same as in Fig. 7.3(a). (c) Relative reflectivity change ( $\Delta R/R_0$ ) along a line just above the red dash-dotted line in panel (b).

films. Theoretical support of this explanation is provided by recent large-scale molecular dynamics simulations of ps laser-pulse excitation of silver, confined by a transparent solid overlay, and irradiated at fluences well above the melting threshold of silver. A similar kind of directed growth from surviving crystalline seeds was demonstrated – in this case located at the silver surface – where the growth began as soon as the surrounding material cooled below the melting temperature [32].

The observation that it is necessary for the columnar grains to approximately reach the Si substrate for optical change does not immediately provide an explanation of the mechanism causing the sudden optical change. As explained above, it does, however, imply that the energy density at some point has been sufficiently high to nearly melt the entire film. This can explain the strong thickness dependence as observed in Fig. 7.2(a-b). Indeed, the solid line in those panels is a combined TMM/TTM calculation of the optical-change threshold, assuming that it is necessary to raise the temperature of the entire GST film to the melting temperature at some instant after excitation. The precise criterion used in the simulations is that the energy density should exceed  $H_{cr} = C_{ph}T_m + L_m/2$ . The reason for this choice is that it implies partial melting; entire melting would correspond  $C_{ph}T_m + L_m$  and would, in our interpretation, result in complete amorphization. The TMM/TTM calculations are seen to reproduce the observed trend fairly well. We note that all the material parameters used in the simulations are based entirely on literature values (see 7.G.2 for a discussion). Interestingly, the trend is also very well described by calculations based only on TMM by reducing  $H_{cr}$  to 80% of its value. This reduction is reasonable because no loss of energy through heat conduction to the substrate is present in the TMM. The fact that TMM with and without TTM agree rather well is presumably due to the combination of slow heat conduction in GST and fast heat transfer to the Si substrate. If, for instance,  $R$  is increased by an order of magnitude, TTM will predict much lower threshold fluences for optical change (or melting) in case of thick films, as heat conduction raises the energy density on the backside of GST faster than heat is removed by the substrate. For comparison, a representative prediction of the optical-change thresholds based on Lambert-Beer absorption is shown as the black dashed line in Fig. 7.2(b); the model is clearly incapable of describing even a subset of the data. This failure highlights the importance of treating absorption in thin films rigorously as explained in section 7.C.

The important question regarding the physical mechanism responsible for laser-induced optical change in GST will now be addressed. As is now known,

optical change in GeTe alloys occurs already on the fs time scale after fs laser excitation [80–83]. A possible explanation of the induced optical change that fits the time-resolved observations is based on breaking of resonant bonds. The resonant bonds consist of second-neighbor angular alignment of  $p$ -orbitals, that potentially exist in crystalline states of GeTe alloys, which would then be responsible for the large optical constants (and hence high reflectivities) of the crystalline states as compared to the amorphous states, where the delocalized orbital alignment is absent [86]. It has recently been suggested that the experimentally observed rattling motion of Ge atoms, stimulated by the optical excitation, may drive the resonant-bond breaking and induce structural disorder (including amorphization) on longer time scales [83]. Our results show that permanent optical change can exist also in a crystalline state with roughly the same optical properties as the amorphous state. This is consistent with the resonant-bond picture if this supposed crystalline state, similar to the amorphous state, lacks resonant bonding. As discussed above, permanent optical change appears only when the entire film has been heated to about the melting temperature. We therefore suggest that the resonant bonds have to be ruptured simultaneously throughout the depth of film, otherwise they recover gradually from the remaining unperturbed resonant bonds on longer time scales. The supposed crystalline state, lacking resonant bonding, is probably a metastable state, produced by the efficient thermal quenching by the Si substrate. Our observations, of course, do not provide any direct evidence for this dynamical picture, but it appears physically plausible. The explanation, however, relies on the resonance-bonding picture of PCMs, which is still up for debate [84, 87].

### 7.E.2 Ablation

The results presented above give much indirect information about the ablation process. As noted in section 7.D, the entire GST film is removed by ablation in the thin-film regime. For  $\eta > 1$ , i.e. in the thick-film regime, the first ablation threshold reaches a constant value as expected [107]. We attribute this first ablation crater, in the thick-film regime, as being due to photomechanical spallation: photomechanical spallation occurs when a large compressive pressure, confined to the surface of the material, relaxes by expanding the free surface, thereby producing a strong tensile wave trailing the initial compressive wave travelling down the material. If the tensile component is sufficiently strong, it can cause rupture through cavitation (formation and nucleation of

voids) in a certain depth [108–112]. In thick films, where the laser-produced pressure is confined to the surface, this explanation predicts a threshold fluence independent of film thickness, in agreement with the data on first ablation.

It is important to remark that stress confinement is a necessary condition for occurrence of photomechanical spallation [109, 110]. That is, the time of energy transfer to the lattice, here given roughly by  $\tau_{\text{e-ph}} = 2.2$  ps [82], must be faster than the characteristic mechanical relaxation time. The latter may be estimated as  $\tau_s = \ell/v_s$  where  $v_s$  is speed of sound and  $\ell$  is the extent of the pressure zone. Using  $\ell \approx \alpha^{-1} = 85$  nm and  $v_s = 3.2$  nm ps<sup>-1</sup> [96], we get  $\tau_s \approx 27$  ps. Thus, stress confinement is clearly present in GST. Further evidence that the first ablation is caused by photomechanical spallation is provided by the observation of cavitation (i.e. formation of voids) in the surface layer surrounding the first ablation crater (Fig. 7.4(a)) together with the rough, corrugated surface, (Fig. 7.3(b-c)) which are well-known consequences of photomechanical effects [111, 112].

We note that the stress-confinement criterium in GST also holds for 800 nm excitation where the mechanical relaxation time is about 4 ps. Under these conditions, ablation at low fluences most likely proceeds by photomechanical spallation as well. This cannot, however, be true for ablation of GST by ps and ns lasers, where ablation might instead be caused by phase explosion.

The second ablation threshold is more challenging to explain. The observation of two ablation regimes in thin films [107, 113] with similar thickness dependence [114] has been reported, although in those cases, the films were found to be completely removed by the second ablation. In the present study, only approximately half of the film thickness is removed (see Fig. 7.2(c)). It is therefore not apparent whether the mechanisms are the same. The authors in [113, 114] attributed the two ablation regimes to “gentle” and “strong” ablation [33]. Strong ablation in bulk materials is generally caused by phase explosion, which is easily identified by the large number of droplets and clusters deposited around the ablation zone [110, 111]. Yet phase explosion should not exhibit any thickness dependence as observed in this study for second ablation. Besides, the second ablation craters reported here remain rather smooth if the fluences are not much larger than the ablation threshold.

A thickness dependent ablation threshold could be explained by the reflection of acoustic waves at the GST/Si interface. This phenomenon has been seen in molecular-dynamics simulations of free-standing Ni films due to constructive interference of forward- and backward-traveling tensile waves [109]. Based on values of the elastic constants of GST reported in [115], it is

found that approximately 11% to 21% of the wave amplitudes are reflected at the interface, depending on the crystallographic orientation of GST (Maxim V. Shugaev, Personal communication, August 2018). This corresponds to a reflected amount of energy of roughly 1% to 5%, which is potentially large enough to have an impact. The acoustic impedance of GST is, however, lower than that of Si, meaning that the phase is preserved upon reflection. Hence, the compressive and tensile waves interfere destructively near the interface, which could help stabilize the GST film against complete detachment from the Si substrate. The compressive and tensile waves, reflected at the GST/Si, may interfere later upon reflection from the upper spall layer, (resulting from first ablation) where they undergo a phase shift due to the reduced impedance of this layer compared to the surroundings. Whether this may reproduce the thickness-dependent second ablation threshold observed in this study, depends on the detailed dynamics of the process, e.g. how quickly acoustic waves are damped in GST. Another factor that may influence the process is that the density of amorphous GST is 6% higher than that of crystalline GST [116]; presumably, the molten state is at least as dense. At present, we are unable to determine uniquely the mechanism behind the second ablation, but hopefully more advanced simulations, such as molecular dynamics, will in the future shed more light on this issue.

## 7.F Conclusion

In conclusion, we have studied fs laser-induced modifications in crystalline GST films. We found that the onset of optical change can occur at a lower fluence than that required for complete amorphization of the films, and that the latter is not accompanied by any additional change in optical contrast. Thus, it is possible to achieve optical switching without complete amorphization by fs irradiation. The threshold fluences for optical change and amorphization were found to be strongly dependent on film thickness, which was explained in terms of TTM simulations by assuming that partial melting of the entire film is required. That substantial heating did occur was supported by the observation of long columnar grains growing with increasing fluence, and appearing to bridge approximately the entire film near the optical-change boundaries. In addition, two distinct zones of ablation were observed on thick (larger than 80 nm) GST films. The low-fluence threshold was found to proceed by photomechanical spallation.

**Acknowledgements** This work was funded by Innovation Fund Denmark through the SunTune project. The authors would like to thank John L. Hansen for performing the XRD and RBS measurements, and Maxim V. Shugaev and Leonid Zhigilei (University of Virginia) for insightful comments and fruitful discussion.

## 7.G Appendix

### 7.G.1 Determination of thresholds

For a Gaussian laser beam, the fluence profile is given as  $F(r) = F_0 e^{-2r^2/\omega^2}$ , where  $r$  is the distance from the center of the spot, and  $\omega$  is the laser beam spot size. The threshold fluence for a modification of diameter  $D$  is found by equating  $F(D/2) = F_{\text{th}}$ , leading to

$$D^2 = 2\omega^2 \ln \frac{F_0}{F_{\text{th}}}. \quad (7.4)$$

If several modifications are present as in Fig. 7.1, then there is an equation of the type in Eq. (7.4) for each modification. Thus, for the  $i$ th modification, we have

$$D_i^2 = 2\omega^2 \ln \frac{F_0}{F_{\text{th},i}}. \quad (7.5)$$

The relation between peak fluence and pulse energy,  $E_p$ , is  $F_0 = 2E_p/\pi\omega^2$ , and it can be convenient in the analysis to replace the fluences in Eq. (7.5) with the associated pulse energies, and convert to fluences only in the end. By recording the size of the modification at different pulse energies, the threshold fluence (or equivalently, threshold energy) can be determined from Eq. (7.5). Fig. 7.6 shows two examples for 100 nm (a), and 190 nm (b) thick GST films, both showing three modifications (optical change, first ablation, and second ablation). The data were fitted to Eq. (7.5) simultaneously to give the same laser beam spot size  $\omega$ . To find the dimensions of modifications, ellipses were fitted to their boundaries. By using ellipses instead of circles, deviations from circularity could be assessed, which was used to estimate the error bars shown in Fig. 7.6. The errors are relatively small, which shows that the laser beam is circular to a good approximation.

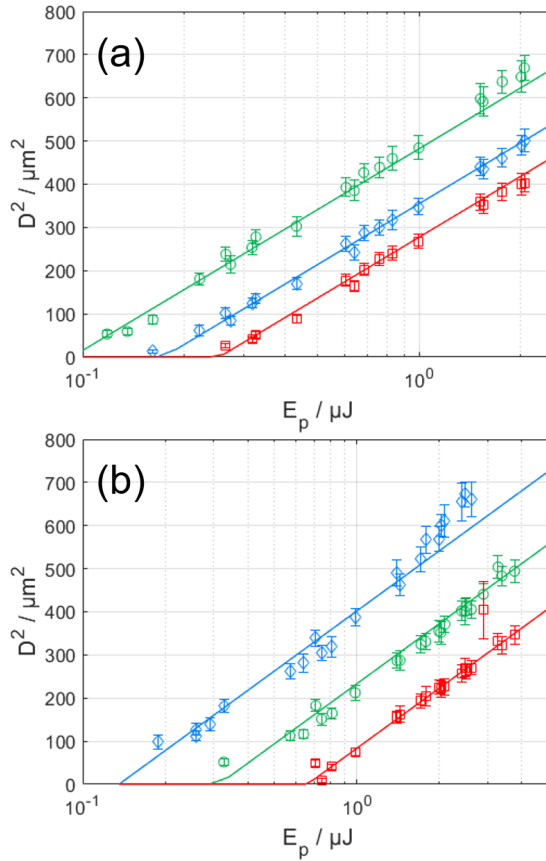


**Figure 7.6:** Diameters squared of the laser-induced modifications versus the logarithm of the pulse energy for 100 nm thick GST (a), and 190 nm thick GST (b). The obtained laser beam spot size in both cases are  $w = 10.1 \pm 0.2 \mu\text{m}$ . Three modifications are present: optical change (green circles), first ablation (blue diamonds), and second ablation (red squares). The solid lines are simultaneous fits to Eq. (7.5) for all three types of modifications.

## 7.G.2 Modelling details

### Thermal properties

The relation between the energy density  $H$  and the temperature  $T$  is  $H(T) = \int_0^T T' C(T') dT'$ , where  $C$  is the volume-specific heat capacity. For the lattice, we take a constant value,  $C_{\text{ph}} = 1.38 \times 10^6 \text{ J m}^{-3} \text{ K}^{-1}$ , which is a reasonable simplification as the Debye temperature is close to room temperature [97]. The melting temperature of GST is  $T_{\text{m}} = 621 \text{ }^\circ\text{C}$ , and the heat of fusion is  $L_{\text{m}} = 7.0 \times 10^8 \text{ J m}^{-3}$  [98]. To account for melting, the heat capacity of the lattice is taken to be  $C'_{\text{ph}}(T_{\text{ph}}) = C_{\text{ph}}/2 + L_{\text{m}}/2\varepsilon$  for  $|T_{\text{ph}} - T_{\text{m}}| \leq \varepsilon$ , where  $\varepsilon \ll T_{\text{m}}$ ; this fixes the temperature around  $T_{\text{m}} \pm \varepsilon$  during melting. For  $T > T_{\text{m}} + \varepsilon$ , the material is melted and thus in its liquid state. For the liquid state of GST, we use the same values for  $\kappa_{\text{ph}}$  and  $C_{\text{ph}}$  as in the solid state due to lack of better alternatives. The thermal conductivity is taken to be  $\kappa_{\text{ph}} = 0.45 \text{ W m}^{-1} \text{ K}^{-1}$  [96].

For the electronic system, the values of  $C_e$  and  $\kappa_e$  are generally taken to be proportional to  $T_e$ , i.e.  $C_e = \gamma T_e$ ,  $\kappa_e = \kappa_{e,0}(T_e/T_0)$  where  $T_0 = 293 \text{ K}$  is room temperature. The electron contribution to the thermal conductivity of GST at  $T_0$  is about  $\kappa_{e,0} = 0.04 \text{ W m}^{-1} \text{ K}^{-1}$  [96]. In [117] it was estimated that the electron specific heat is less than  $0.08 \text{ J mol}^{-1} \text{ K}^{-1}$ . Choosing the upper limit, we get a value  $\gamma \approx 20 \text{ J m}^{-3} \text{ K}^{-2}$ . This choice is somewhat arbitrary of course, but the exact value of  $\gamma$  (and  $\kappa_{e,0}$  for that matter) does not influence the estimation of optical-change thresholds significantly.

An experimental value of  $\tau_{\text{e-ph}} = 2.2 \text{ ps}$  for the inverse electron-phonon coupling rate has been reported in [82] for GST. The relation to the coupling strength is assigned according to [65, 95]

$$g = \frac{C_e}{\tau_{\text{e-ph}}}. \quad (7.6)$$

It is important to note that the values and temperature scalings of the thermal parameters above are based on experimental values of fcc-GST, all obtained under equilibrium conditions at low temperatures (below  $400 \text{ }^\circ\text{C}$ , as higher temperatures converts the metastable fcc phase into the stable hcp phase). The values used in our simulations are bound to deviate from the correct values at very high temperatures (for instance, the linear temperature scaling of  $\kappa_e$  and  $C_e$  breaks down). However, no better values (such as from ab-initio simulations) appear to be available for GST at elevated temperatures.

### Effect of carrier transport

The carrier mobility in fcc-GST is approximately  $1 \text{ cm}^2 \text{ V}^{-1}$  [118]. From the Einstein relation, the diffusion coefficient of carriers is  $D \approx (10^{-6} \text{ m}^2 \text{ s}^{-1})T_e/T_0$ , where  $T_0 = 293 \text{ K}$ . The characteristic time scale of carrier diffusion is therefore  $t_{\text{diff}} \sim L^2/D$ , where  $L$  is a characteristic length scale. Similarly, the electronic thermal time scale is  $t_{\text{thermal}} \sim L^2\gamma T_0/\kappa_{e,0}$ . The ratio is  $t_{\text{diff}}/t_{\text{thermal}} = \kappa_{e,0}/D\gamma T_0 \sim 10 \times (T_0/T_e)$ . After electron-phonon equilibration, we typically have  $T_e \sim 10 \times T_0$ , and therefore it follows that the two time scales are similar. Consequently, the spatial distribution of the carrier temperature and concentration will be roughly the same, which justifies the approximation of considering only thermal diffusion.

### Boundary conditions

Due to the band-gap mismatch between GST and Si, transport of electrons (and holes) through the interface is likely only a minor effect, and is consequently ignored. Thus, the generated conduction-band electrons are trapped in the GST film. Insulating boundary conditions for the electronic heat transport are therefore appropriate (i.e.  $\partial T_e/\partial x = 0$  at the boundaries of GST). In case of the lattice heat transport, insulating boundary conditions are taken at the GST/air interface, while heat-preserving boundary conditions are presumed at the GST/Si interface [119]:

$$-\kappa_{\text{ph}}^{\text{GST}} \frac{\partial T_{\text{ph}}^{\text{GST}}}{\partial x} = \frac{T_{\text{ph}}^{\text{GST}} - T_{\text{ph}}^{\text{Si}}}{R} = -\kappa_{\text{ph}}^{\text{Si}} \frac{\partial T_{\text{ph}}^{\text{Si}}}{\partial x}. \quad (7.7)$$

The backside of the silicon substrate (which is 0.5 mm thick) is fixed to ambient temperature (293 K).

The thermal boundary resistance,  $R$ , is a crucial parameter as it determines the rate at which GST is cooled by the Si substrate. Its value can be estimated using the Diffuse-Mismatch Model [120] based on values from [96]. This yields  $R \approx 1.0 \times 10^{-8} \text{ m}^2 \text{ K W}^{-1}$ .

### Implementation

The nonlinear TTM equations (Eqs. (7.1) and (7.2)) are solved by the finite-difference method in a backward Euler scheme (fully implicit and first order in time) using the split-step method in which the electron-phonon coupling term

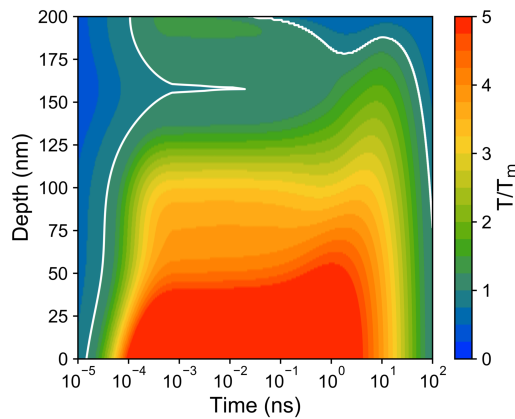


**Figure 7.7:** Simulated evolution of the lattice temperature (color scale) in a 200 nm GST film irradiated at the threshold fluence for optical change. The solid white line is a contour line of temperature  $T_m$ . The scale was truncated at  $5T_m$ .

is integrated with a much finer time-resolution than the heat-conduction terms (which are costly to integrate and are significant only on a longer time scale) [121], modified according to the procedure described in [122] for efficiently treating phase-transition problems. The basic idea is to linearize the energy densities  $H$  (and other nonlinear parameters) in the temperature  $T$ , solve the system of linear equations for  $T$ , update the energies according to the linearized temperature changes, and, finally, correct the temperatures by inverting the energy expression. The corrected temperatures are then used for the next step in an iterative scheme to solve the full nonlinear system for one time step until convergence (i.e.  $H$  and  $T$  are consistent). By ensuring consistency between  $T$  and  $H$  at all times, no (sudden) phase transition will be missed.

An example of a TTM simulation is shown in Fig 7.7 for a 200 nm GST film irradiated at the (simulated) threshold fluence for optical change, the criterion being that the entire film has to reach the melting temperature  $T_m$  at one instant in time. (Note that  $T_{\text{ph}} = T_m$  corresponds to partial melting; complete melting occurs when  $T_{\text{ph}} \geq T_m + \varepsilon$ .) Interference causes a local minimum in absorption at a depth of approximately 150 nm. The backside of the film is quickly cooled through the Si substrate; heat conduction in the GST film is generally insufficient to ever significantly reheat the back of the film.

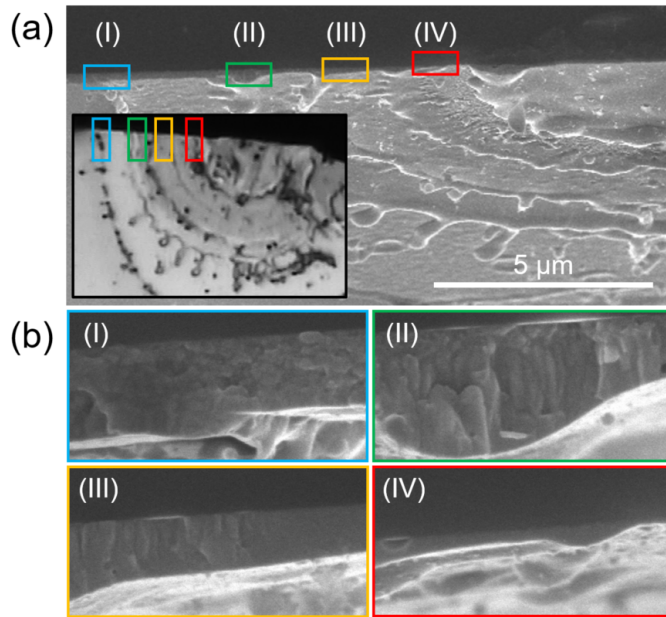


**Figure 7.8:** Cross-sectional SEM image of a laser-irradiated spot in a 250 nm GST film. (a) Tilted SEM overview of the spot. Regions (I-IV) corresponds to the boundaries of first ablation, optical change, complete amorphization, and complete film removal, respectively. The inset shows an optical microscope image of the same spot. The contrast in the optical microscope image has been adjusted to make the optical change more apparent. (b) Close-ups of regions (I-IV).

### 7.G.3 Cross-sectional SEM

Another example demonstrating optical change before complete amorphization is provided in Fig. 7.8 for the case of a 250 nm thick GST film. Regions of first ablation and complete removal of the film are also shown. Region (II) (green) in panel (a) contains the boundary for optical change; its location has been marked both in the SEM- and optical microscopy image (inset). Panel (b) provides the cross sectional view, showing the formation columnar grains that begin to almost reach the Si substrate to the right (region (II)).

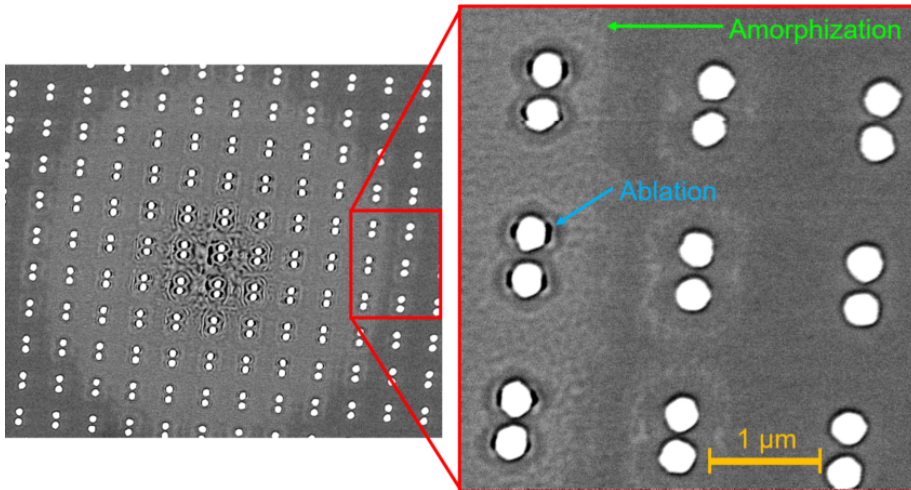


**Figure 7.9:** *Left.* Laser-irradiated spot of GST film with nanoparticles on top. The bright annular region indicates the amorphized parts of the film. *Right.* Close up at the amorphization boundary. Ablation (blue arrow) happens just around the nanoparticles while amorphization is inhibited (lack of bright regions around the nanoparticle).

### 7.3 Near-field marking and $\text{Ge}_2\text{Sb}_2\text{Te}_5$

We close this chapter on GST by explaining *why* the material is not suited for imaging near fields of gold nanoparticles.

The problem is illustrated in Fig. 7.9, which shows an SEM image of a laser-irradiated spot on a 40 nm GST film with gold nanodimers (i.e. pairs of disks) on top, arranged in a periodic pattern. The peak fluence of the laser pulse barely reached the ablation threshold, as evident by the partially ablated centre. The bright annular region shows the amorphized parts of GST. A close up near the amorphization boundary is shown on the right; slight ablation occurs around the left-most column of nanoparticles. However, there is no evidence of amorphization near the nanoparticles where the NFE is largest. Instead, amorphization appears to be inhibited around the nanoparticles!

Fig. 7.9 is just one out of many examples of this lack of amorphization. We argued in Section 7.E.1 that a necessary condition for amorphization of GST appears to be complete melting of the film. This explains the missing amorphization near the nanoparticles: The extremely localized near fields

of the nanoparticles implies localized melting. Because thermal diffusion in GST is slow, and cooling by the silicon substrate is rapid, the entire film never melts through the entire depth close to the nanoparticles. Note that amorphization of GST for near-field imaging worked in Refs. [10, 11], but that is probably because the authors used dielectric microspheres, which has much less near-field localization than metal nanoparticles.

# TRANSIENT OPTICAL PROPERTIES OF EXCITED DIELECTRICS

In this chapter, we examine the transient optical properties of fused silica, excited by ultrashort laser pulses above the ablation threshold. The properties are tracked by simultaneously recording  $s$ - and  $p$ -reflectivities ( $R_s$  and  $R_p$ , respectively) of ultrashort visible probe pulses. An *apparent* birefringence emerges  $\sim 100$  fs after pump pulse excitation, after which  $R_s$  and  $R_p$  cannot be described by reflection from an air–solid interface with *any* dielectric constant of the solid. This feature is observed over a wide range of probe wavelengths, as well as on a different dielectrics (sapphire). A simple optical model based on the creation of a thin electron cloud outside the dielectric through electron emission, can explain all the features of our measurements, thereby resolving the apparent birefringence.

The main text and the supplemental material included below was submitted to Physical Review Letters.

## 8.1 Contributions

I have carried out all the measurements, created the figures, analyzed the data, and written most of the manuscript. Sebastian T. Andersen has carried out

an extensive amount of measurements on sapphire, which, however, is not included here. The manuscript has been through a lot of versions; besides the authors, Lasse Haahr-Lillevang, Thomas Winkler, and Brian Julsgaard, has carefully read, commented and critiqued on early drafts. (Brian has, in fact, commented on several, early as well as late, versions of the manuscript.)

The manuscript has been reproduced below with slight changes to a few of the figures; the content is exactly the same, but the panels have been moved around to adapt these figures on an A5 page.

## Transient optical properties of highly excited dielectric materials at variance with reflection from an air–solid interface: Signatures of ultrafast electron emission

Søren H. Møller, Sebastian T. Andersen, Peter Balling

Department of Physics and Astronomy, Aarhus University, Ny Munkegade 120, DK-8000 Aarhus C, Denmark

**Abstract:** The ultrafast dynamics of short-pulse-laser-excited fused silica is investigated by measuring polarization-resolved reflectivities of a wavelength-tunable probe pulse following a near-infrared pump pulse. This data, which should in principle allow a determination of both real and imaginary parts of the time-dependent refractive index, turn out to become incompatible with reflection from an air–solid interface after  $\sim 100$  fs. We show that an apparent birefringence can be resolved by introducing the ultrafast formation of a thin electron cloud in front of the dielectric sample.

Dielectric materials undergo rapid changes when excited by intense, ultrashort light pulses. The earliest response is dominated by the carriers, resulting from a drastic rearrangement of electrons between the energy levels (bands) of the material: valence-band (VB) electrons are promoted to the conduction band (CB), typically via strong-field excitation by visible and IR laser pulses [24, 30, 94, 123]. The free carriers, i.e. the CB electrons and VB holes, form an electron-hole (e-h) plasma, which is responsible for an increased reflectivity (plasma-mirror effect [124]) and absorption in the dielectric material. This absorption plays an important role for energy deposition in the late parts of the laser pulse; it leads to heating of the plasma in a thin layer and opens up for collisional excitation of additional carriers from VB to CB (potentially leading to avalanche ionization [30]). After the laser pulse, the carriers thermalize among themselves by intra- and inter-band collisions and after tens of ps also with the lattice, thereby transferring energy to the atoms in the solid. At this point, if the excitation is strong enough, ablation – removal of atoms from the solid – may be initiated, for example if the thermal energy of atoms exceed their binding energy.

Tracking the transient changes in material properties with high temporal resolution can be accomplished in pump-probe schemes using ultrashort laser pulses [125–134]. Such experiments provide valuable insight into the transient states of the laser-excited materials outlined above and can guide theoretical descriptions of the dynamics, also when explaining new phenomena, like the

recently discovered LADIE (light amplification in excited dielectrics) effect [135]. The (complex) dielectric constant  $\varepsilon$  determines the optical properties of a system, and is thus an extremely useful quantity to measure for understanding and making future predictions about the transient states of excited materials. Since laser excitation is typically very inhomogeneous in depth,  $\varepsilon$  varies through the material. Nevertheless, an effective value (a so-called pseudo- $\varepsilon$  [136]) can be inferred through polarization-resolved reflectivity measurements by inversion of the Fresnel equations [125, 131, 137].

Here, we report on time- and polarization-resolved reflectivity measurements on fused silica ( $\text{SiO}_2$ ), excited well above the ablation threshold, with focus on the ultrashort time scale after laser-pulse excitation. We used wavelength-tunable probe pulses with the original goal of experimentally determining the transient dielectric constant at different wavelengths. To our surprise, the measured reflectivities of  $p$ - and  $s$ -polarized light at all applied wavelengths (480-730 nm) become – and remain – incompatible with reflection from an air-solid interface  $\sim 100$  fs after excitation. In this letter, we propose an extension of the optical model, which includes the effects of a cloud of emitted electrons originating from the laser-excited dielectric target. This electron cloud, in combination with a time-dependent scattering rate in the Drude description of the excited material, provide a good description of the experimental data.

The experimental setup is a typical pump-probe scheme, which is described in detail in the supplemental material Section 8.A. Briefly, the pump and probe pulses derive from a regeneratively amplified Ti:sapphire laser. The pump pulse (of duration 45 fs FWHM) is sent through a computerized delay line and focused at normal incidence to a spot size (radius at  $1/e^2$ ) of  $30 \mu\text{m}/23 \mu\text{m}$  (vertical/horizontal) onto the sample (dielectric target), which is mounted on a computer-controlled 3-axis stage. An optical parametric amplifier (TOPAS) produces wavelength-tunable probe pulses (durations of about 50 fs or less). The electric-field polarization of the probe beam is rotated by roughly  $45^\circ$  so that it contains almost equal mixtures of  $s$ - and  $p$ -polarized components on the sample, onto which it is focused at an incidence angle  $\theta = 59.5 \pm 1.0^\circ$ . The reflected probe pulse, which is significantly larger than the pump beam on the sample, is imaged via a long-working-distance microscope objective (20 $\times$ , NA = 0.42) onto a camera (CMOS, 8-bit). A birefringent calcite crystal, mounted before the camera, spatially separates the  $s$ - and  $p$ -polarized components of the probe pulse onto two distinct sections on the camera sensor. In this way, simultaneous  $s$ - and  $p$ -polarized images are captured of the pump-excited surface. Band-pass filters (10-40 nm broad) are placed after the microscope

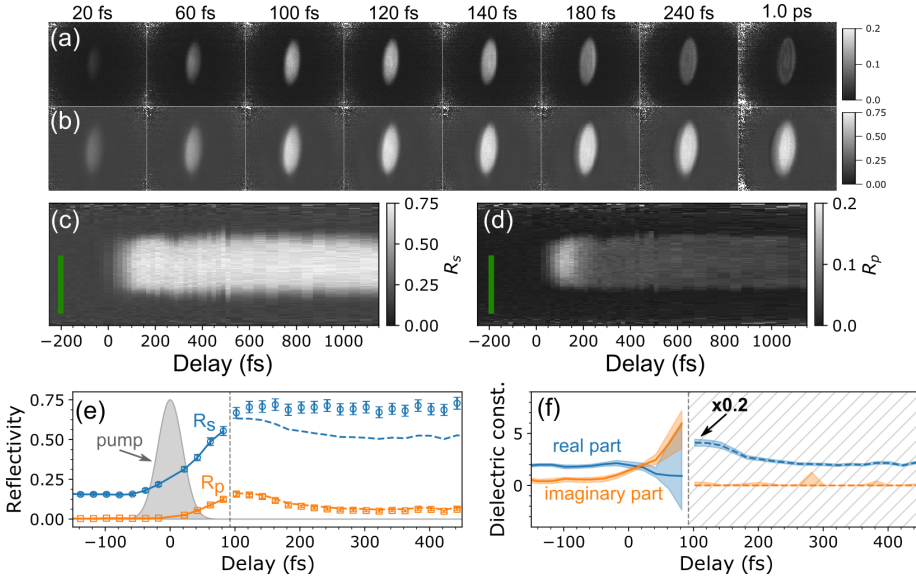


**Figure 8.1:** Reflectivity at 700 nm of fused silica after pump excitation. (a-b) Selected images at different time delays of  $R_p$  (a) and  $R_s$  (b). (c-d) Reflectivity time series along a vertical slice passing through the center of the pump spots in (a) and (b). The green bars indicate the pump-beam spot size (30  $\mu\text{m}$ ). (e) Time evolution of  $R_s$  (blue circles) and  $R_p$  (orange squares) in the center of the pump spot. The envelope of the pump pulse has been highlighted by gray. The solid and dashed lines represent the reflectivities reconstructed from the transient dielectric constant  $\varepsilon$  shown in panel (f). The lightly shaded ribbons in panel (f) indicate 68% credible intervals centered on the mean values of  $\varepsilon$  (solid and dashed lines). The real part of  $\varepsilon$  is scaled down by a factor of 5 in the hatched region.

objective to filter out unwanted stray light. Absolute reflectivities of the probe pulses following a pump pulse are obtained as explained in Section 8.A. The sample is moved to a fresh location after each pump shot.

Fig. 8.1 shows an example of measurements acquired on fused silica with 700 nm probe light. The average pump-pulse energy was 62  $\mu\text{J}$  corresponding to a peak fluence of about 5.7  $\text{J cm}^{-2}$  (peak intensity  $\sim 100 \text{ TW cm}^{-2}$ ), which is about 2 times the ablation threshold fluence ( $\sim 2.9 \text{ J cm}^{-2}$ ). Panels (a) and (b) show a few selected images of the  $p$ - and  $s$ -polarized reflectivities ( $R_p$  and  $R_s$ ), respectively, at different delay times. The emerging bright central spot reflects the large free-carrier density created by the pump pulse, viewed under an angle

of  $60^\circ$ . Panels (c) and (d) show the detailed time evolution of  $R_p$  and  $R_s$  along a fixed vertical slice passing through the center of pump spots in panels (a) and (b), while the data points in panel (e) show the reflectivities in the center of the pump-excited area. Two prominent features are observed: (i) Both  $R_s$  and  $R_p$  increase until  $\sim 100$  fs after the material excitation, and (ii)  $R_p$  exhibits a subsequent decrease between 100 and 200 fs. The time scale “ $t = 0$ ” has been set by comparison to the optical model described later to eliminate the uncertainty associated with the experimental determination of the temporal pump-probe overlap, detailed in Section 8.A.

The delayed onset of a reflectivity increase [feature (i)], which continues after the pump pulse is over, has been seen in previous investigations [129, 130]. Such behavior is not easy to explain if the dynamics is governed primarily by the growth of the e-h density inside the dielectric target, where the fastest reflectivity increase should happen during the pump pulse; this is the case even if collisional excitation is contributing, as this mechanism happens on a few-femtosecond time scale [138, 139]. However, as will be shown quantitatively below, the delayed increase in reflectivities can be explained within the Drude model by a gradual decrease of the scattering rate, possibly due to thermalization of the e-h plasma.

The subsequent drop in  $R_p$  [feature (ii)] deserves careful attention. Assuming that the optical properties of the (inhomogeneously) excited dielectric can be represented by a pseudo-dielectric constant  $\varepsilon$ , its value can be inferred from the data in panel (e) of Fig. 8.1 by inverting the Fresnel equations for  $R_s$  and  $R_p$  at an air–solid interface; the results are shown in Fig. 8.1, panel (f). Initially, we observe an increase in the imaginary part [ $\text{Im}(\varepsilon)$ ] and a reduction of the real part [ $\text{Re}(\varepsilon)$ ], which is consistent with the optical signature of an e-h plasma. The values of  $R_s$  and  $R_p$  calculated from  $\varepsilon$ , shown as the solid and dashed lines in panel (e), confirm that this  $\varepsilon$  fits the data at early times. However, after 90 fs, which coincides with the onset of the drop in  $R_p$ , the method fails (hatched regions): the real part increases to unphysical values (ranging from 10–20), the imaginary part drops to zero, and the observed values of  $R_s$  and  $R_p$  are not simultaneously reproduced. Thus the data cannot be described by *any* complex value of  $\varepsilon$ , due to the large difference between  $R_s$  and  $R_p$ , which develops because of the drop in  $R_p$  (see Section 8.A for a proof that no solutions exist).

Then what is the origin of the drop in  $R_p$ ? Essentially, what the data exhibit is an *apparent* transient birefringence, since the effective optical parameters for the two polarizations are different. The first thing to consider is the

effect of the strong gradient in the excitation of the dielectric material, which questions the validity of the Fresnel equations using a pseudo- $\varepsilon$  [128]. However, more advanced (numerical) solutions of Maxwell's equations clearly show that this effect has similar influence on  $s$ - and  $p$ -polarized light and thus cannot explain the apparent birefringence. What about the effect of self-trapped excitons (STEs), which are known to form quickly (well before 1 ps) after laser excitation of fused silica and strongly influence the optical properties [27, 126]? The formation of STEs is prohibited near the surface of the solid for the reasons discussed in [134], which makes their optical signature extremely weak in reflection measurements. Furthermore, preliminary investigations on sapphire (which has no STEs) exhibit a similar drop in  $R_p$ . Another explanation to discuss has been proposed in two previous reports of a subsequent drop in  $R_p$ : Refs. [127, 133] attributed an observed ultrafast decrease in  $R_p$  to *resonance absorption*, which involves excitation of longitudinal plasma waves. The condition for resonance absorption is that  $\text{Re}(\varepsilon) = 0$  [140], and only  $p$ -polarized waves can excite the resonance because an electric-field vector along the plasma gradient is required. We will argue that resonant absorption does not explain the drop in  $R_p$  after presenting data for more probe wavelengths.

Instead, as an attempt to explain the data, we propose to include the effect of an electron cloud positioned just in front of the dielectric target. Such a cloud (plasma) may readily be formed by the laser-heated hot electrons that escape the target [141, 142]. A simplified model of the situation is sketched in Fig. 8.2, panel (a), showing the high-density e-h plasma (labeled “2”) inside the laser-excited target material (fused silica), and the low-density electron cloud (labeled “1”) outside. The target surface is placed at  $z = 0$ . The free-carrier densities  $n_i$  in each region ( $i = 1, 2$ ) are assumed to vanish over some characteristic length scale  $\ell_i$  as  $n_i(z) = n_{0,i} \exp(-|z|/\ell_i)$ . The dielectric constant  $\varepsilon_i(z)$  in both plasmas is taken to follow the Drude model

$$\varepsilon_i(z, \omega) = \varepsilon_{b,i}(\omega) - \frac{\omega_{p,i}^2(z)}{\omega^2 + i\omega\Gamma_i}, \quad (8.1)$$

where  $\varepsilon_{b,i}$  is the dielectric constant of the unperturbed materials (e.g.  $\varepsilon_{b,1} = 1.0$  for air),  $\Gamma_i$  is the phenomenological scattering rate,  $\omega_{p,i}(z) = \sqrt{e^2 n_i(z) / \varepsilon_0 m_i}$  is the plasma frequency,  $m_i$  is the (reduced) carrier mass, and  $\omega$  is the probe frequency. The reduced e-h mass is set to  $0.43m_e$  inside fused silica [134].  $R_s$  and  $R_p$  are calculated by solving the Helmholtz equations based on the procedure described in Section 8.A.

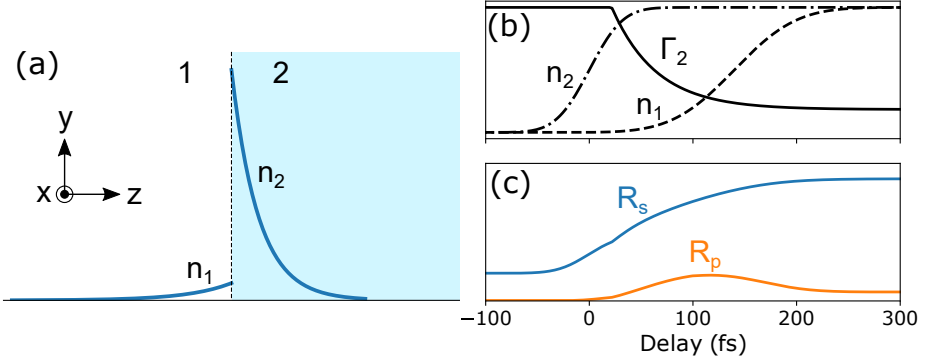


**Figure 8.2:** (a) Sketch of the model geometry. The vertical dotted line separates the domain into two parts at  $z = 0$ : air (labeled “1”) and fused silica (labeled “2” and colored light-blue). The solid blue curves depict the free-electron densities  $n$  that make up the electron cloud (region 1) and the e-h plasma (region 2). Perfect symmetry in  $x$  and  $y$  is assumed. (b) Assumed time evolution of the electron densities  $n_1$  and  $n_2$ , and scattering rate  $\Gamma_2$  at  $z = 0$  [see Eq. (8.2)]. (c) Associated reflectivity changes of  $R_s$  and  $R_p$  at  $60^\circ$  angle of incidence.

To model the dynamics of the reflectivities, we envision the time evolution of  $n_{0,i}$  and  $\Gamma_2$  depicted in Fig. 8.2, panel (b). The e-h density  $n_{0,2}$  increases while the pump pulse is “on” with a presumed time scale of  $\tau_2 = 60$  fs, effectively incorporating the temporal overlap between the pump and probe. Near the end of the pulse, the scattering rate of the e-h plasma  $\Gamma_2$  gradually decreases, e.g. through thermalization of the carriers, down to a certain “steady” value. Meanwhile, the electron cloud forms in front of the dielectric (region 1);  $n_{0,1}$  increases. Panel (c) shows the resulting time evolution of  $R_s$  and  $R_p$ . Both reflectivities increase as  $\Gamma_2$  decreases, and when  $n_{0,1}$  reaches a sufficient value,  $R_p$  starts to drop while  $R_s$  is more or less unaffected. This confirms that the model is able to reproduce features (i) and (ii) described above.

Specifically,  $R_s$  and  $R_p$  are modeled by assuming a simple error-function growth of the densities and exponential decrease of the scattering rate:

$$n_{0,2}(t) = n_{2,\infty} \operatorname{erfc} \left[ -\sqrt{4 \ln 2} \frac{t}{\tau_2} \right], \quad (8.2a)$$

$$n_{0,1}(t) = n_{1,\infty} \operatorname{erfc} \left[ -\sqrt{4 \ln 2} \frac{(t - t_0)}{\tau_1} \right] \frac{n_{0,2}(t)}{n_{2,\infty}}, \quad (8.2b)$$

$$\Gamma_2(t) = \begin{cases} \Gamma_{2,0} & t < \xi \\ \Gamma_{2,\infty} + (\Gamma_{2,0} - \Gamma_{2,\infty})e^{-(t-\xi)/T} & \xi \leq t \end{cases} \quad (8.2c)$$

The “ $\infty$ ” subscript indicates the “steady-state” values of the parameters, which in this context means the values after  $\sim 300$  fs (c.f. Fig. 8.1).  $\tau_1$  is the time scale for growth of the electron cloud. Note that  $n_{0,1}$  is assumed proportional to  $n_{0,2}$  as the electrons originate from the solid. Inspired by the experimental results in [131], we assume an exponential decrease of  $\Gamma_2$  from an initial value  $\Gamma_{2,0} > \Gamma_{2,\infty}$  with time constant  $T$ .  $t_0$  and  $\xi$  are time offsets relative to the pump pulse (“ $t = 0$ ”).

The physical origin of the drop in  $R_p$  can, in fact, be explained as an interference phenomenon: The thin electron cloud provides an additional interface, from which the incident probe pulses are reflected. However, the cloud has different effects for the two polarizations: for  $p$ -polarized light, the additional reflection is out of phase with that from the solid, which is not the case for  $s$ -polarized light. Consequently, the drop in the  $p$ -reflectivity is a signature of destructive interference. Representing the cloud by a pseudo- $\varepsilon$ , it can be shown (see Section 8.A) that a necessary condition for such a phase relation is  $\varepsilon_1 < \sin^2 \theta$ , which makes the  $z$ -component of the wave vector in the cloud imaginary. In our experiment ( $\sin^2 \theta \approx 0.75$ ), this condition is fulfilled as soon as the electron density in the cloud becomes appreciable.

So far we have based our discussion on the measurements with a 700 nm-probe. However, experiments were performed for a wide range of probe wavelengths, and all data exhibited qualitatively similar behavior. Figure 8.3 shows the time evolutions of the reflectivity in the pump-beam center at eight different wavelengths in the range 480–730 nm. These measurements were generally recorded on different days, so that systematic variations, for example in terms of slight variations in pump fluence, are possible. Nevertheless, as a general trend we observe that the risetimes of  $R_p$  and  $R_s$  decreases as the probe wavelength increases; the subsequent drop in  $R_p$  is less pronounced at shorter wavelengths; and the steady-state values of  $R_p$ , reached 100–300 fs after excitation, decrease with increasing probe wavelength, whereas  $R_s$  generally increases. (These qualitative observations are quantified in Section 8.A.)

We fitted the dynamic model Eq. (8.2) simultaneously to all the dataserieS shown in Fig. 8.3, where the resulting model predictions are shown as solid lines. To allow for the expected small systematic variations in experimental conditions, we allowed  $n_{1,\infty}$ ,  $n_{2,\infty}$ ,  $t_0$ ,  $\xi$ , and  $\Gamma_{2,0}$  to vary independently between each dataserieS. All the fitted parameters are summarized in Table 8.1

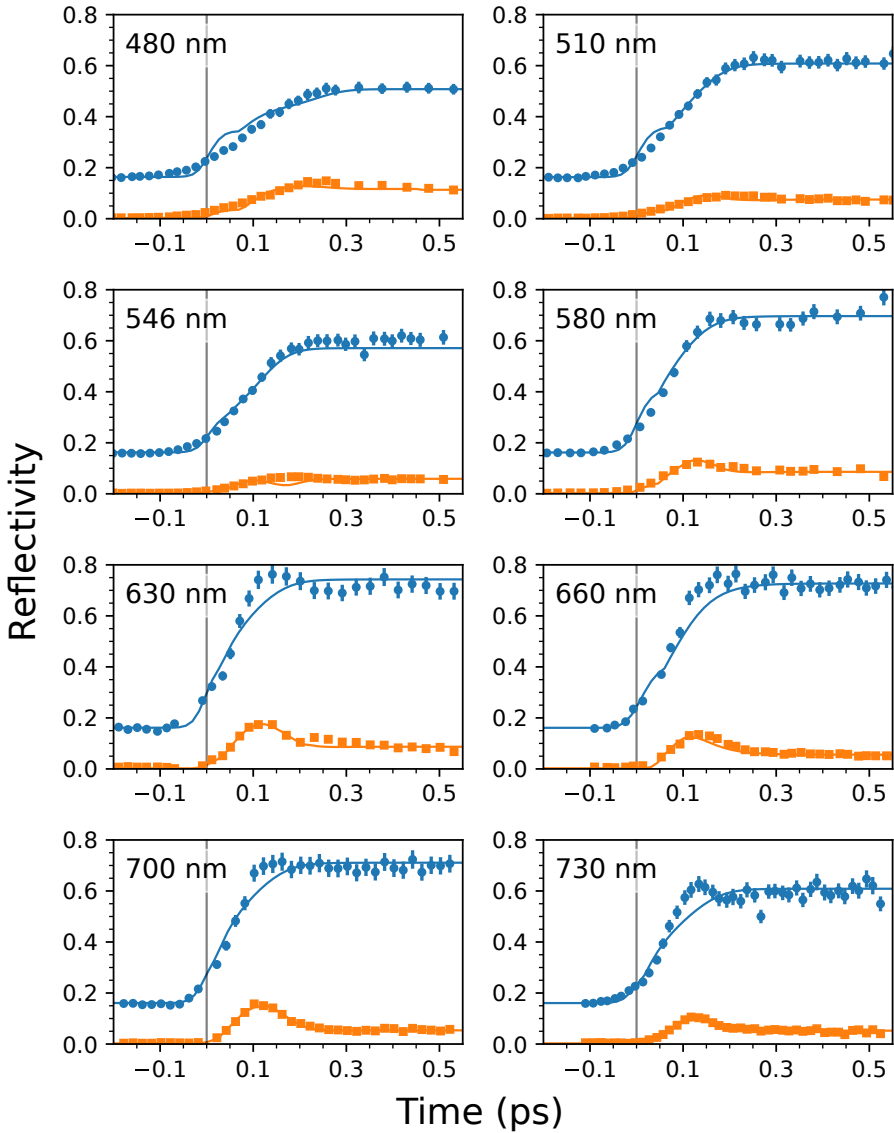


**Figure 8.3:** Observed time-resolved values of  $R_s$  (blue circles) and  $R_p$  (orange squares) at different probe wavelengths. The solid lines are model predictions (c.f. Eq. (8.2)) based on a simultaneous fit across all the displayed datasets. Vertical lines mark  $t = 0$  as inferred from the fit.

**Table 8.1:** Model parameters [c.f. Eq. (8.2)] obtained from fitting the data in Fig. 8.3 with  $\tau_2 = 60$  fs. Parameters that were allowed to change between each of the 8 dataseries are summarized here by the mean  $\pm$  the standard deviation.

Parameter	Value	Units
$n_{1,\infty}$	$(1.9 \pm 0.2) \times 10^{21}$	$\text{cm}^{-3}$
$n_{2,\infty}$	$(3.3 \pm 0.6) \times 10^{22}$	$\text{cm}^{-3}$
$\Gamma_1$	$1.0 \times 10^{14}$	$\text{s}^{-1}$
$\Gamma_{2,0}$	$(4.5 \pm 2.4) \times 10^{15}$	$\text{s}^{-1}$
$\Gamma_{2,\infty}$	$9.2 \times 10^{14}$	$\text{s}^{-1}$
$\ell_1$	43	nm
$\ell_2$	23	nm
$\tau_1$	110	fs
$T$	43	fs
$t_0$	$135 \pm 60$	fs
$\xi$	$45 \pm 21$	fs

with the aforementioned parameters represented by their mean  $\pm$  the standard deviation. (The full set of parameters is presented in Section 8.A.) We see that the model provides a good explanation of most of the observations: pronounced peaks in  $R_p$  (actually caused by the subsequent drop in  $R_p$ ) are produced at longer wavelengths, and the correct steady-state values of  $R_s$  and  $R_p$  are obtained, which was impossible to achieve without accounting for the electron cloud. Even the wavelength-dependent risetimes are qualitatively captured by the Drude model with the simple time-dependent exponential decrease of  $\Gamma_2$ .

The parameters obtained for the excited-carrier density and scattering rate in fused silica compare well with values in the literature [125, 128–130, 132, 134]. The spatial extent of the plasmas are relatively short; inside the dielectric, this is expected due to the small skin depth  $\sim 28$  nm of the e-h plasma, estimated using optical parameters corresponding to the steady-state values at the surface (Table 8.1). The maximum e-h density amounts to about 50% of the (atomic) number density in fused silica ( $6.6 \times 10^{22} \text{ cm}^{-3}$ ). The electron cloud outside the target corresponds to 11% of the total number of excited electrons. As a result, the surface of the dielectric becomes positively charged, which presumably assists with keeping the electron cloud intact. This picture

is in line with the build-up time  $\tau_1 = 110$  fs and delay  $t_0 \simeq 135$  fs relative to the excitation. Note that the electron cloud is much denser than the density of ambient air  $2.7 \times 10^{19} \text{ cm}^{-3}$ , which indicates that the ambient air plays only a minor role, e.g. in confining the plasma.

It is conceivable that the positive surface charge resulting from electron emission may become so large that it initiates Coulomb explosion – removal of surface ions due to mutual electrostatic repulsion [34, 35]. This would, however, severely perturb the system and thus affect the otherwise steady reflectivities, which is incompatible with the present observations. Coulomb explosion is possibly suppressed by partial compensation of the surface charge by electrons originating from deeper within the e-h plasma. Previous studies on fused silica (and similar materials) agree that the reflectivity after strong laser-pulse excitation remains stable for a few ps after which the onset of macroscopic ablation (*not* Coulomb explosion) masks the e-h-optical response [129, 134, 143].

Let us discuss why the specific features of the reflectivity measurements observed here, inexplicable without the additional electron cloud outside the dielectric target, has to our knowledge only been reported a few times before [127, 133]. To this end, we recall that  $R_p$  starts to drop due to destructive interference between reflections from the cloud and the solid only if  $\varepsilon_1(\omega) < \sin^2 \theta$  Section 8.A. Assuming that  $\Gamma_1 \ll \omega$  (see Table 8.1) and making use of Eq. (8.1), the condition can be expressed more clearly in terms of the probe frequency  $\omega$  and the plasma frequency  $\omega_{p,1}$  of the electron cloud:

$$\omega < \omega_{p,1} / \cos \theta. \quad (8.3)$$

When this condition is *not* fulfilled, the  $p$ -reflectivities from the cloud and the solid surface interfere constructively, thereby making  $R_p$  appear indistinguishable from the response of only an e-h plasma. Most previous experiments used a shorter probe wavelength (larger  $\omega$ ), and smaller incidence angles (larger  $\cos \theta$ ), meaning that the condition Eq. (8.3) was not fulfilled at excitations corresponding to ablation.

To the best of our knowledge, the only previous reports of a subsequent drop in  $R_p$  are Refs. [127, 133]. The authors attributed the drop in  $R_p$  to resonance absorption.  $\text{Re}(\varepsilon) = 0$  is not fulfilled in the dilute electron cloud outside the dielectric (see Table 8.1), but the condition *is* fulfilled inside the dielectric. Suppose that  $\text{Re}(\varepsilon_2) = 0$  at a specific critical depth  $z = d$  for a certain probe frequency  $\omega$ . According to Eq. (8.1), reducing  $\omega$  increases  $d$ , because a

smaller  $n_2$  is needed to achieve  $\text{Re}(\epsilon_2) = 0$ . However, the penetration depth of the probe pulse inside the e-h plasma increases with  $\omega$  (skin effect). Therefore, at lower  $\omega$ , a smaller field amplitude passes through  $z = d$ , thus reducing the influence of resonance absorption on  $R_p$ . This is in contradiction with our data: the differences between  $R_s$  and  $R_p$  are larger at longer wavelengths.

In conclusion, we measured transient and polarization-resolved reflectivities of short-laser-pulse-excited fused silica using ultrashort wavelength-tunable probe pulses (480–730 nm). About 100–200 fs after excitation, we observed a drop in the  $p$ -reflectivity, which could not be reproduced by standard optical models based on an air–solid interface. We were able to explain the time-dependent measurements by including the interference effects of reflection from an electron cloud originating from the laser-excited dielectric. A time-dependent scattering rate in the electron-hole plasma inside fused silica explains the slow growth (compared with the pump-pulse duration) of the reflectivities. The experimental conditions under which clear optical signatures of the electron cloud can be seen were discussed. The new understanding of transient optical properties, provided in this letter, potentially opens up a new avenue towards increased control of short-pulse excitation of materials.

**Acknowledgements** We thank Lasse Haahr-Lillevang for his contributions to an early version of this experiment. Innovation Fund Denmark is acknowledged for funding via the SunTune project.

## 8.A Supplemental material

### 8.A.1 Experimental setup

The experimental setup is a typical pump-probe scheme, sketched in Fig. 8.4. The pump and probe pulses derive from a regeneratively amplified Ti:sapphire laser, delivering 35 fs (at FWHM) pulses (1.4 mJ maximum pulse energy at 5 kHz) centered around 800 nm. The laser is gated by our data-acquisition software to fire single pulses on demand. The first beam splitter (BS, Fig. 8.4) placed after the laser separates the laser beam into a pump beam and a probe beam.

The probe is sent through an optical parametric amplifier (TOPAS), outputting wave-length-tunable fs pulses (marked as green in Fig. 8.4). Only probe wavelengths between 480 nm and 730 nm are used here. After the TOPAS, a periscope arrangement rotates the electric-field polarization by roughly  $45^\circ$

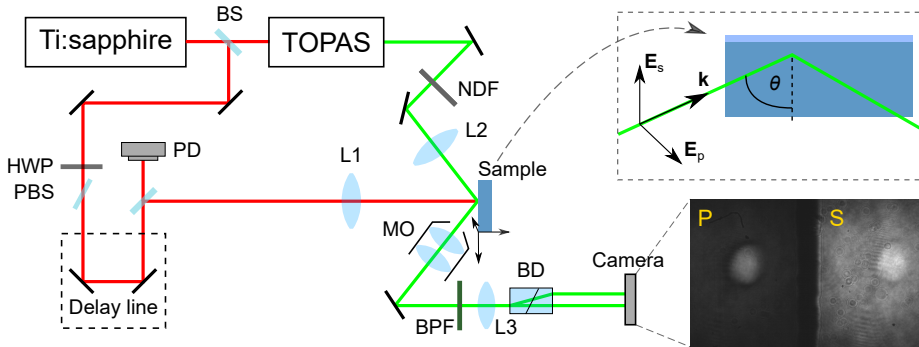


**Figure 8.4:** Pump-probe setup for measuring simultaneously  $s$ - and  $p$ -reflectivities. The pump and probe beam paths are marked by red and green, respectively. The upper right inset shows the probe beam incident onto the sample at an angle  $\theta = 59.5 \pm 1.0^\circ$  of mixed  $s$  (electric field  $E_s$ ) and  $p$  (electric field  $E_p$ ) polarization. A microscope objective (MO) collects the reflected probe and images it onto a camera, and a beam displacer (BD) separates the reflected  $s$  and  $p$  components; an example of a resultant image is shown next to the camera (left:  $p$ , right:  $s$ ). HWP: half-wave plate; BS: beam splitter; PBS: thin-film polarizing beam splitter; PD: photodiode, BPF: bandpass filter; NDF: neutral density filter wheel; L1-L3: 100 mm, 50 mm, and 200 mm achromatic lenses.

such that the probe beam consists of an almost equal mixture of  $p$  and  $s$  components. After passing through an adjustable reflective neutral-density filter wheel (NDF), the probe beam is focused (via the 50 mm achromatic lens L2) onto the sample at an incidence angle  $\theta = 59.5 \pm 1.0^\circ$  (dash-outlined inset in Fig. 8.4). The pulse is imaged onto a CMOS camera (8-bit,  $720 \times 480$  pixels) by a combination of a long-working-distance, infinity-corrected microscope objective (MO) ( $\times 20$ ,  $NA = 0.42$ ) and a 200 mm achromatic tube lens (L3). A band-pass filter (BPF) is placed between MO and L3 to filter out potential stray light from sources other than the probe pulse (e.g. scattered pump light and plasma emission). The birefringent calcite beam displacer (BD) placed after L3 spatially separates the  $p$ - and  $s$ -polarized components on the camera sensor as shown in Fig. 8.4. Two crossed linear polarizing filters (not shown) are mounted in front of the camera sensor to filter out  $s$ -polarized probe light on the  $p$ -side and vice versa.

The pump beam is sent through a computerized mechanical delay line. The pulse energy is adjusted by a combination of a half-wave plate (HWP) on a computerized rotation stage and a thin-film polarizing beam splitter

(PBS), transmitting primarily the  $p$ -polarized component. The pulse energy is monitored by a fast, calibrated photodiode (PD). Finally, the pump beam is focused at normal incidence onto the sample by a 100 mm achromatic lens (L1). The sample is mounted on a computer-controlled three-axis stage, and is moved to a fresh location after each pump pulse. An electro-mechanical shutter is placed in the pump-beam path so that reference images of the sample surface can be captured prior to the actual measurement where both the pump and probe light interact with the sample.

### 8.A.2 Laser pulse parameters

The central part of the pump beam at the sample is described well by an elliptical Gaussian with beam waists (radius at  $1/e^2$  in intensity) around  $30\ \mu\text{m}$  (vertical) and  $23\ \mu\text{m}$  (horizontal), as inferred by the typical approach of measuring the cross sections of ablation craters at various pulse energies [59].

The laser beam exiting the Ti:sapphire laser is intentionally slightly chirped to optimize the output from the TOPAS; the latter requires a compressed pump pulse (FHMW  $\sim 35$  fs) in order to function optimally. The chirp in the pump path is almost compensated for by a beam-size-reducing telescopic arrangement (not shown in Fig. 8.4) and the HWP, because from noncollinear autocorrelation measurements, we find that the pulse duration of the pump is  $35 \pm 2$  fs. The beam path to the autocorrelation setup differs only from the pump-part of the setup (Fig. 8.4) in that the laser beam does not pass through PBS (3.2 mm thick) and L1 (5.5 mm thick), both of which introduces some unwanted group-delay dispersion, which we estimate to broaden the pulse to no more than 46 fs. (There is a weak focusing lens in the autocorrelation setup that actually reduces the relative amount of group delay dispersion, so this estimate provides a reasonable upper limit.)

To estimate the duration of the probe pulse, we measured cross-correlation signals of the pump and signal/idler beams that generate the desired visible probe pulses inside the TOPAS through parametric processes (sum-frequency generation and second harmonic generation). The cross-correlation width (at FWHM) varied somewhat between 60 fs and 75 fs depending on the wavelength. However, the duration of the visible probe pulse is limited by the shortest of the two pulses (pump or signal/idler); most likely the pump with FWHM 35 fs, but certainly less than  $(75\ \text{fs})/\sqrt{2} \approx 50$  fs.

In summary, we expect, at most, a temporal overlap of the pump and probe at the sample surface of around  $\sqrt{46^2 + 50^2}$  fs  $\approx 70$  fs; any observed

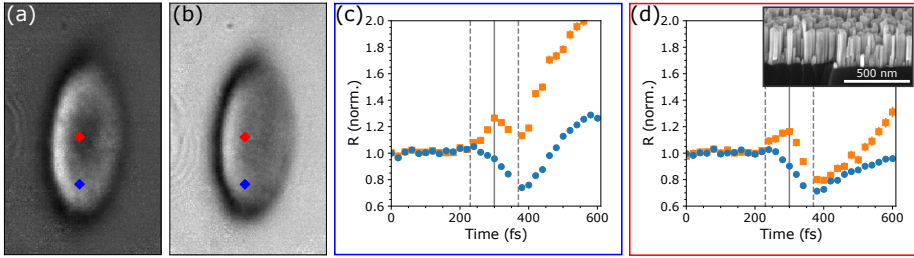


**Figure 8.5:** Time-resolved reflectance measurements of GaN nanowires. Panels (a) and (b): images of the (a)  $p$ - and (b)  $s$ -components of the probe at a certain time delay. The time evolution of the two regions marked by red and blue squares are shown in panels (c) and (d), respectively. Normalized values of the  $p$ - and  $s$ -reflectance are represented, respectively, by blue circles and orange squares. The vertical dashed lines indicate the region of the presumed temporal overlap of the pump and probe pulses. An SEM image of the GaN nanowires is shown in the upper right corner of panel (d).

dynamic changes slower than 70 fs must therefore reflect the response of the target material.

### 8.A.3 Finding $t = 0$

It is important to determine the temporal overlap of the pump and probe pulses (i.e. “ $t = 0$ ”) to correctly interpret the experimental observations. One approach is to take advantage of the instantaneous Kerr effect [130]: the presence of the intense femtosecond pump pulse induces a change in the refractive index of the target, which in turn instantly affects the reflectivity of the probe. It can, however, be difficult to disentangle the Kerr effect from other processes that influence the reflectivity.

We were not able to make this distinction on our fused-silica samples, possibly due to an insufficient dynamic range of the camera (8-bit). Instead we used as a target home-grown gallium nitride (GaN) nanowires (a scanning electron microscope (SEM) image shown in the upper right corner of Fig. 8.5). Fig. 8.5 shows a measurement using a 700 nm probe. Panels (a) and (b) show, respectively,  $s$ - and  $p$ -polarized images at a certain delay. The time evolution of two regions ( $5 \times 5$  pixels), marked red and blue, is followed in panel (c) and (d) wherein blue circles and orange squares represent normalized values of  $s$ - and  $p$ -reflectivities, respectively. The reflectivities initially decrease because the free-carriers reduce the real part of the refractive index. However, a small

peak consistently appears around 300 fs (solid vertical line) in the  $p$ -signal, which we attribute to the temporal overlap of the pump and probe pulses via the Kerr effect. The vertical dashed lines mark a 140 fs interval around the peak, from which we obtain an estimated cross-correlation time (FWHM)  $\sim 70$  fs. This is similar to the overlap estimated in the previous section.

The procedure by which we find  $t = 0$  is as follows: we first perform the desired measurements on the samples of interest (e.g. fused silica) at a specific probe wavelength. Afterwards we switch samples and look for the peak in the  $p$ -reflectance, c.f. Fig. 8.5; this marks  $t = 0$ . Because there are potential alignment issues involved in changing the sample (aggravated by the steep imaging angle), we expect uncertainties in determining  $t = 0$  to be up to  $\pm 120$  fs.

#### 8.A.4 Data analysis

To estimate the change in surface reflectivity induced by the pump at a specific pump-probe delay, two images are captured: First, a reference image  $\mathbf{r} = \{r_{ij}\}$  of the surface without the pump; then an image with pump and probe,  $\mathbf{d} = \{d_{ij}\}$ . The difference between  $\mathbf{d}$  and  $\mathbf{r}$  gives the signal change  $\mathbf{x} = \{x_{ij}\}$  due to the pump excitation, which is proportional to the reflectivity change.

A single picture captured on the camera actually contains two images of the surface acquired with the  $p$ - and  $s$ -polarization of the probe, respectively (see Fig. 8.4). We consider these two images as separate, i.e. the  $p$ -polarized image is  $\mathbf{d}^{(p)} = \{d_{ij}^{(p)}\}$  and the  $s$ -polarized image is  $\mathbf{d}^{(s)} = \{d_{ij}^{(s)}\}$ . We leave out the superscripts indicating the polarization when the formulae apply equally well to both cases.

Because of pulse-to-pulse energy fluctuations of the probe (fluctuations are much more pronounced for the probe because it is generated through nonlinear processes of the pump), we model the data as

$$d_{ij} = a(r_{ij} + x_{ij}), \quad (8.4)$$

where  $a$  is the ratio of the energies of the two subsequent probe pulses. The regions outside the pump-beam-affected zone, where  $x_{ij} = 0$ , are used to estimate the probe-energy ratio  $a$ . Once  $a$  is known,  $x_{ij}$  can be estimated everywhere from Eq. (8.4).

To get absolute reflectivities of the  $p$  and  $s$  components during pump-pulse excitation, we must know the reflectivities of the pristine sample, here denoted

as  $R_{p,0}$  and  $R_{s,0}$ . They are estimated from the Fresnel equations given the known angle of incidence  $\theta \approx 60^\circ$ , and known refractive index of the sample at the probe wavelength. For a particular pixel (suppressing the  $ij$ -indices in the following), the associated reflectivity change is

$$\Delta R_k = \frac{x^{(k)}}{r^{(k)}} R_{0,k} \quad \text{with } k = s, p. \quad (8.5)$$

Because the  $60^\circ$  angle of incidence used in this experiment is close to the Brewster angle of most transparent materials,  $r_p \approx 0$ , which makes Eq. (8.5) useless for estimating  $\Delta R_p$ . Instead, we use the reference image captured on the  $s$ -side of the camera, properly translated and scaled, so that according to Eq. (8.5),

$$\Delta R_p = \gamma \frac{x^{(p)}}{x^{(s)}} \Delta R_s. \quad (8.6)$$

We have introduced the factor  $\gamma$  to correct for the relative pulse energies in the  $s$ - and  $p$ -components of the probe.  $\gamma$  is acquired by calibrating the camera using a high-reflective aluminum mirror.

The absolute reflectivities reported in the letter are obtained as  $R_k = R_{k,0} + \Delta R_k$ .

### A Bayesian probability analysis

The steps outlined fully describes the data analysis procedure: the two crucial steps are the estimation of  $x^{(k)}$  and the proper overlapping of the  $p$ - and  $s$ -polarized sections on the camera. To carry out this procedure automatically and consistently, we apply Bayesian probability theory to estimate  $\mathbf{x}^{(k)}$  and the relative location of the pump beam spots on the  $p$ - and  $s$ -sections on the image to properly overlap them. The workflow is sketched in Fig. 8.6 using the methods described in this section. We assume the reader is familiar with basics Bayesian probability theory, see, e.g. Ref. [144].

In probability theory, Eq. (8.4) is no longer an exact identity but subject to errors (experimental uncertainties), which we account for by adding an error term  $\epsilon$  (suppressing again the  $ij$  indices):

$$d = a(r + x) + \epsilon, \quad (8.7)$$

We assume that the images have been normalized such that  $0 \leq d \leq 1$ . The errors result primarily from shot noise ( $\epsilon \propto \sqrt{d}$ ) since we are concerned with

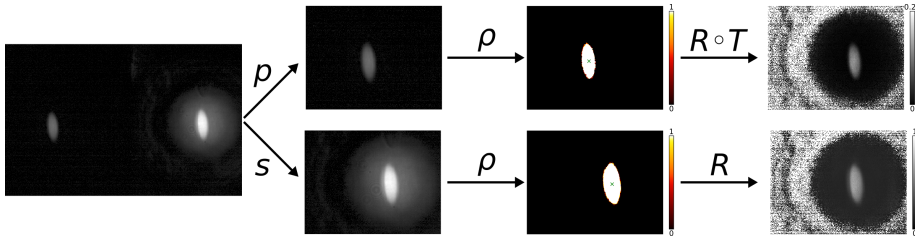


**Figure 8.6:** Principle of the workflow (left to right) for analyzing  $p$ - and  $s$ -reflectivities on fused silica when the reference  $p$ -reflectivity is close zero. The first step is to split the image into the  $p$ - and  $s$ -polarized sections. Then a map  $\rho$  (Eq. (8.26)) is applied separately to each section in order to “threshold” the pump-affected parts of the image (1 is associated with pump-induced signal, 0 with the background). The center of the pump beam is found by computing the center of mass of the thresholded images (marked by green crosses). The  $p$ -polarized image is then translated ( $T$ ) to overlap the pump spot onto the  $s$ -polarized image. Finally, the reflectivity of the  $p$ - and  $s$ -images are computed using Eq. (8.6) and Eq. (8.5), respectively. Note that the regions with low probe signal produce an extreme variance in the reflectivity (because of division by zero), but that is of no concern here, since it is well outside the pump spot.

relatively large changes in reflectivity due to the pump excitation. Consequently, the Poisson-distributed errors can be approximated by a Gaussian with standard error  $\sigma$

$$\Pr(\epsilon|\sigma I) = \frac{1}{\sqrt{2\pi}\sigma} e^{-\epsilon^2/2\sigma^2}. \quad (8.8)$$

In our case,  $\sigma = \frac{c}{\sqrt{255}} \sqrt{d + 0.002}$ , where a choice of  $c$  in the range 0.2 to 0.3 gives a reasonable approximation to the shot noise.<sup>1</sup>

Inspired by [144, pp. 396-403], we adopt a mixture-model approach, where a given pixel is classified according to whether it is outside ( $T$ ) or inside ( $F$ ) the pump spot. In the first case ( $T$ ), we know that  $x \equiv 0$  and therefore  $d = ar + \epsilon$ . In the second case ( $F$ ), Eq. (8.7) holds and  $x$  could be anything in the range from  $-r$  to  $a^{-1} - r$ . We do not immediately know which of the two possibilities is more likely, but suppose that a fraction  $\beta$  of the image is *not* filled by the pump. Randomly drawn pixels from the image thus have a chance  $\beta$  of containing no signal ( $x = 0$ ). Therefore, the likelihood of observing

<sup>1</sup>The seemingly arbitrary factor  $\sqrt{255}$  is introduced because of the 8-bit dynamic range of the camera. Also, the extra term 0.002 ensures that the error remains finite when  $d = 0$ .

datum  $d$ , given  $r$ ,  $a$ , and  $\beta$ , is

$$\Pr(d|ra\beta I) = \beta \Pr(d|raTI) + (1 - \beta) \Pr(d|raFI) \quad (8.9)$$

The likelihood when  $T$  is true is, by virtue of Eqs. (8.7) and (8.8) with  $x = 0$ , the familiar Gaussian likelihood:

$$\Pr(d|raTI) = \frac{1}{\sqrt{2\pi}\sigma} e^{-(d-ar)^2/2\sigma^2}. \quad (8.10)$$

When  $F$  is true, the value of  $x$  could, in principle, be anything in the range noted above. Therefore, we assign a uniform probability over  $x$ :

$$\Pr(x|raFI) = \begin{cases} a^{-1} & \text{if } -r \leq x \leq a^{-1} - r, \\ 0 & \text{otherwise.} \end{cases} \quad (8.11)$$

The likelihood for  $d$  is in this case, without knowing  $x$ :

$$\Pr(d|raFI) = \int dx \Pr(xd|raFI) = \int dx \Pr(x|raFI) \Pr(d|raxFI) \quad (8.12)$$

$$= \frac{1}{2} \operatorname{erf}\left(\frac{d}{\sqrt{2}\sigma}\right) + \frac{1}{2} \operatorname{erf}\left(\frac{1-d}{\sqrt{2}\sigma}\right). \quad (8.13)$$

This specifies the mixture-model likelihood in Eq. (8.9) for a single datum.

Suppose that  $N$  samples have been chosen at random from the image: enumerate them  $i = 1, 2, \dots, N$ . The full likelihood of  $\{d_i\}$  is just a product over the individual likelihood functions for a single datum:

$$\Pr(\{d_i\}|\{r_i\}a\beta I) = \prod_{i=1}^N \{\beta \Pr(d_i|r_i aTI) + (1 - \beta) \Pr(d_i|r_i aFI)\}. \quad (8.14)$$

From this likelihood, we can finally obtain the posterior probability distribution for  $a$  and  $\beta$  through Bayes theorem [144]:

$$\Pr(a\beta|\{d_i\}\{r_i\}I) \propto \Pr(a|I) \Pr(\beta|I) \Pr(\{d_i\}|\{r_i\}a\beta I). \quad (8.15)$$

We have to specify prior distributions for  $a$  and  $\beta$ . For  $a$  we choose a normal distribution for  $a$  centered at 1 (no energy fluctuations) with width around 0.3, whereas for  $\beta$  we assign a beta distribution, which restricts  $\beta$  to the

unit interval, with more weight on large  $\beta$  values. Note, however, that when drawing enough samples (typically we draw  $N = 1000$  samples), the likelihood completely overrules the prior information. Therefore, the choice of priors makes essentially no difference as long as they are consistent with the data.

The most probable values of  $a$  and  $\beta$ , named  $\hat{a}$  and  $\hat{\beta}$  respectively, are found by maximizing either Eq. (8.15) (maximum a posteriori estimation) or Eq. (8.14) (maximum likelihood); if  $N$  is large, the difference is immaterial. In practice, the probability distributions for  $a$  and  $\beta$  are so narrow that the uncertainties they produce in the uncertainty analysis of the reflectivities are negligible compared to the shot noise error  $\sigma$ . We will therefore make the simplifying approximation that  $\Pr(a\beta|\{d_i\}\{r_i\}I) \approx \delta(a - \hat{a})\delta(\beta - \hat{\beta})$ .

To infer the reflectivity, we need the posterior probability distribution for a particular  $x_j$ :

$$\Pr(x_j|\{d_i\}\{r_i\}I) = \int da d\beta \Pr(a\beta|\{d_i\}\{r_i\}I) \Pr(x_j|\{d_i\}\{r_i\}a\beta I) \quad (8.16)$$

$$\approx \int da d\beta \delta(a - \hat{a})\delta(\beta - \hat{\beta}) \Pr(x_j|\{d_i\}\{r_i\}a\beta I) \quad (8.17)$$

$$= \Pr(x_j|\{d_i\}\{r_i\}\hat{a}\hat{\beta}I) = \Pr(x_j|d_j r_j \hat{a} \hat{\beta} I) \quad (8.18)$$

$$\propto \Pr(x_j|a r_j \hat{\beta} I) \Pr(d_j | r_j x_j \hat{a} \hat{\beta} I) \quad (8.19)$$

$$= (1 - \hat{\beta}) \Pr(x_j|a r_j F I) \Pr(d_j | r_j x_j \hat{a} F I) \\ + \hat{\beta} \delta(x_j) \Pr(d_j | r_j \hat{a} T I). \quad (8.20)$$

We see that the probability distribution of  $x_j$  is (within the approximations) a simple average of the product of the likelihoods and priors associated with the two possibilities  $T$  (sample  $j$  outside the pump spot) and  $F$  (inside pump spot), weighted according to  $\hat{\beta}$  and  $1 - \hat{\beta}$ .

Assume that the possibility  $F$  is true – i.e. neglect the second term in Eq. (8.20). In the article (e.g. Fig. 1(d) and Fig. 2), we represent  $x_j$  by its average value  $\bar{x}_j$  with associated errorbars  $\sqrt{x_j^2 - \bar{x}_j^2}$ . The required integrals

can be carried out analytically:

$$\overline{x^n} \equiv \int dx x^n \Pr(x|\{d_i\}\{r_i\}FI) \quad (8.21)$$

$$= \frac{1}{Z} \left( \frac{\sqrt{2}\sigma}{a} \right)^n \sum_{k=0}^n \binom{n}{k} (-1)^k \left( \frac{d-ar}{\sqrt{2}\sigma} \right)^{n-k} (\mathcal{I}_k - \mathcal{J}_k), \quad (8.22)$$

with

$$Z = \sqrt{\pi} \left[ \operatorname{erf} \left( \frac{d}{\sqrt{2}\sigma} \right) + \operatorname{erf} \left( \frac{1-d}{\sqrt{2}\sigma} \right) \right], \quad (8.23)$$

$$\mathcal{I}_k = [1 + (-1)^k] \Gamma \left( \frac{k+1}{2} \right), \quad (8.24)$$

$$\mathcal{J}_k = \Gamma \left( \frac{k+1}{2}; \frac{d^2}{2\sigma^2} \right) + (-1)^k \Gamma \left( \frac{k+1}{2}; \frac{(1-d)^2}{2\sigma^2} \right), \quad (8.25)$$

and  $\Gamma$  is the (incomplete) gamma function.

Finally, it is possible to compute the probability  $\rho$  that a particular sample is within the beam spot. Skipping the details (see [144]) and using the previous approximations,

$$\rho = \frac{(1 - \hat{\beta}) \Pr(d|r \hat{a}FI)}{(1 - \hat{\beta}) \Pr(d|r \hat{a}FI) + \hat{\beta} \Pr(d|r \hat{a}TI)}. \quad (8.26)$$

This is a weighted ratio average of the likelihoods for  $F$  and  $T$ , which certainly makes a lot of sense. We use this equation to threshold the pump spot in the  $p$ - and  $s$ -polarized sections of the images to properly overlap them (see Fig. 8.6).

### 8.A.5 Parameterization of the time-resolved data

The time-resolved reflectivity measurements, displayed in Fig. 1(e) and Fig. 2 in the letter, can be parameterized surprisingly well by the following analytical expressions:

$$R_s(t) \sim R_{s,0} + \frac{1}{2}(R_{s,\infty} - R_{s,0}) \operatorname{erfc} \left[ -\sqrt{4 \ln 2} \frac{(t - t_{0,s})}{\tau_s} \right], \quad (8.27a)$$

$$R_p(t) \sim R_{p,0} + \frac{1}{2}(R_{p,\infty} - R_{p,0}) \operatorname{erfc} \left[ -\sqrt{4 \ln 2} \frac{(t - t_{0,p})}{\tau_p} \right] + \Delta R_p \exp \left[ -4 \ln 2 \frac{(t - t_{0,p})^2}{\tau_p^2} \right]. \quad (8.27b)$$

The initial reflectivities  $R_{k,0}$  ( $k = s, p$ ) are the known reflectivities of the dielectric material;  $R_{k,\infty}$  are the steady-state reflectivities, and  $\tau_k$  are the time constants (FWHM) of the growth of  $R_k$ . The third term in Eq. (8.27b) accounts for the transient peak in  $R_p$ ; note that the time constant is the same as in the second term.

The time-resolved reflectivity data, shown in Fig. 3 in the letter, are fitted to Eq. (8.27) in Fig. 8.7. The associated fitted values of  $R_{k,\infty}$ ,  $\tau_k$ , and  $\Delta R_p$ , are displayed, respectively, in panels (a-c) in Fig. 8.8. These plots substantiate the qualitative remarks made in the letter.

### 8.A.6 Inadequacy of a single dielectric constant

To explain the reflectivity data, it is necessary to reproduce the observed differences between  $R_s$  and  $R_p$ . From Fig. 8.8(a), differences up to 0.65 are seen. However, reflection of a monochromatic beam incident from air at the incidence angle  $\theta \approx 60^\circ$  onto a material with *any* complex dielectric constant  $\varepsilon = \varepsilon' + i\varepsilon''$  cannot produce such large differences. This is illustrated in Fig. 8.9, where we show  $R_s - R_p$  at 700 nm for a wide range of values of  $\varepsilon$ , demonstrating that the maximum reflectivity difference is around 0.5.

In a highly-excited dielectric material, we expect  $\varepsilon'$  to be negative. This further limits the possible values of  $R_s - R_p$ . The laser-excited dielectric should of course not be modeled as a homogeneous material. We have therefore performed several numerical calculations using the Helmholtz equation (see Section 8.A.7) with various plasma decay lengths inside the dielectric using the Drude model. However, none of these were able to reproduce the experimentally observed differences between  $R_s$  and  $R_p$ .

### 8.A.7 Reflectivity calculations

To better describe the experimental results, we introduced a new model. The model geometry was sketched in Fig. 2(a) in the letter, and reproduced here in Fig. 8.10 for convenience. The system consists of two regions (region 1: air, region 2: dielectric target) separated at  $z = 0$ . The incident wave vector lies in the  $xz$  plane, impinging from air towards the target at an incidence angle  $\theta$ :  $\mathbf{k}_{\text{inc}} = (\omega/c)(\mathbf{e}_x \sin \theta + \mathbf{e}_z \cos \theta)$ . We further assume perfect symmetry in the  $xy$  plane, implying that  $k_x = (\omega/c) \sin \theta$  is conserved [? ].

We distinguish between  $s$  and  $p$  polarized waves. For the  $s$  polarization, it is easiest to consider the wave equation for the electric field, which is completely

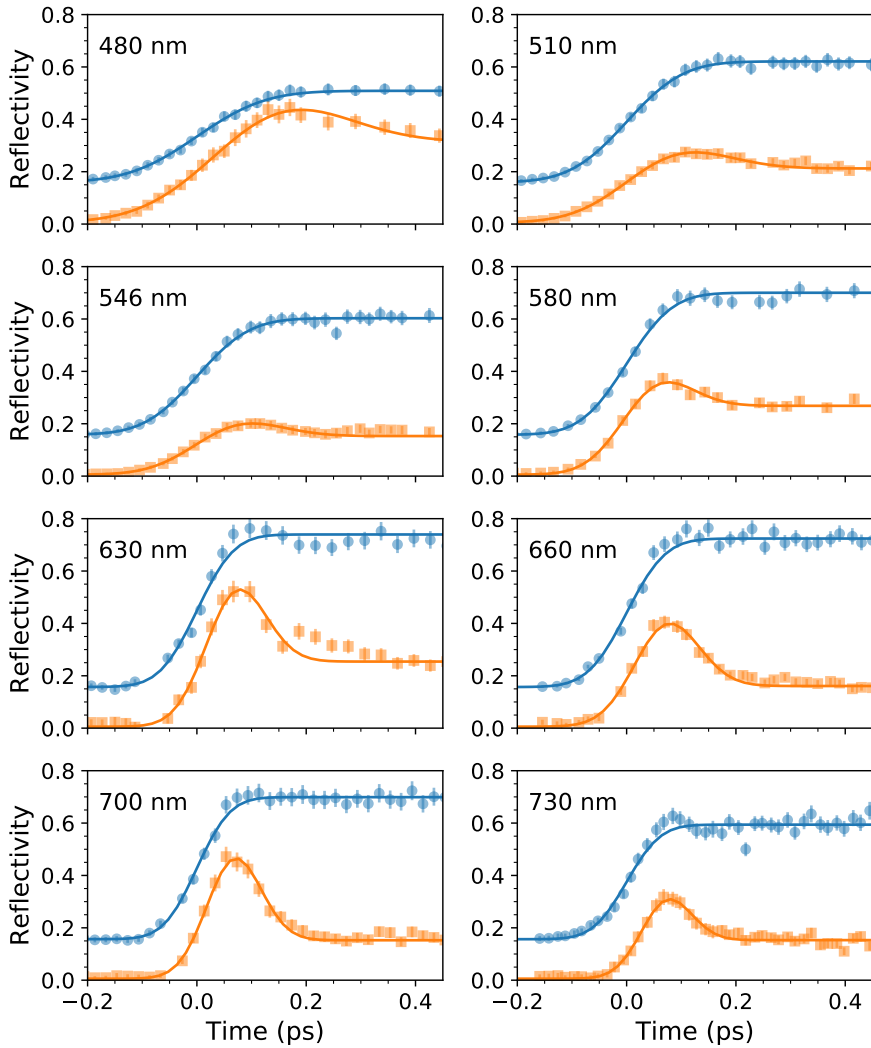


**Figure 8.7:** Time-resolved  $R_s$  (blue circles) and  $R_p$  (orange ) data in the center of the pump beam spot at different probe wavelengths (noted in the top left corner). For clarity,  $R_p$  has been scaled by  $\times 3$ , and the data has been offset in time for ease of comparison. The solid lines are the parameterization via Eq. (8.27).

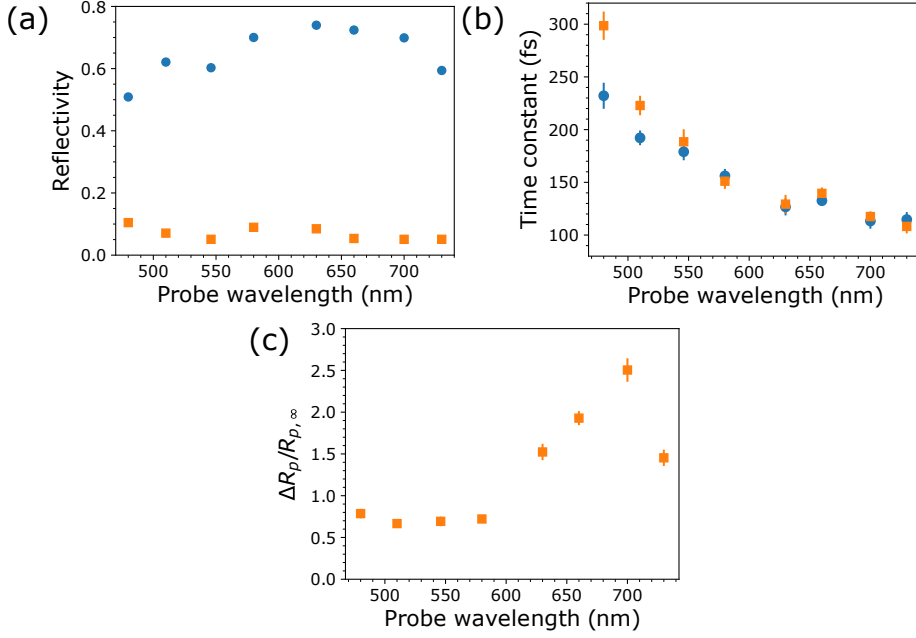


**Figure 8.8:** Model parameters according to Eq. (8.27) and Fig. 8.7. Blue circles and orange squares are associated with Eq. (8.27a) and Eq. (8.27b), respectively. (a) Steady-state reflectivities, (b) time constants, and (c) amplitudes  $\Delta R_p$  of the peak in  $p$ -reflectivity normalized to  $R_{p,\infty}$ .

polarized in  $y$ :

$$E_y'' + \frac{\omega^2}{c^2} (\varepsilon(z) - \sin^2 \theta) E_y = 0. \quad (8.28)$$

The prime denotes differentiation with respect to  $z$ . For the  $p$ -component, we consider the magnetic  $B$  field, which is also  $y$ -polarized; its wave equation reads

$$B_y'' - \frac{\varepsilon'(z)}{\varepsilon(z)} B_y' + \frac{\omega^2}{c^2} (\varepsilon(z) - \sin^2 \theta) B_y = 0. \quad (8.29)$$

The two uncoupled wave equations can now be solved by a procedure analogous to the transfer-matrix method (TMM) [15], where we start with the transmitted field deep inside fused silica in the form  $\sim e^{ik_x x + ik_{z,2} z}$  with  $k_x = (\omega/c) \sin \theta$  and  $k_{z,2} = (\omega/c) (\varepsilon_{b,2} - \sin^2 \theta)^{1/2}$  (this is the solution in the homogeneous material for  $z \gg \ell_2$  where  $\varepsilon_2 \approx \varepsilon_{b,2}$ ) and integrate backwards to some  $z^*$  where  $\varepsilon_2 = 1$  (i.e.  $|z^*| \gg \ell_1$ ). However, the dielectric constant is

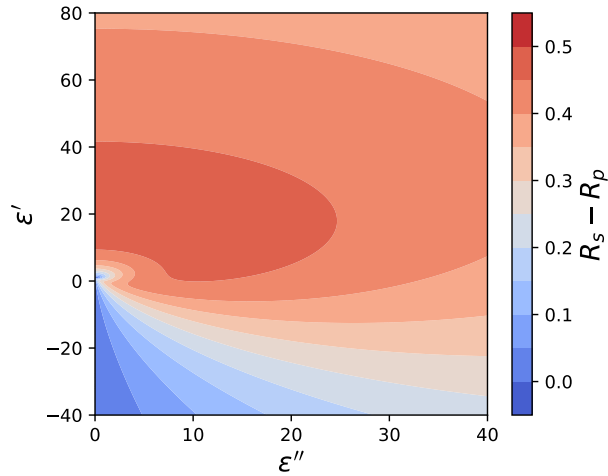


**Figure 8.9:** Differences between  $R_s$  and  $R_p$  reflectivities at the interface between air and a hypothetical material. The reflectivities are computed for 700 nm at an incidence angle of  $60^\circ$  using Fresnel's equation at various values of the real ( $\epsilon'$ ) and imaginary ( $\epsilon''$ ) parts of the material's dielectric constant.

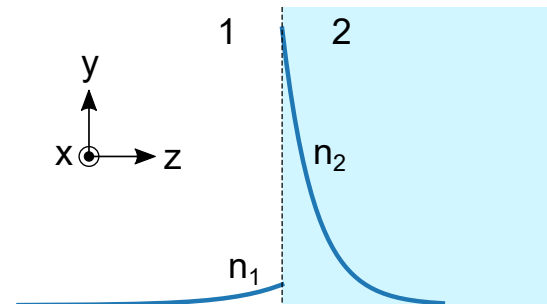


**Figure 8.10:** Model geometry. The interface between the two regions labelled “1” (air) and “2” (dielectric) is placed at  $z = 0$ . The blue solid lines depict the free-carrier densities (labelled  $n_i$ ,  $i = 1, 2$ ) which are assumed to decay exponentially on either side of the interface. The incident waves propagate in the  $xz$  plane.

discontinuous at  $z = 0$ , so the fields must be matched by Maxwell's interface conditions. For example, we require for the  $p$ -polarized field that

$$\begin{aligned} \lim_{z \rightarrow 0^+} B_y(z) &= \lim_{z \rightarrow 0^-} B_y(z), \quad \text{and} \\ \lim_{z \rightarrow 0^+} \frac{1}{\varepsilon(z)} B'_y(z) &= \lim_{z \rightarrow 0^-} \frac{1}{\varepsilon(z)} B'_y(z). \end{aligned} \quad (8.30)$$

This provides the proper initial conditions for the field and its derivative in the second domain (air in this case). The conditions are equivalent for the  $s$ -polarized wave except that  $E'_y$  is continuous.

Continuing the integration to some  $z^*$ , the solution is matched, according to the appropriate interface conditions, to an incident and a reflected plane wave:  $F \sim e^{ik_{z,1}z^*} + r e^{-ik_{z,1}z^*}$ . Here,  $r$  is the complex reflection coefficient, which we can now obtain as follows

$$r_p = \frac{ik_{z,1}B_y^* - B_y'^*}{ik_{z,1}B_y^* + B_y'^*}, \quad r_s = \frac{ik_{z,1}E_y^* - E_y'^*}{ik_{z,1}E_y^* + E_y'^*}, \quad (8.31)$$

where the starred quantities are the (numerically obtained) fields evaluated at  $z^*$ . Finally, the reflectivities are just  $R_p = |r_p|^2$  and  $R_s = |r_s|^2$ .

The differential equations were solved using the `DifferentialEquations.jl` package [145] using non-stiff solvers. We checked that this approach – solving the Helmholtz equations – gives the same reflectivities as using the TMM (with the `tmm` package [100]) where the domain is sliced into many thin layers, each having a constant dielectric constant. For high accuracy calculations, solving the Helmholtz equations with `DifferentialEquations.jl` was more time efficient than using `tmm`, which is why we used the former approach.

### 8.A.8 Fitting of the time-resolved data

The time-resolved data shown in Fig. 2 of the letter were fitted to Eqs. (2) of the letter, which we reproduce here for convenience:

$$n_2(t) = n_{2,\infty} \operatorname{erfc} \left[ -\sqrt{4 \ln 2} \frac{t}{\tau_2} \right], \quad (8.32a)$$

$$n_1(t) = n_{1,\infty} \operatorname{erfc} \left[ -\sqrt{4 \ln 2} \frac{(t - t_0)}{\tau_1} \right] \frac{n_2(t)}{n_{2,\infty}}, \quad (8.32b)$$

$$\Gamma_2(t) = \begin{cases} \Gamma_{2,0} & t < \xi \\ \Gamma_{2,\infty} + (\Gamma_{2,0} - \Gamma_{2,\infty})e^{-(t-\xi)/T} & \xi \leq t \end{cases} \quad (8.32c)$$

All dataseries (i.e.  $R_s$  and  $R_p$  at different time delays acquired for a particular probe wavelength) were combined to form a single likelihood function. The likelihood of each datum was taken as a Gaussian with standard error assigned to the estimated uncertainty on  $x$  (see Section 8.A.4) and on  $R_0$  (the intrinsic reflectivity). Scale-parameters in the model ( $n$ ,  $\Gamma$ ,  $\tau$ ,  $T$ , and  $\ell$ ) were assigned Jeffrey's prior while locations parameter ( $t_0$ ,  $\xi$ ) were assigned uniform probabilities [144]. To account for systematic variations in experimental conditions (e.g. from day to day), we allowed  $n_{i,\infty}$ ,  $\Gamma_{2,0}$ ,  $\xi$ , and  $t_0$  to vary between dataseries. The "best" model parameters were determined from maximum a posteriori estimation. This is an optimization problem with a vast number of parameters (54 in total): we used a particle-swarm algorithm for the optimization [146], but we of course cannot be sure that we found the global optimum.

The "best" parameters were summarized in Table 1 of the letter with the parameters that were allowed to vary between dataseries represented by the sample mean  $\pm$  sample standard deviation. The variation of these parameters are presented in Fig. 8.11.

The parameters at 660 nm seem to break the general trends in the figures, but inspecting the data (e.g. Fig. 8.7), it is not clear why. Possibly the objective function being optimized (the logarithm of the likelihood times the prior probability distribution) was particularly ambiguous for this parameter subset.

### 8.A.9 Condition for the subsequent decrease of $R_p$

The increase and subsequent decrease of  $R_p$  is explained in the letter as a result of destructive interference between reflections from the electron cloud and the solid. A necessary condition for such destructive interference, Eq. (3), was put forth; let us justify this expression here.

We assume that it is possible to represent the optical properties of the electron cloud and the excited dielectric by pseudo-dielectric constants  $\varepsilon_1$  and  $\varepsilon_2$ , respectively. A probe pulse incident from air (angle of incidence  $\theta$ ) is partly reflected by the cloud ( $\varepsilon_1$ ), and partly by the solid ( $\varepsilon_2$ ). The complex reflection amplitudes for the air–cloud and the cloud–solid interfaces ( $r_1$  and

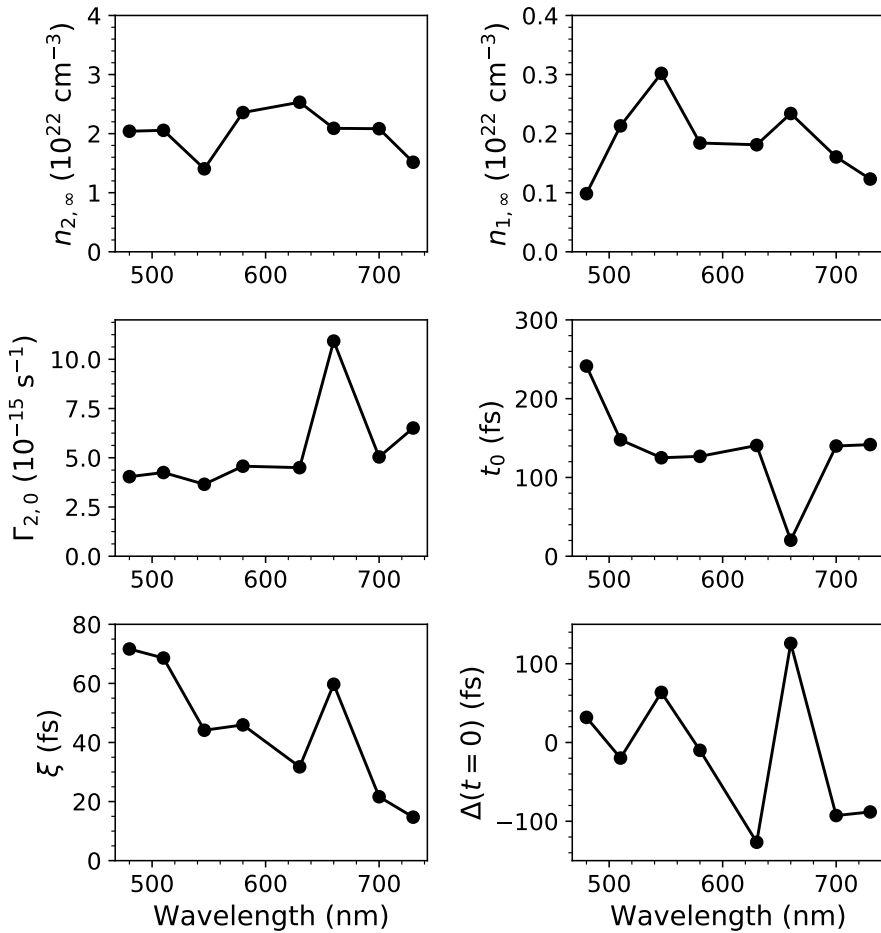


**Figure 8.11:** Inferred wavelength-dependent model parameters from Eq. (8.32). The last panel labelled  $\Delta(t=0)$  shows the difference between the measured  $t=0$  (c.f. Section 8.A.3) and the model's preferred  $t=0$ . Obviously,  $\Delta(t=0)$  fluctuates a lot, but it is actually within the expected uncertainties of the measured  $t=0$ .

$r_2$ , respectively) are [14]:

$$r_1^s = \frac{k_{z,0} - k_{z,1}}{k_{z,0} + k_{z,1}}, \quad r_2^s = \frac{k_{z,1} - k_{z,2}}{k_{z,1} + k_{z,2}}, \quad (8.33a)$$

$$r_1^p = \frac{\varepsilon_1 k_{z,0} - k_{z,1}}{\varepsilon_1 k_{z,0} + k_{z,1}}, \quad r_2^p = \frac{\varepsilon_2 k_{z,1} - \varepsilon_1 k_{z,2}}{\varepsilon_2 k_{z,1} + \varepsilon_1 k_{z,2}}. \quad (8.33b)$$

Here,  $k_{z,i}$  is the component of the wave vector perpendicular to the interfaces in air ( $i = 0$ ), the cloud ( $i = 1$ ), and the solid ( $i = 2$ ).

We expect that the reflection amplitude  $r$  of the entire system is minimal when the relative phase difference between light reflected from the cloud and light reflected from the solid, is approaching  $\pi$ . However, as long as  $k_{z,1}$  is real,  $r_1$  is real and positive; the electron cloud therefore does not introduce a phase shift of the reflected light. This is true regardless of the polarization as long as  $\text{Re}\{\varepsilon_1\} < 1$ , which is always the case according to the Drude description of the optical properties of the cloud.

When  $k_{z,1}$  becomes complex, light reflected from the cloud will exhibit a polarization-dependent phase shift. Since the parallel wave vector  $k_{\parallel} = (\omega/c) \sin \theta$  is conserved (due to symmetry),  $k_{z,1} = (\omega/c) \sqrt{\varepsilon_1 - \sin^2 \theta}$ , which is imaginary when  $\varepsilon_1 < \sin^2 \theta$ . This is thus a *necessary* condition for the occurrence of destructive interference between the reflected beams.

Suppose for simplicity that  $\varepsilon_1$  is real (this is a good approximation, see Table 1 in the letter, which implies that  $\Gamma_1/\omega \ll 1$  for optical frequencies), and  $\varepsilon_1 < \sin^2 \theta$ . According to the Drude model,

$$\varepsilon_1(\omega) \approx 1 - \frac{\omega_{p,1}^2}{\omega^2} < \sin^2 \theta, \quad (8.34)$$

which we solve for  $\omega$  to obtain

$$\omega < \omega_{p,1}/\cos \theta. \quad (8.35)$$

Eq. (8.35) is hence another way to express the necessary condition for the occurrence of destructive interference between reflections from the electron cloud and the solid. The sufficient condition of a significant drop in  $R_p$  is that the relative phase of the two  $p$ -polarized reflections approaches  $\pi$ . This is seen formally from the reflectivity of the full system  $R = |r|^2$ : Let  $d$  be

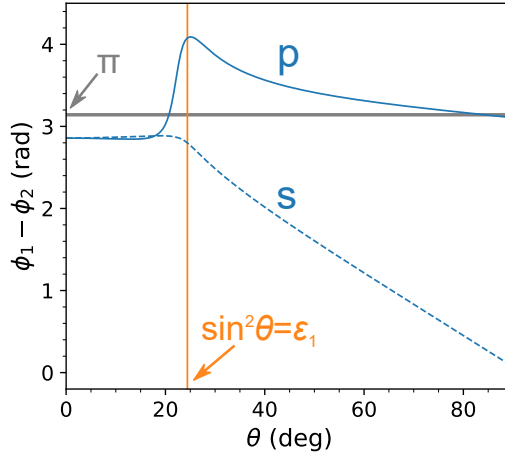


**Figure 8.12:** Phase difference  $\phi_1 - \phi_2$  between 700 nm light reflected from the electron cloud and the solid. Blue lines indicate the values for  $s$ -polarized light (dashed) and  $p$ -polarized light (continuous) as a function of angle of incidence  $\theta$ . The horizontal gray line marks the condition for destructive interference [Eq. (8.37)]. The vertical orange line shows the minimal angle at which  $\epsilon_1 < \sin^2 \theta$  [equivalent to Eq. (8.35)]. For the calculations, we used the dielectric constants of the materials obtained from the steady-state values (at  $z = 0$ ) in Table 1 in the letter.

the thickness of the electron cloud, and define  $\beta = \text{Im}\{k_{z,1}\}d = |k_{z,1}|d$ ; then [147]

$$R = \frac{|r_1|^2 + |r_2|^2 e^{-4\beta} + 2|r_1||r_2|e^{-2\beta} \cos(\phi_1 - \phi_2)}{1 + |r_1|^2|r_2|^2 e^{-4\beta} + 2|r_1||r_2|e^{-2\beta} \cos(\phi_1 + \phi_2)}, \quad (8.36)$$

which is minimal when

$$\phi_1 - \phi_2 = \pi, \quad (8.37)$$

and vanishes if, in addition,

$$|r_1| = |r_2|e^{-2\beta}. \quad (8.38)$$

This expression is valid for both  $s$ - and  $p$ -polarization. Here,  $\phi_i$  is the phase of the reflection amplitude, i.e.  $r_i = |r_i|e^{-i\phi_i}$ , so  $\phi_1 - \phi_2$  is the phase difference between  $r_1$  and  $r_2$ . The Fresnel equations are not easily inverted analytically to determine the conditions that give rise to the phase shift  $\phi_1 - \phi_2 = \pi$ . However, numerical calculations confirm that a phase shift close to  $\pi$  is in fact observed for  $p$ -polarized light under the experimental conditions (using the

typical steady-state values for  $\varepsilon_1$  and  $\varepsilon_2$ , obtained from Table 1 in the letter), while a much smaller phase shift is seen for *s*-polarized light, see Fig. 8.12

---

## TIME-RESOLVED CATHODOLUMINESCENCE OF ERBIUM

This chapter presents some of the work that I carried out on time-resolved cathodoluminescence (CL) during my research stay (February to May, 2018) in Albert Polman's group at AMOLF Amsterdam, The Netherlands.

The goal was to experimentally investigate how a metal nanoparticle influences the spontaneous emission rate of nearby  $\text{Er}^{3+}$  ions on the nanoscale. In SunTune, a localized surface plasmon resonance (LSPR) frequency of the nanoparticles is tuned to approximately match the  ${}^4\text{I}_{15/2} \rightarrow {}^4\text{I}_{13/2}$  transition in  $\text{Er}^{3+}$  (Fig. 1.2) to enhance UC luminescence as explained in Section 1.2. Ideally, the  ${}^4\text{I}_{13/2}$  level should have a long lifetime to promote UC, but interaction with a nearby metal nanoparticle can dramatically reduce this lifetime [16]. The effect is most pronounced in the near-field zone of the nanoparticles, which means that the lifetime modifications cannot be probed through normal means by time-resolved photoluminescence (PL), where the excitation spot is limited by diffraction to a too large area. However, achieving the required spatial resolution *is* possible with a focused electron beam, and the lifetime studies can be carried out using time-resolved CL.

This chapter starts off with a brief description of the physics underlying spontaneous emission-rate modification of emitters by nanoparticles. The

following two sections introduce the basics of CL, and describes the setup developed at AMOLF for time-resolved CL. The experimental investigations are presented and discussed, and we close the chapter with a conclusion and outlook.

## 9.1 Nanoparticle-emitter coupling

### 9.1.1 The Purcell effect

Spontaneous emission is the process where an atom (or more generally, an ion or a molecule) decays to a state of lower energy by emitting a photon without any external stimulus. The rate of spontaneous emission can be estimated from Fermi's golden rule:

$$\Gamma_{2 \rightarrow 1} = \frac{2\pi}{\hbar} |\langle 1 | H_{\text{int}} | 2 \rangle|^2 \rho \quad (9.1)$$

Here,  $|2\rangle$  refers to the excited state and  $|1\rangle$  to a lower-lying energy state (e.g. the ground state). The interaction hamiltonian  $H_{\text{int}}$  couples the two energy states to modes of the quantized electromagnetic field. To compute this rate, we need to add up the probabilities of all the possible paths that lead to the  $2 \rightarrow 1$  transition. Suppose that the emitted photon carries a fixed energy  $\hbar\omega$ ; we must then include all of its possible momentum and polarization states consistent with this energy. The density of states (per unit volume)  $\rho$  accounts for this abundance of possibilities; in free space it reads [14, p. 248]:

$$\rho = \frac{\omega^2}{\pi^2 c^3}. \quad (9.2)$$

E. M. Purcell showed in 1946 that the spontaneous emission rate of nuclear magnetic moments can be modified dramatically by coupling the system to a resonant circuit [148]. The analogy to optics can be made by inserting the atom (emitter) into an imperfect cavity with a linewidth  $\Delta\omega$ . If the resonance frequency of the cavity matches a transition frequency  $\omega$  of the emitter, two modes exist within the cavity for a photon of this frequency (one mode for each of the two orthogonal states of polarizations). The associated density of states per unit volume  $V$  of the cavity is then  $\rho = 2/\Delta\omega V$ . Or, expressed in terms of the *quality factor*  $Q \equiv \omega/\Delta\omega$ ,  $\rho = 2Q/\omega V$  [148]. This is clearly very different from Eq. (9.2). In particular, the explicit dependence on cavity volume makes it possible to significantly modify the spontaneous emission rate of the emitter.

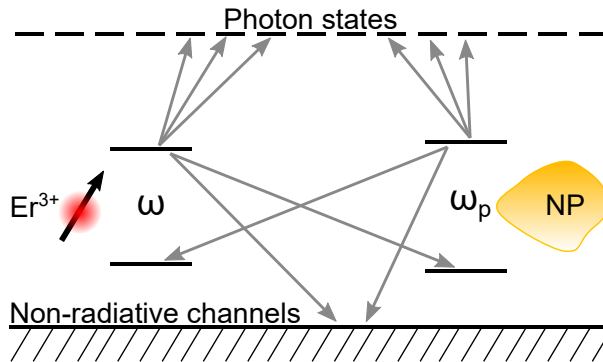


**Figure 9.1:** Couplings (arrows) between the states of an emitter ( $\text{Er}^{3+}$ ), a nanoparticle (NP), free-space photon states, and non-radiative channels (loss). For example, the emitter couples to free-space photon states by spontaneous emission, to the ground state of the nanoparticle by exciting a LSP, or decays via non-radiative channels.

### 9.1.2 Coupling to a plasmonic nanoparticle

A nanoparticle influences the spontaneous emission rate of a nearby emitter in the same way as the cavity in the Purcell effect: by changing the density of optical states at the location of the emitter. This modification can actually be determined classically from the electric fields scattered by the nanoparticle back onto the emitter [14].

A complete picture of the different couplings is presented in Fig. 9.1. An excited-state emitter (here  $\text{Er}^{3+}$ , showing only the two lowest energy levels with transition frequency  $\omega$ ) can decay in the following ways: (i) by emitting a photon to free space (“photon states”); (ii) by coupling to a localized surface plasmon (LSP) in the nearby nanoparticle if  $\omega_p \approx \omega$ , which then decays either nonradiatively or radiatively (to free space); (iii) by radiation and subsequent absorption in the nanoparticle; (iv) and through various non-radiative channels unrelated to the nanoparticle. If the emitter is very close (within a few nm) to the nanoparticle, radiation is usually completely quenched by additional local couplings to the metal [16, p. 202]. Conversely, the emitter can be excited either directly by the incident radiation, or it can be excited by the decay of an LSP of the nanoparticle.

In addition, the nanoparticle may modify the radiative transition rates of the emitter through spatial localization of the electromagnetic near fields. This is understood when we recall that transition rates are typically computed

on the basis of the dipole approximation, which assumes spatially uniform fields across the emitter. This uniformity is broken by the nanoparticle, which potentially enhances the absorption of nearby emitters [16, p. 204]. However, this effect is presumably small for single ions.

Predicting a nanoparticle's influence on the radiative properties of a distribution of emitter is a challenging task. Experimentally, we can compare the decay rates of emitters close to and far away from the nanoparticles; this tells us simply by how much the total decay rate of the emitters was modified by the nanoparticle. It is not revealed whether the decay rate was changed due to radiative or nonradiative (or both) enhancement. If the transition frequency of the emitter does not match a LSP of the nanoparticle, the decay rate can be expected to be enhanced primarily through nonradiative by coupling to ohmic loss in the nanoparticle.

## 9.2 Cathodoluminescence

Cathodoluminescence (CL) is the light emission that results from a target, bombarded with an electron beam (“cathode ray”). The interaction between the swift electrons and the target leads to a multitude of excitations that produces CL. For instance, surface and bulk plasmon modes are easily excited with an electron beam. The reason for this is that a swift electron is essentially a broadband source in frequency space [149] that can simultaneously exchange a wide range of momenta with the target [150]. In contrast, pulsed light sources are rather limited in both frequency and momentum space, which is why they cannot immediately excite surface and bulk plasmons, since energy and momentum cannot simultaneously be conserved.

Following [150], it is useful to distinguish between two types of CL: coherent CL which is dominant in metals (and plasmonic nanoparticles), and incoherent CL which is dominant in semiconductors and dielectrics.

Coherent CL is the radiation which is emitted by charges that are accelerated instantly by the electric field accompanying the incident electron beam. A classical description based on Maxwell's equations quite accurately describes coherent CL by providing the appropriate source terms of an electron moving with constant velocity  $\mathbf{v}$  [i.e. charge density  $-e\delta(\mathbf{r} - \mathbf{v}t)$  and current density  $-e\mathbf{v}\delta(\mathbf{r} - \mathbf{v}t)$ ] [150]. Coherent CL is generally directional (as opposed to “incoherent” luminescence which is typically *Lambertian*); this is easily understood by making the analogy to a driven dipole. An important feature of

coherent CL is that the radiation efficiency increases with the kinetic energy of the incident electrons; the greater velocity increases the magnitude of the radial electric field in direct proportion to the Lorentz factor  $(1 - v^2/c^2)^{-1/2}$  [12, p. 439], thus driving coherently a larger volume of electrons in the target [150].

Incoherent CL resembles PL, where the electron beam transfers the target to some excited state that later relaxes by emitting photons. The process is “incoherent” because the relaxation is delayed, and thus no longer “in tune”, with the excitation source. Typical processes that yield incoherent CL are radiative recombination of electron-hole (e-h) pairs and excitons, and emission from defect states. Another possibility is the excitation of localized luminescent dopants, such as  $\text{Er}^{3+}$ . In contrast to coherent CL, the efficiency of incoherent CL decreases with the kinetic energy of the exciting electron beam. This happens because the inelastic mean free path of electrons in materials generally increases with energy (the “Universal Curve”). In addition, emission of incoherent CL is a random process, so the resulting radiation is often Lambertian. The last property actually makes it possible to distinguish between coherent and incoherent CL [151].

### 9.2.1 Spatial resolution

Most modern SEMs have a spatial resolution around a few nm, which is made possible by the small de Broglie wavelength of energetic electrons. One could think that CL achieves the same resolution, but this is wrong; the electron beam, typically possessing kinetic energies of several keVs, deposits its energy in a pear-shaped volume with a size that increases rapidly with kinetic energy. The interaction volume is exemplified in Fig. 9.2, which shows a CASINO [152] simulation of the energy distribution of electrons from a 10 keV beam in a 300 nm  $\text{TiO}_2:\text{Er}^{3+}$  thin film on top of a silicon substrate. Although the initial beam spot was 5 nm, we see that energy absorption in the sample happens over a much larger volume. Radiation is produced everywhere within this volume, thus reducing the spatial resolution of CL.<sup>1</sup> To improve the spatial resolution, it is a clear advantage to use lower acceleration voltages.

---

<sup>1</sup>Incidentally, the spatial resolution of CL in metals is much better because CL originating within the bulk is absorbed within a skin depth of the metal.

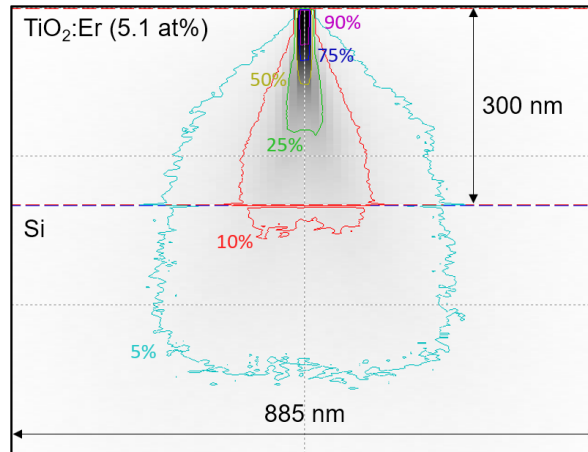


**Figure 9.2:** CASINO simulation of the spatial energy distribution of electrons for a 5 nm wide (radius) 10 keV beam, incident from the top. The contour lines represent the volume within which the kinetic energy of electrons is equal to or larger than X% of 10 keV.

### 9.3 Pulsed CL

The setup for carrying out time-resolved CL is sketched in Fig. 9.3. The source of electrons is a commercial SEM, which has been outfitted with an aluminum-coated parabolic mirror (PM) together with a pair of blanking plates (BP) and a blanking aperture (BA) for pulsing the electron beam.

Electron pulses are created by applying a square-wave AC voltage to the BP using an external frequency generator (typical range  $\pm 5$  V with repetition rates up to 80 MHz). When an electron passes through the biased BPs, its path is deflected slightly sideways in proportion to the applied voltage. The BA blocks any deflected electrons; only electrons that pass through the BP at times when the external bias is zero (when the square-wave signal changes sign) are let through the BA. In this simple way, short (down to ps) electron pulses are generated, and which may consist of less than one electron per pulse (on average). The pulse duration can be adjusted by controlling the distance between the blanking plates and adjusting the acceleration voltage, whereas the beam current determines the average number of electrons per pulse. Running the beam continuously is as simple as disconnecting the external bias on the BPs.

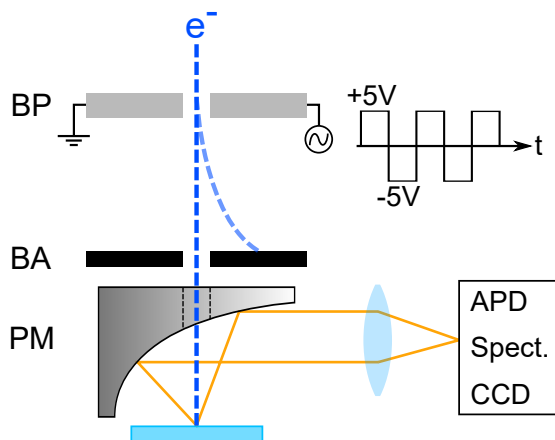


**Figure 9.3:** Schematic setup for pulsed CL. An AC voltage (square-wave signal) is applied to the blanking plates (BP) to deflect the electron beam onto the blanking aperture (BA), thereby pulsing the beam when the applied AC voltage flips sign. The parabolic mirror (PM) collects CL from the sample and directs it onto a CCD, a spectrometer (spect.), or an avalanche photodiode (APD) for time-resolved measurements.

When electrons pass through the BA, they reach the PM through which a small hole is drilled, so that they can reach the sample. When the electrons strike the sample, CL is generated which is collected by the PM and directed outside the SEM chamber where the light enters a commercial CL-optics system (SPARC, Delmic) for analysis. The PM is mounted on a computerized piezo-mechanical stage that is used for aligning the PM, which is crucial for efficient CL collection. The alignment procedure involves gradually moving the sample to the focal plane of the PM, while the CL is imaged onto an external CCD (part of the SPARC system), and aligning the PM to ensure an approximately aberration-free image, that should converge to a small spot when the sample enters the focal plane of the PM.

It is possible in the SPARC system to couple out the collected CL to external optical setups via fibers. For near-infrared CL, we used an external nitrogen-cooled CCD spectrometer (“Spect.” in figure 9.3). Lifetime CL measurements were carried out using a single-photon avalanche diode (“APD” in Fig. 9.3). The APD is connected to a commercial time-correlated single-photon counting system (PicoHarp) which is triggered by short electrical pulses (NIM signal) derived from a trigger-delay generator (TDG) that in

turn is triggered by the external frequency generator that pulses the electron beam. The PicoHarp system bins the arrival times of single-photon events with respect to electron pulses such that a histogram of photon-arrival times is gradually built up. The time resolution can be as good as 70 ps.

CL measurements are acquired using the open-source software “Odemis” (developed by Delmic), which takes control over the scanning of the electron-beam, which is normally handled by the SEM software. However, SEM images are acquired as usual by collection of secondary electrons emitted from the sample. In this way, all CL measurements (whether it is time-resolved lifetime or spectroscopy measurements) are automatically associated with the electron beam’s position and thereby the resulting secondary-electron image acquired by the SEM.

### 9.3.1 Difficulties related to beam blanking

One advantage of using the beam-blanking setup in Fig. 9.3 is that it is possible to easily adjust the repetition rate of the beam, the number of electrons per pulse, and the pulse duration. In another approach, which is also used at AMOLF, but in a different CL setup, electron pulses are generated by shining short focused UV pulses onto the electron gun.<sup>2</sup> For short pulses, this requires a fs laser system (and harmonic-generation stages) that has to be aligned with the SEM. In comparison, the beam-blanking scheme is simpler to implement.

A disadvantage of the beam-blanking approach is, however, that the electron beam is swept across the sample, even when the beam is idle, i.e. when it is not scanning. This effect is more pronounced at lower acceleration voltages, which quickly deteriorates spatial resolution. To correct for this, it is crucial to adjust the lens alignment in the SEM column such that the blanking plates (BP, see Fig. 9.3) are *imaged* onto the sample surface. This imaging configuration is called conjugate blanking [154].

Unfortunately, SEMs are typically not optimized for the conjugate-blanking configuration. As a result, it can be difficult – in fact impossible – to achieve good, aberration-free images. The difficulties increase drastically as the acceleration voltage of the electron beam is lowered [153]. An example of a decent SEM image captured during conjugate blanking at 5 keV is shown in Fig. 9.4, where it is compared to an image taken prior to blanking the beam. The conjugate blanking clearly limits spatial resolution. The situation

---

<sup>2</sup>This setup is described in [153].

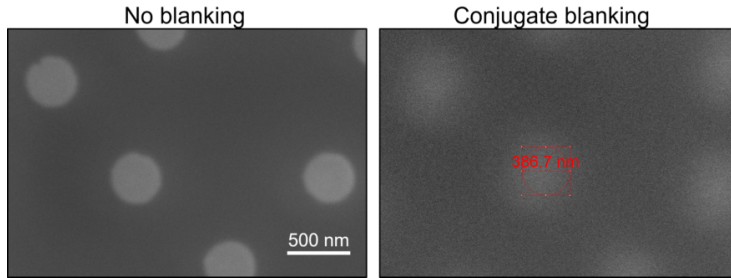


**Figure 9.4:** SEM image of nanoparticles (about 400 nm in diameter) acquired at 5 keV with (right) and without (left) blanking the beam. There is evidently a loss in spatial resolution during beam blanking.

is actually much better at 10 keV and above, but then the spatial resolution of CL is reduced by the much-increased interaction volume (c.f. Fig. 9.2). The spatial SEM resolution using the beam blanker is quantified in [153].

## 9.4 Experimental investigations

The chief aim of the following experimental investigations was to use pulsed CL to map out the decay rate of erbium ions as a function of their distance to a plasmonic nanoparticle. As discussed in Section 9.1, the decay rate of erbium is expected to be modified due to quenching of radiation and resonant coupling to the nanoparticle. Investigating the decay-rate modification of the  $^4I_{13/2}$  level in erbium would be ideal for SunTune, as quenching of this level could severely limit the plasmonically enhanced UC efficiency. However, it was not immediately possible to measure lifetimes at this transition because the spectral response of the APDs used for the decay-rate measurements were limited to optical frequencies. Since radiative quenching by metal nanoparticles anyway happens for all wavelengths, I therefore studied the visible transitions in erbium instead.

The samples that were used in the investigations was brought to AMOLF from Aarhus and consisted of  $TiO_2$  films doped with erbium (5.1 atomic percent), deposited by rf-magnetron sputtering on silicon and quartz substrates by the usual procedures used in SunTune [45]. EBL-produced plasmonic nanoparticles were placed on top of some of the quartz-substrate samples, covering a small fraction of the total surface area. Charging of the quartz

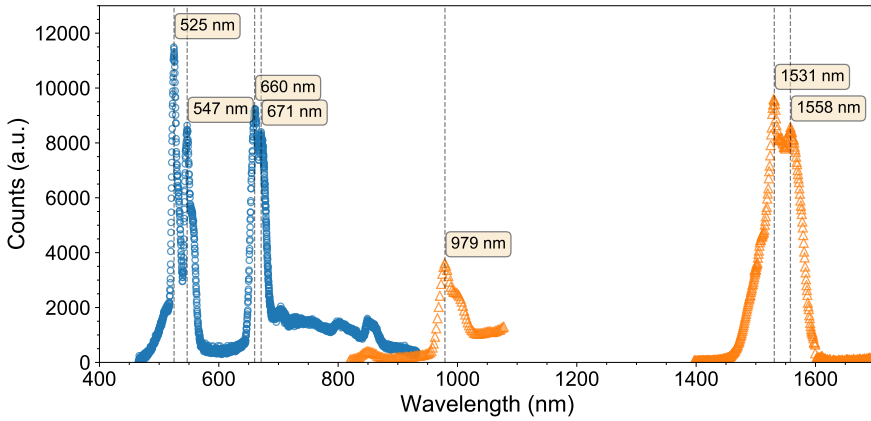


**Figure 9.5:** CL from a 300 nm erbium-doped  $\text{TiO}_2$ -film on silicon. All annotated peaks are characteristic transitions in erbium. Data marked by blue circles and orange triangles were acquired with a VIS and NIR spectrometer, respectively. The electron beam kinetic energy was 30 keV. The peaks are embedded in a background from  $\text{TiO}_2$  and Si.

samples by the electron beam was prevented by coating the upper  $\text{TiO}_2:\text{Er}^{3+}$  film with a thin (1-3 nm) layer of chromium.

#### 9.4.1 Spectroscopy of erbium

As a first step, we confirmed that spectral CL of  $\text{Er}^{3+}$  fits with what is known in the literature as this is typically based on PL. Spectral CL measurements with a 30 keV beam on a sample of 300 nm thick  $\text{TiO}_2$ -doped  $\text{Er}^{3+}$  is shown Fig. 9.5; it indeed confirms that  $\text{Er}^{3+}$  emits CL at all the expected wavelengths (compare to Fig. 1.2). Some side peaks are seen due to crystal-field splitting by the  $\text{TiO}_2$  matrix.

Although the heights and areas of the different peaks in Fig. 9.5 cannot be compared directly to each other, we see that the electron beam promotes  $\text{Er}^{3+}$  ions to basically all of their excited states (at least up to the  ${}^2\text{H}_{11/2}$  level, which emits at the shortest wavelength (525 nm) we could measure). The excitation mechanism of CL can be understood as impact excitation of  $\text{Er}^{3+}$  by hot electrons and holes, created by the electron beam, although Auger-recombination of e-h pairs could also be a possibility [155]. This mechanism

should be contrasted with PL, where erbium ions are excited to a specific level, relax through lower-lying energy states, and are only promoted to states of higher energy through UC-related processes.

### 9.4.2 Time-resolved CL and PL of erbium

The characteristic spacing between erbium ions in the  $\text{TiO}_2$  matrix is 6 Å [156], which implies strong coupling between erbium ions. Since the electron beam excites  $\text{Er}^{3+}$  to all possible energy states, it is possible that resonant energy transfer between the ions could result in different decay dynamics of  $\text{Er}^{3+}$  in CL and PL. Therefore, we wanted to compare the decay rates obtained from time-resolved CL and PL.

For these measurements, we focused on the two transitions around  ${}^2\text{H}_{11/2}$  (525 nm) and  ${}^4\text{S}_{3/2}$  (550 nm), using the pulsed CL setup described above. A band-pass filter ( $550 \pm 40$  nm) was placed before the APD to filter out CL beyond the range of these two erbium transitions. We used 5 keV and 10 keV electron beams, where the background CL from  $\text{TiO}_2$  and Si is negligible.

The choice of repetition rate of the electron pulses basically sets the lower limit on the obtained lifetimes, as the rate has to be sufficiently small to allow relaxation of the ions to the ground state between pulses. Another thing to keep in mind is that, as a general rule of thumb, the count rate on the APD (subtracting dark counts) should not exceed 1% of the repetition rate of the excitation source. We made sure that the count rates were well below this limit.

The time-resolved CL measurement shown in Fig. 9.6 was acquired on the same  $\text{TiO}_2:\text{Er}^{3+}/\text{Si}$  sample as before. The electron-beam energy in the present measurement was 10 keV, the repetition rate was 500 kHz, and the time resolution was 512 ps. The electron current and aperture settings in the SEM were adjusted such that each pulse contained about 0.7 electrons on average with a pulse duration of 70 ps.<sup>3</sup> The decay trace was accumulated over 13 hours.

---

<sup>3</sup>The electron-pulse duration  $\tau$  and the number of electrons per pulse  $n$  are inferred from beam-current measurements using a Faraday cup. Suppose the beam is blanked with a frequency  $f$ , and that the corresponding current collected by the Faraday cup is  $I_f$ . By definition  $I_f = enf$ , which provides  $n$ . If the current is  $I$  without blanking the beam, then  $I\tau = I_f/f$  from which we obtain  $\tau$ .

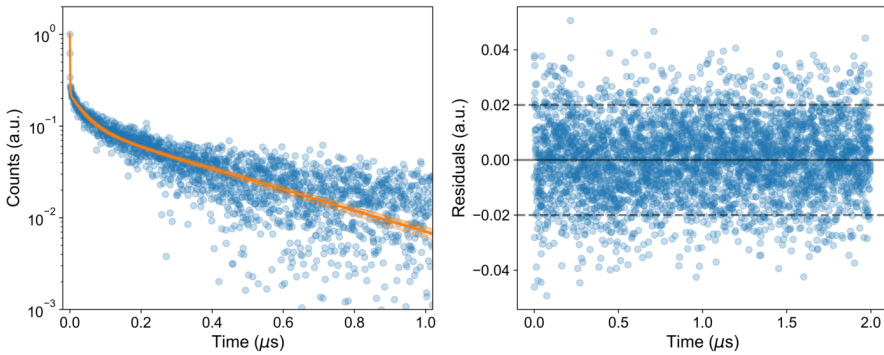


**Figure 9.6:** CL-lifetime measurement of the  ${}^2\text{H}_{11/2}$  and  ${}^4\text{S}_{3/2}$  transitions in  $\text{Er}^{3+}$ -doped  $\text{TiO}_2$ . *Left.* The decay trace; blue points are the data, and the orange solid line is a three-decay-component-exponential fit, Eq. (9.3). *Right.* The associated residuals.

In order to model the data, it is necessary to use a triple-exponential decay function:

$$s(t) = \sum_{i=1}^3 A_i e^{-t/\tau_i}. \quad (9.3)$$

Here,  $s$  denotes the CL signal,  $A_i$  are the amplitudes of each decay component, and  $\tau_i$  are the associated lifetimes (inverse decay rates).

The fitted model is shown as the solid line in Fig. 9.6. The associated residuals, being randomly distributed about 0, indicates that the model provides an adequate description of the data. The model parameters were estimated following the procedure in [157] where the likelihood  $L$  of the data  $\mathbf{d} = \{d_i\}$  is assigned a Student's  $t$ -distribution:

$$L(\mathbf{d}) \propto \left\{ \frac{1}{2} \sum_{i=1}^N [d_i - n(t_i)]^2 \right\}^{-N/2}. \quad (9.4)$$

This choice of likelihood is favored over a Gaussian (i.e. “least squares”) when the experimental uncertainty of each datum is assumed to be the same, but unknown. The resulting parameter estimates with associated  $1\sigma$  uncertainties of the lifetimes are shown in Table 9.1 together with a CL lifetime measurement at 5 keV. Note that the initial fast decay in Fig. 9.6, associated with  $\tau_1$ , basically matches the time resolution in the measurements; its inferred value is clearly more uncertain than let on by the parameter-estimation procedure.

**Table 9.1:** Parameter estimates of the three-component exponential model [Eq. (9.3)] based on time-resolved CL and PL measurements. The lifetime estimates are reported as the mean value  $\pm$  one standard deviation.

	CL		PL 343 nm		PL 515 nm	
	5 keV	10 keV	7 mW	15 mW	16 mW	32 mW
$\tau_1$ (ns)	$0.92 \pm 0.07$	$0.66 \pm 0.03$	$2.07 \pm 0.07$	$1.7 \pm 0.1$	$1.8 \pm 0.6$	$0.71 \pm 0.06$
$\tau_2$ (ns)	$33 \pm 6$	$44 \pm 4$	$29 \pm 3$	$22 \pm 2$	$35 \pm 9$	$35 \pm 4$
$\tau_3$ (ns)	$360 \pm 25$	$379 \pm 12$	$414 \pm 7$	$407 \pm 5$	$447 \pm 6$	$447 \pm 3$
$A_1$	0.88	0.78	0.53	0.38	0.34	0.47
$A_2$	0.10	0.12	0.08	0.12	0.13	0.11
$A_3$	0.08	0.10	0.39	0.50	0.53	0.42

For the PL measurements, we used as the excitation source the second harmonic (515 nm) and third harmonic (343 nm) of a 1030 nm, 500 fs mode-locked fiber-laser. The PL data was likewise modeled by Eq. (9.3), and we repeated the measurements at two different laser-pulse energies (powers). The obtained model parameters are listed in Table 9.1.

We note that the decay dynamics of erbium are not described by a simple, single exponential decay. The reason for this may be related to different classes of  $\text{Er}^{3+}$  inhabiting different local environments [156, 158], which in general affects both the radiative and nonradiative decay rates.

We observe that the lifetimes of the  ${}^2\text{H}_{11/2}$  and  ${}^4\text{S}_{3/2}$  levels obtained by different means (CL and PL at different excitation wavelengths) differ slightly from each other, but that the PL lifetimes obtained at the same wavelength and different laser-pulse energies (powers), and CL lifetimes obtained at different electron-beam energies, mutually agree. Perhaps the lifetimes of  $\text{Er}^{3+}$  show large-scale variations within the sample? Since different areas of the sample was excited in each of the three cases, this provides a simple explanation for the slight variations. That is, the slight differences seem to be “random”, and the variations in Table 9.1 could provide a more realistic picture of the variability of the lifetimes of the  ${}^2\text{H}_{11/2}$  and  ${}^4\text{S}_{3/2}$  transitions in the  $\text{TiO}_2:\text{Er}^{3+}$  sample.

### 9.4.3 Lifetime mapping of erbium

We have confirmed that CL and PL agree on the lifetimes of  $\text{Er}^{3+}$ , so we can use CL to make detailed spatial maps of the lifetimes  $\text{Er}^{3+}$  around plasmonic nanoparticles. For this to be doable, it is important to minimize the time

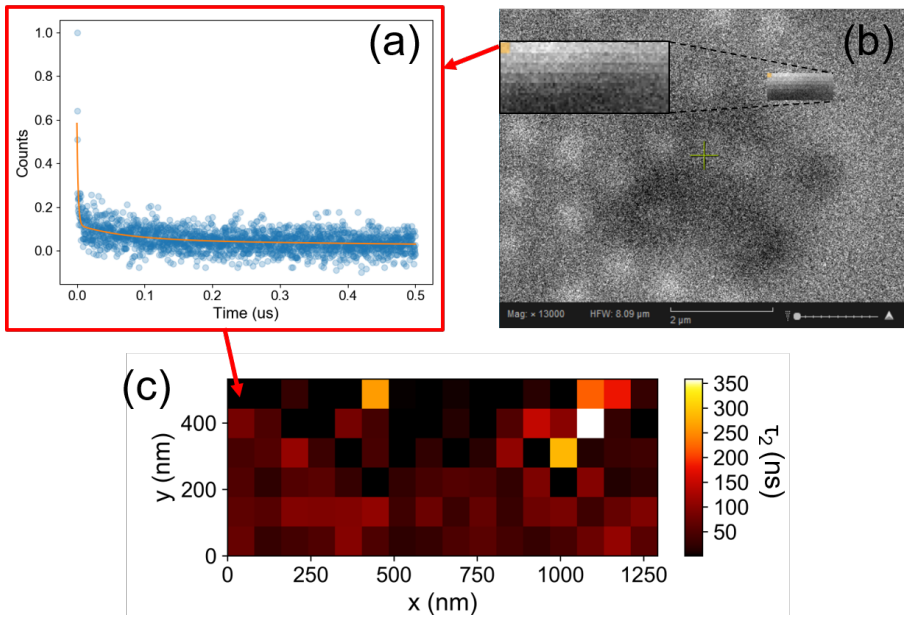


**Figure 9.7:** Lifetime-mapping of erbium close to a nanoparticle. (a) Time-resolved CL at one particular location (indicated by the red arrow). (b) SEM image of the sample during the measurements. The highlighted rectangle is the scan area of the lifetime mapping. (c) Extracted lifetimes  $\tau_2$ , which is correlated to the area in panel (b). The mean estimated  $1\sigma$  uncertainties of  $\tau_2$  is about 60 ns.

needed to obtain an adequate decay trace; after some experimentation with high beam currents and low acceleration voltages, I found that 5 minutes was sufficient to consistently measure the two longer lifetimes  $\tau_2$  and  $\tau_3$ .

The  $\text{TiO}_2:\text{Er}^{3+}$  samples containing nanoparticles, used quartz as a substrate. While we could avoid charging by coating the samples with a thin chromium layer, as explained previously, quartz emits an impressive, and spectrally broad, amount of CL. On these samples, there was basically no CL from quartz at 5 keV, but at 10 keV, the erbium signal was being completely drowned in CL originating from the substrate. Thus 5 keV was used.

The most successful of the measurements is shown in Fig. 9.7. The nanoparticles on this sample is the same gold nanodisks (400 nm diameter and 50 nm in height) shown in Fig. 9.4. The blanked electron beam contained roughly 12 electrons per pulse with a pulse duration around 300 ps.

Panel (b) shows an SEM image acquired during the scan. The darkened

areas are the results of previous electron-beam exposure. The outlined rectangle is the actual region over which the beam was scanned during the lifetime-measurement; it consists of  $17 \times 7$  pixels, i.e. 119 measurements at separate locations. The brightness of each pixel corresponds to the average amount of collected secondary electrons during the roughly 5 minutes measurement. The upper part of the region actually contains about half of a nanoparticle (visible as the brighter the pixels), however it is blurred somewhat, presumably because of slight sample drift over the course of the 10 hours it took to complete the measurement.

Panel (a) shows a decay-time trace associated with the pixel in the upper-left corner. The data is as usual modeled by the triple-exponential-decay function, Eq. (9.3). The spatial lifetime map of  $\tau_2$  is depicted in panel (c), and we should note that the estimated average  $1\sigma$  uncertainty is about 60 ns. There certainly is a trend where  $\tau_2$  is reduced by a factor 4–6 in the vicinity of the nanoparticle, however a precise spatial correlation with the SEM image is clearly not possible.  $\tau_1$  and  $\tau_3$  was also obtained from the fit, but  $\tau_1$  showed no variations (the temporal resolution is anyway not good enough), and  $\tau_3$  was extremely noisy. The latter is presumably a consequence of the rather high repetition rate (2 MHz) used for this measurement, which is on the limits of the typical values of  $\tau_3$  (c.f. Table 9.1).

## 9.5 Discussion and conclusion

Achieving decent lifetime maps of erbium was challenged by the complicated lifetime dynamics of the  $^4S_{3/2}$  level in erbium, which made it difficult to properly analyze the decay traces with a low signal-to-noise ratio, especially because the initial fast decay component dominated the time-resolved CL signal (c.f.  $A_1$  in Table 9.1). We speculated that the complicated decay dynamics was a consequence of *concentration quenching*, where energy is transferred between erbium ions, eventually ending up on a quenching center. The energy-transfer rate could be large due to the high erbium concentration. After I returned from AMOLF, I fabricated several samples erbium-doped  $TiO_2$  with erbium concentrations between 0.1-1.3 at%. I measured the lifetimes of the  $^4S_{3/2}$  and  $^4F_{9/2}$  levels by time-resolved PL (pumping the  $^2H_{11/2}$  with 530 nm), but I still found it necessary to use either two or three (usually the latter) decay components to fit the data. The new lifetimes were, however, larger – ranging from 100 ns to 10  $\mu$ s. This is unfortunately not an advantage for

time-resolved CL measurements, as the reduced erbium concentration and the longer lifetimes would lead to longer measurement times. At this point, we finally realized that erbium-doped TiO<sub>2</sub> was probably not the right material for making these spatial lifetime map.

In a recent paper [159], a group from Delft managed in a well-thought-out experiment to spatially map the decay-rate modifications of cerium ions (Ce<sup>3+</sup>, doped into a YAG (yttrium aluminum garnet) matrix) inside metal-dielectric cavities using time-resolved CL (using the beam-blanking technique that we have also used). Ce<sup>3+</sup> showed, on the relevant time scales, single-exponential decays with typical lifetimes around 100 ns. In [159], a decent decay-time trace was obtained in 8 s per pixel using a repetition rate of 1 MHz. For comparison, our measurements with Er<sup>3+</sup> took about 200 times longer to complete per pixel, and with poor statistics.

To conclude, we performed time-resolved CL measurements on erbium-doped TiO<sub>2</sub> films and measured lifetimes of the <sup>2</sup>H<sub>11/2</sub> (525 nm) and <sup>4</sup>S<sub>3/2</sub> (550 nm) transitions of Er<sup>3+</sup>. The decay of these transitions showed two decay components with lifetimes around 30 ns and 400 ns, following an initial very fast decay with sub-ns lifetime. We observed the same decay dynamics of Er<sup>3+</sup> with time-resolved PL. Spatial lifetime mapping of erbium around gold nanodisks was carried out, but with limited success due to the complicated decay dynamics and a low signal-to-noise ratio. We discussed that the TiO<sub>2</sub>:Er<sup>3+</sup> system is not well-suited for these kinds of measurements.

## CONCLUSION AND OUTLOOK

The SunTune project strives to reduce band-gap losses of solar cells by photon upconversion (UC), photon downshifting (DS), and plasmonics. In UC, two sub-band-gap photons are combined to one photon of higher energy, which can be absorbed by most solar cells. DS provides more low-energy photons for the UC process. Plasmonics is crucial for ensuring efficient UC. Detailed numerical simulations and topology optimization (TopOpt) have been applied to search for excellent UC-enhancing gold nanostructures.

A key theme of this thesis has been the development of an experimental technique for carrying out detailed experimental validations of electric-field simulations of metal nanostructures. This was achieved by utilizing ultra-short laser pulses to induce various modifications, which exhibit well-defined laser-fluence thresholds, in materials surrounding the nanostructures. Such a material, when irradiated below the threshold, is not modified by the laser pulse, but the presence of a nanostructure *can* modify the material by increasing the local fluence above the threshold via near-field enhancement (NFE). The modifications induced by the nanostructures can be accurately imaged with scanning electron microscopy (SEM) and atomic force microscopy (AFM). We have demonstrated that a careful determination of threshold fluences allow lines and surfaces of constant NFEs to be mapped out, enabling direct and quantitative comparison with electric-field simulations.

Two candidates for the laser-induced modification were considered. In the first approach, NFEs of nanoparticles were marked by ablation in an underlying  $\text{TiO}_2$  film. Comparison with numerical simulations were semi-quantitative: The experimental and simulated NFEs generally agreed, but slight systematic differences in the near-field patterns were observed. We argued that the differences might be related to the hot-carrier transport preceding ablation, which was not accounted for by the simulations. The necessity of accounting for such effects suggests a new approach towards precise examination these transport effects on the nanoscale.

In the second approach, we utilized multiphoton polymerization (MPP) of SU-8. Here, nanoparticles were embedded in SU-8, which polymerizes by laser irradiation above a certain exposure threshold. 2D maps of NFEs obtained by SEM agreed well with near-field simulations. We showed that surfaces of constant NFE can, in principle, be obtained via AFM, but consistent results were hard to obtain. Various reasons for this was discussed, and future investigations on periodic TopOpt designs will likely ascertain which ones are correct.

A somewhat different study emerged from our initial investigations on the phase-change material  $\text{Ge}_2\text{Sb}_2\text{Te}_5$  (GST) as a tool for near-field marking. We investigated laser-induced amorphization and ablation of GST as a function of film thickness. A strong thickness dependence of the amorphization threshold, and the appearance of an additional high-fluence ablation threshold in thick films, were observed. By combining SEM and transmission electron microscopy (TEM), we could connect the onset of amorphization to the requirement of complete melting of the film. This condition, together with two-temperature model calculations, confirmed the strong thickness dependence of the amorphization threshold. Concerning ablation, we found, based on TEM, detailed evidence of photomechanical spallation at low fluences. The high-fluence ablation regime, observed only in thick films, is more difficult to understand. Molecular dynamics (MD) simulations could shed light on this issue, but detailed atomic potentials, required by MD, are not available for GST. However, it is hard to imagine that the high-fluence ablation behavior is unique to GST; similar studies on crystalline metal films (with fast electron-phonon coupling, such as aluminum), where MD simulations are available, would be very attractive.

We investigated the time evolution of the optical properties of fused silica after excitation by strong pump pulses with peak fluences above the ablation threshold. The optical properties were studied by simultaneous measurements

of *s*- and *p*-reflectivities ( $R_s$  and  $R_p$ , respectively) of time-delayed probe pulses. About 100 fs after the pump-pulse excitation, a significant drop in  $R_p$  was observed, which persisted for at least 1 ps. This was a general feature across the applied range of probe wavelengths. In order to explain the data, we proposed that a thin electron cloud is formed outside laser-excited solid through electron emission. An optical model based on the electron cloud and a Drude description of the excited dielectric with a time-dependent scattering rate, adequately explained all the features of our measurements. In a simplified picture, the drop in  $R_p$  is attributed to destructive interference between *p*-polarized light reflected partly by the electron cloud, and partly by the solid. We have observed a similar ultrafast drop in  $R_p$  on sapphire as well, which suggests that this is a general feature of strongly excited dielectrics. We discussed why these effects have rarely been reported before. By making the conditions, under which clear optical signatures of the electron cloud are possible, we hope that other research groups will choose to carry out similar experiments, where these conditions are fulfilled. Our experiments have so far been carried out in ambient atmosphere, where nonlinear effects might slightly affect the pump beam at the applied intensities. The next step is to repeat the experiments in vacuum and/or in a helium atmosphere to ascertain that potential nonlinear effects in air does not alter the present conclusions.

Finally, we used time-resolved cathodoluminescence (CL) as a tool to investigate the influence of metal nanoparticles on the spontaneous emission rate of nearby  $\text{Er}^{3+}$  ions. Analysis of the data was challenged by a complicated time-dependent luminescence of  $\text{Er}^{3+}$ , but we managed to see a 4–6 fold increase in the decay rate of  $\text{Er}^{3+}$  ions very close to a metal nanoparticle. However, to further improve these measurements, much more work would be needed on optimizing and preparing high-quality  $\text{Er}^{3+}$ -doped samples, which preferably should show single-exponential decay.



## BIBLIOGRAPHY

- [1] S. H. Møller, J. Vester-Petersen, A. Nazir, E. H. Eriksen, B. Julsgaard, S. P. Madsen, and P. Balling, *Near-field marking of gold nanostars by ultrashort pulsed laser irradiation: experiment and simulations*, Appl. Phys. A **124**, 210 (2018).
- [2] S. H. Møller, E. H. Eriksen, P. L. Tønning, P. B. Jensen, J. Chevallier, and P. Balling, *Femtosecond-laser-induced modifications of Ge<sub>2</sub>Sb<sub>2</sub>Te<sub>5</sub> thin films: Permanent optical change without amorphization*, Appl. Surf. Sci. **476**, 221 (2019).
- [3] N. L. Bindoff, P. A. Stott, K. M. AchutaRao, M. R. Allen, N. Gillett, D. Gutzler, K. Hansingo, G. Hegerl, Y. Hu, S. Jain, *et al.*, *Detection and attribution of climate change: from global to regional*, (2013).
- [4] R. P. Sorenson, *Eunice Foote's pioneering research on CO<sub>2</sub> and climate warming*, Search and Discovery (2011).
- [5] A. Polman, M. Knight, E. C. Garnett, B. Ehrler, and W. C. Sinke, *Photovoltaic materials: Present efficiencies and future challenges*, Science **352**, aad4424 (2016).
- [6] P. Würfel, *Physics of solar cells: from basic principles to advanced concepts* (Wiley-VCH, Weinheim, 2009).
- [7] J. Christiansen, H. Lakhotiya, E. Eriksen, S. P. Madsen, P. Balling, and B. Julsgaard, *Analytical model for the intensity dependence of 1500 nm to 980 nm upconversion in Er<sup>3+</sup>: A new tool for material characterization*, J. Appl. Phys. **125**, 043106 (2019).

- [8] P. Leiderer, C. Bartels, J. Koenig-Birk, M. Mosbacher, and J. Boneberg, *Imaging optical near-fields of nanostructures*, Appl. Phys. Lett. **85**, 5370 (2004).
- [9] A. Merlen and F. Lagugné-Labarthe, *Imaging the optical near field in plasmonic nanostructures*, Appl. Spectrosc **68**, 1307 (2014).
- [10] P. Kühler, F. J. G. de Abajo, P. Leiprecht, A. Kolloch, J. Solis, P. Leiderer, and J. Siegel, *Quantitative imaging of the optical near field*, Opt. Express **20**, 22063 (2012).
- [11] C. David, P. Kühler, F. J. G. de Abajo, and J. Siegel, *Near-field nanoimprinting using colloidal monolayers*, Opt. Express **22**, 8226 (2014).
- [12] D. J. Griffiths, *Introduction to Electrodynamics*, 3rd ed. (Pearson Benjamin Cummings, 2008).
- [13] L. D. Landau, J. Bell, M. Kearsley, L. Pitaevskii, E. Lifshitz, and J. Sykes, *Electrodynamics of continuous media*, Vol. 8 (Elsevier, 2013).
- [14] L. Novotny and B. Hecht, *Principles of Nano-Optics* (Cambridge University Press, 2009).
- [15] S. J. Byrnes, *Multilayer optical calculations*, arXiv e-prints , arXiv:1603.02720 (2016), arXiv:1603.02720 [physics.comp-ph] .
- [16] M. Pelton and G. W. Bryant, *Introduction to Metal-Nanoparticle Plasmonics* (Wiley, 2013).
- [17] N. W. Ashcroft and N. D. Mermin, *Solid state physics* (Brooks/Cole, Belmont, 1976).
- [18] P. B. Johnson and R. W. Christy, *Optical Constants of the Noble Metals*, Phys. Rev. B **6**, 4370 (1972).
- [19] S. Maier, *Plasmonics: fundamentals and applications* (Springer, New York, 2007).
- [20] R. Yu, L. M. Liz-Marzán, and F. J. García de Abajo, *Universal analytical modeling of plasmonic nanoparticles*, Chem. Soc. Rev. **46**, 6710 (2017).

- [21] C. F. Bohren and D. R. Huffman, *Absorption and scattering of light by small particles* (John Wiley & Sons, 1983).
- [22] J. Zuloaga and P. Nordlander, *On the Energy Shift between Near-Field and Far-Field Peak Intensities in Localized Plasmon Systems*, *Nano Lett.* **11**, 1280 (2011).
- [23] P. W. Milonni and J. H. Eberly, *Laser physics* (John Wiley & Sons, Hoboken, N.J., 2010).
- [24] L. V. Keldysh, *Ionization in the field of a strong electromagnetic wave*, *Sov. Phys. JETP* **20**, 1307 (1965).
- [25] M. Lenzner, J. Krüger, S. Sartania, Z. Cheng, C. Spielmann, G. Mourou, W. Kautek, and F. Krausz, *Femtosecond Optical Breakdown in Dielectrics*, *Phys. Rev. Lett.* **80**, 4076 (1998).
- [26] P. P. Pronko, P. A. VanRompay, C. Horvath, F. Loesel, T. Juhasz, X. Liu, and G. Mourou, *Avalanche ionization and dielectric breakdown in silicon with ultrafast laser pulses*, *Phys. Rev. B* **58**, 2387 (1998).
- [27] D. Grojo, M. Gertsvolf, S. Lei, T. Barillot, D. M. Rayner, and P. B. Corkum, *Exciton-seeded multiphoton ionization in bulk SiO<sub>2</sub>*, *Phys. Rev. B* **81**, 212301 (2010).
- [28] F. Quéré, S. Guizard, and P. Martin, *Time-resolved study of laser-induced breakdown in dielectrics*, *EPL* **56**, 138 (2001).
- [29] A. Q. Wu, I. H. Chowdhury, and X. Xu, *Femtosecond laser absorption in fused silica: Numerical and experimental investigation*, *Phys. Rev. B* **72**, 085128 (2005).
- [30] P. Balling and J. Schou, *Femtosecond-laser ablation dynamics of dielectrics: basics and applications for thin films*, *Rep. Prog. Phys.* **76**, 036502 (2013).
- [31] M. V. Shugaev, C. Wu, O. Armbruster, A. Naghilou, N. Brouwer, D. S. Ivanov, T. J.-Y. Derrien, N. M. Bulgakova, W. Kautek, B. Rethfeld, and L. Zhigilei, *Fundamentals of ultrafast laser-material interaction*, *MRS Bulletin* **41**, 960–968 (2016).

- [32] M. V. Shugaev, C.-Y. Shih, E. T. Karim, C. Wu, and L. V. Zhigilei, *Generation of nanocrystalline surface layer in short pulse laser processing of metal targets under conditions of spatial confinement by solid or liquid overlayer*, Appl. Surf. Sci. **417**, 54 (2017).
- [33] R. Stoian, D. Ashkenasi, A. Rosenfeld, and E. E. B. Campbell, *Coulomb explosion in ultrashort pulsed laser ablation of Al<sub>2</sub>O<sub>3</sub>*, Phys. Rev. B **62**, 13167 (2000).
- [34] R. Stoian, A. Rosenfeld, D. Ashkenasi, I. V. Hertel, N. M. Bulgakova, and E. E. B. Campbell, *Surface Charging and Impulsive Ion Ejection during Ultrashort Pulsed Laser Ablation*, Phys. Rev. Lett. **88**, 097603 (2002).
- [35] N. M. Bulgakova, R. Stoian, A. Rosenfeld, I. V. Hertel, and E. E. B. Campbell, *Electronic transport and consequences for material removal in ultrafast pulsed laser ablation of materials*, Phys. Rev. B **69**, 054102 (2004).
- [36] D. A. Genov, A. K. Sarychev, V. M. Shalaev, and A. Wei, *Resonant field enhancements from metal nanoparticle arrays*, Nano Lett. **4**, 153 (2004).
- [37] J. Mock, M. Barbic, D. Smith, D. Schultz, and S. Schultz, *Shape effects in plasmon resonance of individual colloidal silver nanoparticles*, J. Chem. Phys. **116**, 6755 (2002).
- [38] J. J. Mock, D. R. Smith, and S. Schultz, *Local refractive index dependence of plasmon resonance spectra from individual nanoparticles*, Nano Lett. **3**, 485 (2003).
- [39] X. Luo, A. Morrin, A. J. Killard, and M. R. Smyth, *Application of nanoparticles in electrochemical sensors and biosensors*, Electroanalysis **18**, 319 (2006).
- [40] H. A. Atwater and A. Polman, *Plasmonics for improved photovoltaic devices*, Nat. Mater. **9**, 205 (2010).
- [41] M. Kauranen and A. V. Zayats, *Nonlinear plasmonics*, Nat. Photonics **6**, 737 (2012).
- [42] F. J. G. de Abajo, *Microscopy: plasmons go quantum*, Nature **483**, 417 (2012).

- [43] J. Olson, S. Dominguez-Medina, A. Hoggard, L.-Y. Wang, W.-S. Chang, and S. Link, *Optical characterization of single plasmonic nanoparticles*, Chem. Soc. Rev. **44**, 40 (2015).
- [44] C. Forestiere, A. J. Pasquale, A. Capretti, G. Miano, A. Tamburrino, S. Y. Lee, B. M. Reinhard, and L. Dal Negro, *Genetically engineered plasmonic nanoarrays*, Nano Lett. **12**, 2037 (2012).
- [45] H. Lakhotiya, A. Nazir, S. P. Madsen, J. Christiansen, E. Eriksen, J. Vester-Petersen, S. R. Johannsen, B. R. Jeppesen, P. Balling, A. N. Larsen, and B. Julsgaard, *Plasmonically enhanced upconversion of 1500 nm light via trivalent Er in a TiO<sub>2</sub> matrix*, Appl. Phys. Lett. **109**, 263102 (2016).
- [46] J. Krenn, A. Dereux, J. Weeber, E. Bourillot, Y. Lacroute, J. Goudonnet, G. Schider, W. Gotschy, A. Leitner, F. Aussenegg, *et al.*, *Squeezing the optical near-field zone by plasmon coupling of metallic nanoparticles*, Phys. Rev. Lett. **82**, 2590 (1999).
- [47] F.-P. Schmidt, H. Ditlbacher, U. Hohenester, A. Hohenau, F. Hofer, and J. R. Krenn, *Dark plasmonic breathing modes in silver nanodisks*, Nano Lett. **12**, 5780 (2012).
- [48] T. Coenen, D. T. Schoen, B. J. Brenny, A. Polman, and M. L. Brongersma, *Combined electron energy-loss and cathodoluminescence spectroscopy on individual and composite plasmonic nanostructures*, Phys. Rev. B **93**, 195429 (2016).
- [49] J. Fiutowski, C. Maibohm, O. Kostiučenko, J. Kjelstrup-Hansen, and H.-G. Rubahn, *Mapping of gold nanostructure-enhanced near fields via laser scanning second-harmonic generation and ablation*, J. Nanophotonics **6**, 063515 (2012).
- [50] S. Dickreuter, J. Gleixner, A. Kolloch, J. Boneberg, E. Scheer, and P. Leiderer, *Mapping of plasmonic resonances in nanotriangles*, Beilstein J. Nanotechnol. **4**, 588 (2013).
- [51] C. Deeb, R. Bachelot, J. Plain, A.-L. Baudrion, S. Jradi, A. Bouhelier, O. Soppera, P. K. Jain, L. Huang, C. Ecoffet, *et al.*, *Quantitative analysis of localized surface plasmons based on molecular probing*, ACS Nano **4**, 4579 (2010).

- [52] T. Geldhauser, A. Kolloch, N. Murazawa, K. Ueno, J. Boneberg, P. Leiderer, E. Scheer, and H. Misawa, *Quantitative measurement of the near-field enhancement of nanostructures by two-photon polymerization*, *Langmuir* **28**, 9041 (2012).
- [53] J.-M. Jin, *Theory and Computation of Electromagnetic Fields* (John Wiley & Sons, Inc., 2010).
- [54] E. H. Eriksen, B. Julsgaard, S. P. Madsen, H. Lakhotiya, A. Nazir, and P. Balling, *Particle-particle interactions in large, sparse arrays of randomly distributed plasmonic metal nanoparticles: a two-particle model*, *Opt. Express* **25**, 19354 (2017).
- [55] S. P. Madsen, S. R. Johannsen, B. R. Jeppesen, J. V. Nygaard, P. B. Jensen, J. Chevallier, B. Julsgaard, P. Balling, and A. N. Larsen, *Optimizing Plasmonically Enhanced Upconversion*, *Energy Procedia* **77**, 478 (2015).
- [56] E. Centurioni, *Generalized matrix method for calculation of internal light energy flux in mixed coherent and incoherent multilayers*, *Appl. Opt.* **44**, 7532 (2005).
- [57] I. H. Malitson, *Interspecimen Comparison of the Refractive Index of Fused Silica*, *J. Opt. Soc. Am.* **55**, 1205 (1965).
- [58] COMSOL AB, *COMSOL Multiphysics® v. 5.3*.
- [59] J. M. Liu, *Simple technique for measurements of pulsed Gaussian-beam spot sizes*, *Opt. Lett.* **7**, 196 (1982).
- [60] E. Kraaikamp, *AutoStakkert v. 2.6.8*.
- [61] A. Habenicht, M. Olapinski, F. Burmeister, P. Leiderer, and J. Boneberg, *Jumping nanodroplets*, *Science* **309**, 2043 (2005).
- [62] C. Spindt, I. Brodie, L. Humphrey, and E. Westerberg, *Physical properties of thin-film field emission cathodes with molybdenum cones*, *J. Appl. Phys.* **47**, 5248 (1976).
- [63] J. Henson, J. DiMaria, and R. Paiella, *Influence of nanoparticle height on plasmonic resonance wavelength and electromagnetic field enhancement in two-dimensional arrays*, *J. Appl. Phys.* **106**, 093111 (2009).

- [64] A. Robitaille, É. Boulais, and M. Meunier, *Mechanisms of plasmon-enhanced femtosecond laser nanoablation of silicon*, Opt. Express **21**, 9703 (2013).
- [65] A. Rämér, O. Osmani, and B. Rethfeld, *Laser damage in silicon: energy absorption, relaxation, and transport*, J. Appl. Phys. **116**, 053508 (2014).
- [66] S. Maruo, O. Nakamura, and S. Kawata, *Three-dimensional microfabrication with two-photon-absorbed photopolymerization*, Opt. Lett. **22**, 132 (1997).
- [67] S. Juodkazis, V. Mizeikis, K. K. Seet, M. Miwa, and H. Misawa, *Two-photon lithography of nanorods in SU-8 photoresist*, Nanotechnology **16**, 846 (2005).
- [68] L. Li and J. T. Fourkas, *Multiphoton polymerization*, Mater. Today **10**, 30 (2007).
- [69] L. Jonušauskas, D. Gailevičius, S. Rekštytė, T. Baldacchini, S. Juodkazis, and M. Malinauskas, *Mesoscale laser 3D printing*, Opt. Express **27**, 15205 (2019).
- [70] A. Sundaramurthy, P. J. Schuck, N. R. Conley, D. P. Fromm, G. S. Kino, and W. E. Moerner, *Toward Nanometer-Scale Optical Photolithography: Utilizing the Near-Field of Bowtie Optical Nanoantennas*, Nano Lett. **6**, 355 (2006).
- [71] C. Deeb, X. Zhou, R. Miller, S. K. Gray, S. Marguet, J. Plain, G. P. Wiederrecht, and R. Bachelot, *Mapping the Electromagnetic Near-Field Enhancements of Gold Nanocubes*, J. Phys. Chem. C **116**, 24734 (2012).
- [72] C. Deeb, X. Zhou, J. Plain, G. P. Wiederrecht, R. Bachelot, M. Russell, and P. K. Jain, *Size Dependence of the Plasmonic Near-Field Measured via Single-Nanoparticle Photoimaging*, J. Phys. Chem. C **117**, 10669 (2013).
- [73] K. Naka, *Monomers, Oligomers, Polymers, and Macromolecules (Overview)*, in *Encyclopedia of Polymeric Nanomaterials* (Springer Berlin Heidelberg, 2014) pp. 1–6.
- [74] Y. Jee, M. F. Becker, and R. M. Walser, *Laser-induced damage on single-crystal metal surfaces*, J. Opt. Soc. Am. B **5**, 648 (1988).

- [75] J. Byskov-Nielsen, J.-M. Savolainen, M. S. Christensen, and P. Balling, *Ultra-short pulse laser ablation of metals: threshold fluence, incubation coefficient and ablation rates*, Appl. Phys. A **101**, 97 (2010).
- [76] S. Raoux, F. Xiong, M. Wuttig, and E. Pop, *Phase change materials and phase change memory*, MRS Bulletin **39**, 703 (2014).
- [77] V. Weidenhof, I. Friedrich, S. Ziegler, and M. Wuttig, *Atomic force microscopy study of laser induced phase transitions in Ge<sub>2</sub>Sb<sub>2</sub>Te<sub>5</sub>*, J. Appl. Phys. **86**, 5879 (1999).
- [78] J. Siegel, C. N. Afonso, and J. Solis, *Dynamics of ultrafast reversible phase transitions in GeSb films triggered by picosecond laser pulses*, Appl. Phys. Lett. **75**, 3102 (1999).
- [79] J. Siegel, A. Schropp, J. Solis, C. N. Afonso, and M. Wuttig, *Rewritable phase-change optical recording in Ge<sub>2</sub>Sb<sub>2</sub>Te<sub>5</sub> films induced by picosecond laser pulses*, Appl. Phys. Lett. **84**, 2250 (2004).
- [80] M. Konishi, H. Santo, Y. Hongo, K. Tajima, M. Hosoi, and T. Saiki, *Ultrafast amorphization in Ge<sub>10</sub>Sb<sub>2</sub>Te<sub>13</sub> thin film induced by single femtosecond laser pulse*, Appl. Opt. **49**, 3470 (2010).
- [81] J. Takeda, W. Oba, Y. Minami, T. Saiki, and I. Katayama, *Ultrafast crystalline-to-amorphous phase transition in Ge<sub>2</sub>Sb<sub>2</sub>Te<sub>5</sub> chalcogenide alloy thin film using single-shot imaging spectroscopy*, Appl. Phys. Lett. **104**, 261903 (2014).
- [82] L. Waldecker, T. A. Miller, M. Rudé, R. Bertoni, J. Osmond, V. Pruneri, R. E. Simpson, R. Ernstorfer, and S. Wall, *Time-domain separation of optical properties from structural transitions in resonantly bonded materials*, Nat. Mater. **14**, 991 (2015).
- [83] E. Matsubara, S. Okada, T. Ichitsubo, T. Kawaguchi, A. Hirata, P. Guan, K. Tokuda, K. Tanimura, T. Matsunaga, M. Chen, and N. Yamada, *Initial Atomic Motion Immediately Following Femtosecond-Laser Excitation in Phase-Change Materials*, Phys. Rev. Lett. **117**, 135501 (2016).
- [84] R. O. Jones, *Bonding in phase change materials: concepts and misconceptions*, J. Phys.: Condens. Matter **30**, 153001 (2018).

- [85] G. Lucovsky and R. M. White, *Effects of Resonance Bonding on the Properties of Crystalline and Amorphous Semiconductors*, Phys. Rev. B **8**, 660 (1973).
- [86] B. Huang and J. Robertson, *Bonding origin of optical contrast in phase-change memory materials*, Phys. Rev. B **81**, 081204(R) (2010).
- [87] K. Shimakawa, L. Stržičik, T. Wagner, and M. Frumar, *Penn gap rule in phase-change memory materials: No clear evidence for resonance bonds*, APL Mater. **3**, 041801 (2015).
- [88] Y. Saito, Y. Sutou, P. Fons, S. Shindo, X. Kozina, J. M. Skelton, A. V. Kolobov, and K. Kobayashi, *Electronic Structure of Transition-Metal Based  $\text{Cu}_2\text{GeTe}_3$  Phase Change Material: Revealing the Key Role of Cu d Electrons*, Chem. Mater. **29**, 7440 (2017).
- [89] I. Friedrich, V. Weidenhof, W. Njoroge, P. Franz, and M. Wuttig, *Structural transformations of  $\text{Ge}_2\text{Sb}_2\text{Te}_5$  films studied by electrical resistance measurements*, J. Appl. Phys. **87**, 4130 (2000).
- [90] J. Orava, T. Wágner, J. Šik, J. Přikryl, M. Frumar, and L. Beneš, *Optical properties and phase change transition in  $\text{Ge}_2\text{Sb}_2\text{Te}_5$  flash evaporated thin films studied by temperature dependent spectroscopic ellipsometry*, J. Appl. Phys. **104**, 043523 (2008).
- [91] E. Gourvest, B. Pelissier, C. Vallée, A. Roule, S. Lhostis, and S. Maitre-jean, *Impact of Oxidation on  $\text{Ge}_2\text{Sb}_2\text{Te}_5$  and  $\text{GeTe}$  Phase-Change Properties*, J. Electrochem. Soc. **159**, H373 (2012).
- [92] N. Uchida, *Optical Properties of Single-Crystal Paratellurite ( $\text{TeO}_2$ )*, Phys. Rev. B **4**, 3736 (1971).
- [93] S. I. Anisimov, B. L. Kapeliovich, and T. L. Perel'man, *Sov. Phys. JETP* **39**, 375 (1974).
- [94] B. Rethfeld, D. S. Ivanov, M. E. Garcia, and S. I. Anisimov, *Modelling ultrafast laser ablation*, J. Phys. D: Appl. Phys. **50**, 193001 (2017).
- [95] H. M. van Driel, *Kinetics of high-density plasmas generated in Si by 1.06- and 0.53- $\mu\text{m}$ picosecond laser pulses*, Phys. Rev. B **35**, 8166 (1987).

- [96] J. Lee, E. Bozorg-Grayeli, S. Kim, M. Asheghi, H.-S. P. Wong, and K. E. Goodson, *Phonon and electron transport through Ge<sub>2</sub>Sb<sub>2</sub>Te<sub>5</sub> films and interfaces bounded by metals*, Appl. Phys. Lett. **102**, 191911 (2013).
- [97] M. Kuwahara, O. Suzuki, Y. Yamakawa, N. Taketoshi, T. Yagi, P. Fons, T. Fukaya, J. Tominaga, and T. Baba, *Temperature Dependence of the Thermal Properties of Optical Memory Materials*, Jpn. J. Appl. Phys. **46**, 3909 (2007).
- [98] J. Kalb, F. Spaepen, and M. Wuttig, *Calorimetric measurements of phase transformations in thin films of amorphous Te alloys used for optical data storage*, J. Appl. Phys. **93**, 2389 (2003).
- [99] G. P. Ortiz and W. L. Mochán, *Nonadditivity of Poynting vector within opaque media*, J. Opt. Soc. Am. A **22**, 2827 (2005).
- [100] E. H. Eriksen, *tmmppy* (2018).
- [101] P. L. Liu, R. Yen, N. Bloembergen, and R. T. Hodgson, *Picosecond laser-induced melting and resolidification morphology on Si*, Appl. Phys. Lett. **34**, 864 (1979).
- [102] J. M. Liu, R. Yen, H. Kurz, and N. Bloembergen, *Phase transformation on and charged particle emission from a silicon crystal surface, induced by picosecond laser pulses*, Appl. Phys. Lett. **39**, 755 (1981).
- [103] W. M. Stobbs, *Electron Microscopical Techniques For The Observation Of Cavities*, J. Microsc. **116**, 3 (1979).
- [104] X. Sun, M. Ehrhardt, A. Lotnyk, P. Lorenz, E. Thelander, J. W. Gerlach, T. Smausz, U. Decker, and B. Rauschenbach, *Crystallization of Ge<sub>2</sub>Sb<sub>2</sub>Te<sub>5</sub> thin films by nano- and femtosecond single laser pulse irradiation*, Sci. Rep. **6**, 28246 (2016).
- [105] V. Weidenhof, I. Friedrich, S. Ziegler, and M. Wuttig, *Laser induced crystallization of amorphous Ge<sub>2</sub>Sb<sub>2</sub>Te<sub>5</sub> films*, J. Appl. Phys. **89**, 3168 (2001).
- [106] R. L. Cotton and J. Siegel, *Stimulated crystallization of melt-quenched Ge<sub>2</sub>Sb<sub>2</sub>Te<sub>5</sub> films employing femtosecond laser double pulses*, J. Appl. Phys. **112**, 123520 (2012).

- [107] M. Domke, L. Nobile, S. Rapp, S. Eiselen, J. Sotrop, H. P. Huber, and M. Schmidt, *Understanding Thin Film Laser Ablation: The Role of the Effective Penetration Depth and the Film Thickness*, Phys. Procedia **56**, 1007 (2014).
- [108] R. S. Dingus and R. J. Scammon, *Grüneisen-stress induced ablation of biological tissue*, in *Laser-Tissue Interact. II*, edited by S. L. Jacques (SPIE, 1991).
- [109] E. Leveugle, D. Ivanov, and L. Zhigilei, *Photomechanical spallation of molecular and metal targets: molecular dynamics study*, Appl. Phys. A **79**, 1643 (2004).
- [110] L. V. Zhigilei, Z. Lin, and D. S. Ivanov, *Atomistic Modeling of Short Pulse Laser Ablation of Metals: Connections between Melting, Spallation, and Phase Explosion*, J. Phys. Chem. C **113**, 11892 (2009).
- [111] J.-M. Savolainen, M. S. Christensen, and P. Balling, *Material swelling as the first step in the ablation of metals by ultrashort laser pulses*, Phys. Rev. B **84**, 193410 (2011).
- [112] C. Wu, M. S. Christensen, J.-M. Savolainen, P. Balling, and L. V. Zhigilei, *Generation of subsurface voids and a nanocrystalline surface layer in femtosecond laser irradiation of a single-crystal Ag target*, Phys. Rev. B **91**, 035413 (2015).
- [113] M. Olbrich, E. Punzel, P. Lickschat, S. Weißmantel, and A. Horn, *Investigation on the Ablation of thin Metal Films with Femtosecond to Picosecond-pulsed Laser Radiation*, Phys. Procedia **83**, 93 (2016).
- [114] M. Olbrich, E. Punzel, R. Roesch, R. Oettking, B. Muhsin, H. Hoppe, and A. Horn, *Case study on the ultrafast laser ablation of thin aluminum films: dependence on laser parameters and film thickness*, Appl. Phys. A **122**, 215 (2016).
- [115] R. Cecchini, K. Kohary, A. Fernández, M. Cabibbo, and A. Marmier, *Determination of the Anisotropic Elastic Properties of Rocksalt Ge<sub>2</sub>Sb<sub>2</sub>Te<sub>5</sub> by XRD, Residual Stress, and DFT*, J. Phys. Chem. C **120**, 5624 (2016).
- [116] J. Kalikka, J. Akola, J. Larrucea, and R. O. Jones, *Nucleus-driven crystallization of amorphous Ge<sub>2</sub>Sb<sub>2</sub>Te<sub>5</sub>: A density functional study*, Phys. Rev. B **86**, 144113 (2012).

- [117] P. Zalden, K. S. Siegert, S. Rols, H. E. Fischer, F. Schlich, T. Hu, and M. Wuttig, *Specific Heat of (GeTe)<sub>x</sub>(Sb<sub>2</sub>Te<sub>3</sub>)<sub>1-x</sub> Phase-Change Materials: The Impact of Disorder and Anharmonicity*, Chem. Mater. **26**, 2307 (2014).
- [118] T. Gotoh, *Effect of annealing on carrier concentration in Ge<sub>2</sub>Sb<sub>2</sub>Te<sub>5</sub> films*, Can. J. Phys. **92**, 681 (2014).
- [119] H. S. Carslaw and J. C. Jaeger, *Conduction of heat in solids*, 2nd ed. (Oxford: Clarendon Press, 1959).
- [120] E. T. Swartz and R. O. Pohl, *Thermal boundary resistance*, Rev. Mod. Phys. **61**, 605 (1989).
- [121] H. P. Langtangen and S. Linge, *Finite Difference Computing with PDEs: A Modern Software Approach*, Vol. 16 (Springer, 2017).
- [122] C. Swaminathan and V. Voller, *On the enthalpy method*, Int. J. Heat Fluid Flow **3**, 233 (1993).
- [123] B. Rethfeld, *Free-electron generation in laser-irradiated dielectrics*, Phys. Rev. B **73**, 035101 (2006).
- [124] C. Thaury, F. Quéré, J.-P. Geindre, A. Levy, T. Ceccotti, P. Monot, M. Bougeard, F. Réau, P. d'Oliveira, P. Audebert, R. Marjoribanks, and P. Martin, *Plasma mirrors for ultrahigh-intensity optics*, Nat. Phys. **3**, 424 (2007).
- [125] K. Sokolowski-Tinten, J. Bialkowski, and D. von der Linde, *Ultrafast laser-induced order-disorder transitions in semiconductors*, Phys. Rev. B **51**, 14186 (1995).
- [126] F. Quéré, S. Guizard, P. Martin, G. Petite, O. Gobert, P. Meynadier, and M. Perdrix, *Ultrafast carrier dynamics in laser-excited materials: sub-picosecond optical studies*, Appl. Phys. B **68**, 459 (1999).
- [127] C. Quoi, G. Hamoniaux, A. Antonetti, J.-C. Gauthier, J.-P. Geindre, and P. Audebert, *Ultrafast plasma studies by phase and amplitude measurements with femtosecond spectral interferometry*, J. Quant. Spectrosc. Radiat. Transf. **65**, 455 (2000).

- [128] K. Sokolowski-Tinten and D. von der Linde, *Generation of dense electron-hole plasmas in silicon*, Phys. Rev. B **61**, 2643 (2000).
- [129] D. Puerto, W. Gawelda, J. Siegel, J. Bonse, G. Bachelier, and J. Solis, *Transient reflectivity and transmission changes during plasma formation and ablation in fused silica induced by femtosecond laser pulses*, Appl. Phys. A **92**, 803 (2008).
- [130] M. Garcia-Lechuga, J. Siegel, J. Hernandez-Rueda, and J. Solis, *Imaging the ultrafast Kerr effect, free carrier generation, relaxation and ablation dynamics of Lithium Niobate irradiated with femtosecond laser pulses*, J. Appl. Phys. **116**, 113502 (2014).
- [131] F. Meng, M. D. Thomson, B. E. Sernelius, M. Jörger, and H. G. Roskos, *Ultrafast dynamic conductivity and scattering rate saturation of photoexcited charge carriers in silicon investigated with a midinfrared continuum probe*, Phys. Rev. B **91**, 075201 (2015).
- [132] L. Haahr-Lillevang, K. Wædegaard, D. B. Sandkamm, A. Mouskeftaras, S. Guizard, and P. Balling, *Short-pulse laser excitation of quartz: experiments and modelling of transient optical properties and ablation*, Appl. Phys. A **120**, 1221 (2015).
- [133] T. Kumada, T. Otobe, M. Nishikino, N. Hasegawa, and T. Hayashi, *Dynamics of spallation during femtosecond laser ablation studied by time-resolved reflectivity with double pump pulses*, Appl. Phys. Lett. **108**, 011102 (2016).
- [134] M. Garcia-Lechuga, L. Haahr-Lillevang, J. Siegel, P. Balling, S. Guizard, and J. Solis, *Simultaneous time-space resolved reflectivity and interferometric measurements of dielectrics excited with femtosecond laser pulses*, Phys. Rev. B **95**, 214114 (2017).
- [135] T. Winkler, L. Haahr-Lillevang, C. Sarpe, B. Zielinski, N. Götte, A. Sentsleben, P. Balling, and T. Baumert, *Laser amplification in excited dielectrics*, Nat. Phys. **14**, 74 (2017).
- [136] H. Tompkins and E. A. Irene, *Handbook of Ellipsometry* (William Andrew, 2005).

- [137] C. Fourment, B. Chimier, F. Deneuille, D. Descamps, F. Dorchies, G. Duchateau, M.-C. Nadeau, and S. Petit, *Ultrafast changes in optical properties of SiO<sub>2</sub> excited by femtosecond laser at the damage threshold and above*, Phys. Rev. B **98**, 155110 (2018).
- [138] N. Brouwer and B. Rethfeld, *Excitation and relaxation dynamics in dielectrics irradiated by an intense ultrashort laser pulse*, J. Opt. Soc. Am. B **31**, C28 (2014).
- [139] B. Rethfeld, A. Ramer, N. Brouwer, N. Medvedev, and O. Osmani, *Electron dynamics and energy dissipation in highly excited dielectrics*, Nucl. Instrum. Methods Phys. Res. **327**, 78 (2014).
- [140] W. Kruer, *The physics of laser plasma interactions* (Addison-Wesley, Redwood City, Calif, 1988).
- [141] A. Belsky, H. Bachau, J. Gaudin, G. Geoffroy, S. Guizard, P. Martin, G. Petite, A. Philippov, A. Vasil'ev, and B. Yatsenko, *Observation of high energy photoelectrons from solids at moderate laser intensity*, Appl. Phys. B **78**, 989 (2004).
- [142] A. Belsky, P. Martin, H. Bachau, A. N. Vasil'ev, B. N. Yatsenko, S. Guizard, G. Geoffroy, and G. Petite, *Heating of conduction band electrons by intense femtosecond laser pulses*, EPL **67**, 301 (2004).
- [143] I. Chowdhury, A. Wu, X. Xu, and A. Weiner, *Ultra-fast laser absorption and ablation dynamics in wide-band-gap dielectrics*, Appl. Phys. A **81**, 1627 (2005).
- [144] W. Von der Linden, V. Dose, and U. Von Toussaint, *Bayesian Probability Theory: Applications in the Physical Sciences* (Cambridge University Press, 2014).
- [145] C. Rackauckas and Q. Nie, *DifferentialEquations.jl – A Performant and Feature-Rich Ecosystem for Solving Differential Equations in Julia*, J. Open Res. Softw. **5**, 15 (2017).
- [146] P. K. Mogensen and A. N. Riseth, *Optim: A mathematical optimization package for Julia*, J. Open Source Softw. **3**, 615 (2018).

- [147] M. Born and E. Wolf, *Principles of Optics: Electromagnetic Theory of Propagation, Interference and Diffraction of Light*, 7th ed. (Cambridge University Press, 1999).
- [148] E. M. Purcell, *Spontaneous emission probabilities at radio frequencies*, Phys. Rev. **69**, 681 (1946).
- [149] B. J. M. Brenny, A. Polman, and F. J. G. de Abajo, *Femtosecond plasmon and photon wave packets excited by a high-energy electron on a metal or dielectric surface*, Phys. Rev. B **94**, 155412 (2016).
- [150] F. J. G. de Abajo, *Optical excitations in electron microscopy*, Rev. Mod. Phys. **82**, 209 (2010).
- [151] B. J. M. Brenny, T. Coenen, and A. Polman, *Quantifying coherent and incoherent cathodoluminescence in semiconductors and metals*, J. of Appl. Phys. **115**, 244307 (2014).
- [152] D. Drouin, A. R. Couture, D. Joly, X. Tastet, V. Aimez, and R. Gauvin, *CASINO V2. 42—a fast and easy-to-use modeling tool for scanning electron microscopy and microanalysis users*, Scanning **29**, 92 (2007).
- [153] S. Meuret, M. S. Garcia, T. Coenen, E. Kieft, H. Zeijlemaker, M. Lätzel, S. Christiansen, S. Woo, Y. Ra, Z. Mi, and A. Polman, *Complementary cathodoluminescence lifetime imaging configurations in a scanning electron microscope*, Ultramicroscopy **197**, 28 (2019).
- [154] R. J. Moerland, I. G. C. Weppelman, M. W. H. Garming, P. Kruit, and J. P. Hooogenboom, *Time-resolved cathodoluminescence microscopy with sub-nanosecond beam blanking for direct evaluation of the local density of states*, Opt. Express **24**, 24760 (2016).
- [155] M. S. Bresler, O. B. Gusev, N. A. Sobolev, E. I. Terukov, I. N. Yassievich, B. P. Zakharchenya, and T. Gregorkevich, *Mechanisms of excitation and thermal quenching of erbium-ion luminescence in crystalline and amorphous silicon*, Phys. Solid State **41**, 770 (1999).
- [156] H. Lakhotiya, J. Christiansen, J. L. Hansen, P. Balling, and B. Julsgaard, *Upconversion luminescence from magnetron-sputtered Er<sup>3+</sup>-doped TiO<sub>2</sub> films: Influence of deposition- and annealing temperatures and correlation to decay times*, J. Appl. Phys. **124**, 163105 (2018).

- 
- [157] G. L. Bretthorst, W. C. Hutton, J. R. Garbow, and J. J. Ackerman, *Exponential parameter estimation (in NMR) using Bayesian probability theory*, *Concept. Magn. Reson. A* **27A**, 55 (2005).
- [158] M. K. Mahata, T. Koppe, T. Mondal, C. Brüsewitz, K. Kumar, V. K. Rai, H. Hofsäss, and U. Vetter, *Incorporation of Zn<sup>2+</sup> ions into Ba-TiO<sub>3</sub>:Er<sup>3+</sup>/Yb<sup>3+</sup> nanophosphor: an effective way to enhance upconversion, defect luminescence and temperature sensing*, *Phys. Chem. Chem. Phys.* **17**, 20741 (2015).
- [159] R. J. Moerland, I. G. C. Weppelman, M. Scotuzzi, and J. P. Hoogenboom, *Nanoscale Imaging of Light-Matter Coupling Inside Metal-Coated Cavities with a Pulsed Electron Beam*, *Nano Lett.* **18**, 6107 (2018).